Photothermal Spectroscopy of Confined Liquids Using Microfluidic Cantilevers

by

Maryam Sadat Ghoraishi Kahangi

A thesis submitted in partial fulfillment of the requirements for the degree of

Doctor of Philosophy

In
Chemical Engineering

Department of Chemical and Materials Engineering
University of Alberta

Abstract

Due to their ability to measure extremely small displacements and forces, nanomechanical cantilevers have attracted considerable attention from numerous scientific communities, each exploring a variety of applications. Though typically operated in either vacuum or air, operation of the device in liquid media remains highly challenging, primarily due to strong viscous damping. In order to overcome this limitation a variation of the microfluidic cantilever sensor capable of confining 1-300 picoliter volumes of liquid sample was fabricated. The capabilities of this platform were then investigated in both the static and dynamic mode of operation.

While calorimetry-based bi-material cantilever spectrometer has been shown to be a very promising platform when operated in air, this technique loses its sensitivity when operated in the liquid phase due to significantly reduced extinction lengths and increased thermal losses. It is thus not suitable for infrared spectroscopic measurements therein and an alternate approach is required.

Confining a liquid inside the microcantilever affords a means to overcome the limitations inherent to standard bi-material microcantilevers by decreasing thermal loss and viscous damping, and allowing for the study of calorimetry-based spectroscopy of liquids. Simultaneously, the low resolution and signal-to-noise ratio of mid infrared (MIR) spectroscopy in aqueous media can be addressed by employing a quantum cascade laser as the light source. The effects of solvent-solute interactions on the absorption peaks related to C-C-O in ethanol have been investigated using this micromechanical calorimetric spectroscopy platform to collect infrared (IR) spectra of ethanol-water mixtures. The results revealed a power law dependence of the IR absorption peak

positions to the induced dipole moments of ethanol in the ethanol-water mixtures. Using such a microfluidic based spectroscopy method can provide high-resolution liquid spectroscopy measurements to further investigate intermolecular interactions.

The thermal sensitivity of a bi-material microcantilever plays a critical role in calorimetric spectroscopy when the device is used to collect photothermal spectra of liquid samples. However, further improvements in their applications as a spectroscopic platform depends on an enhanced understanding of the device's response to heat. In this work, a new model applicable to the bi-material microfluidic cantilever is presented when the device undergoes uniform heating. The presented analysis indicates that an increase in the thermal sensitivity, resulting from reducing the channel height, can improve the photothermal response of this platform and allow for improving the sensitivity, resolution, and selectivity of photothermal deflection spectroscopic measurements.

Piezoelectric crystals in feedback loops have been mainly employed as driving mechanisms for microfluidic cantilever resonators when the device was used to analyze liquid samples. However, there has not yet been any report on actuating a microfluidic cantilever by applying AC voltage on a confined electrolyte solution. In this work, nanograms of $NaHSO_4$ and $NaCl$ solutions in combination with an AC potential difference were used to actuate microfluidic cantilevers. The results indicate that the resonance amplitude increases as a function of applied voltage. However, an increase in the concentration of the electrolyte does not necessarily result in an increase in the amplitude. This concept can possibly be employed to design a new online actuation method in the future.

Preface

This thesis is an original work of Maryam Sadat Ghoraishi Kahangi. The literature review in this thesis was done by myself. Fabrication of the devices, presented in Chapter 3, was conducted by myself and the design of the device was provided by M. F. Khan. The design and establishment of the experimental set-ups used throughout chapters 3, 5, and 6 of this work was done by myself, with the assistance of J. E. Hawk, R. Hull, and Dr. C. Van Nest. All the experiments, data analysis, and preparation of the results were done by myself. All the new theory presented in this work was also developed by myself.

Part of Chapter 5 of this research is published as "Clustering mechanism of ethanol-water mixtures investigated with photothermal microfluidic cantilever deflection spectroscopy", Scientific Reports, Vol 6 (2016) 23966. Regarding this publication, I fabricated the devices, performed the experiments and prepared all the figures. I and J. E. Hawk wrote the manuscript. T. Thundat, M. S. Ghoraishi, J. E. Hawk and A. Phani contributed in scientific discussions. M. F. Khan assisted with experimental setup and design.

Acknowledgements

I would like to express my deep gratitude to my supervisor Prof. Thomas Thundat for all he has provided me during this program. I would also like to thank all the individuals who supported me during this adventure of my life.

To my loved ones:

Simin and Mohamad, who always supported me to be who I am.

Mojan and Mahdi, who always understood and inspired me.

John, who always helped me to see the positive anywhere.

Contents

List of Figures

List of Tables

List of Abbreviations

- IR: Infrared

- MIR: Mid Infrared

- PCDS: Photothermal Cantilever Deflection Spectroscopy

- BMC: Bi-Material Microfluidic Cantilever

- AFM: Atomic Force Microscopy

- RDX: Cyclotrimethylene Trinitramine

- TNT: Trinitrotoluene

- QCL: Quantum Cascade Laser

- FTIR: Fourier-Transform Infrared Spectroscopy

- ATR: Attenuated Total Reflection

- PMMA: Poly(methyl methacrylate)

- PC: Polycarbonate

- PDMS: Poly(dimethylsiloxane)

- SRN: Silicon Rich Silicon Nitride

- LPCVD: Low Pressure Chemical Vapor Deposition

- PECVD: Plasma-Enhanced Chemical Vapor Deposition

- RIE: Reactive Ion Etching

- KOH: Potassium Hydroxide

- Si: Silicon

- SiN: Silicon Nitride

- SiC: Silicon Carbide

- GaAs: Gallium Arsenide

- TMAH: Tetramethylammonium Hydroxide

- HMDS: Hexamethyldisilazane

- YES: Yield Engineering Systems

- DNQ: Diazonaphthoquinone

- NMR: Nuclear Magnetic Resonance

- HIM: Helium Ion Microscope

- PEEK: Polyether Ether Ketone

- PSD: Position Sensitive Diode

- EtOH: Ethanol

- NIST: National Institute of Standards and Technology

- VTMAs: Vibrational Transition Moment Angles

- MD: Molecular Dynamics

- FWHM: Full Width Half Maximum

- LDV: Laser Doppler Vibrometer

- UV-Vis: Ultraviolet–visible

Chapter 1:

Introduction

1.1. Objectives and scope

The innovative idea of developing a novel generation of generic microcantilevers (1) has motivated several groups around the world to focus their efforts on this new variety of the cantilever device. This resulted in different ongoing investigations on the applications of microfluidic based cantilevers in various fields.(2–7) This research is focused around the fabrication of microfluidic cantilevers, application of the device in IR spectroscopy, as well as actuation of the device by employing a system of electrolyte and AC voltage.

The first objective of this work was to fabricate several arrays of the microfluidic cantilevers with different geometries (i.e., length, width, thickness, and channel height) using single-sided polished Si-wafers to reduce the cost of fabrication. Knowing that a cantilever's sensitivity is a function of its geometry, fabricating the devices with different sizes provides flexibility in sensitivity and sampling size to conduct an analysis, where each type of the fabricated cantilever is suitable for a specific application.

The second objective of this work was to modify the fabricated cantilevers and employ them as a photothermal cantilever deflection spectroscopy (PCDS) platform, to collect IR spectra of ethanol-water mixtures. Following the success of this goal, the objective was enhanced with the aim of investigating the effect of intermolecular interactions between ethanol and water, on the IR absorption peaks of $C\text{-}C\text{-}O$ in 1000-

1200 cm^{-1} region. The obtained results were then explained with a simple model developed for this system.

As the thermal sensitivity of a bi-material microfluidic cantilever (BMC) plays a crucial role when the device is used to collect liquid spectra; the third objective of this work was to model the thermal sensitivity of the BMC. Although BMCs have been employed for several novel applications,(8–10) a theoretical understanding of its response to heat is still lacking. Adapting the approach developed by Timoshenko,(11) bending of a BMC resulting from thermally induced surface stresses was modeled in this thesis. To evaluate this new model, photothermal bending of two different microfluidic cantilevers were monitored as a function of IR radiation from 8.3 to 10.4 µm.

Among the different available methods, feedback loops and piezoelectric crystals have been employed as driving mechanisms for microfluidic cantilever resonators. However, because the device can confine various liquid samples, a combination of an electric field and the confined liquid can possibly be used to actuate the device. Thus, the last objective of this thesis was to actuate an electrolyte filled cantilever device by applying AC potential differences. To this end, the effect of several variables such as voltage, concentration, and the size of the device on the resonance amplitude of the cantilever was studied; nonetheless, there are yet many more questions to be answered regarding this system. This concept has interesting capability such as monitoring the concentration of an electrolyte in picoliter volume levels, because the driving force is the result of a complex interplay between the liquid and an electric field and it is concentration dependent.

More detailed objectives, related to the general aforementioned scopes, are presented at each chapters of this work.

1.2. Organization of the thesis

In this section, the outlines of the following chapters are laid out.

In Chapter 2, the knowledge on the basics of cantilever sensors in different modes of operation is presented to facilitate the discussions in the following chapters. In addition, the background knowledge on cantilever microfabrication and photothermal cantilever spectroscopy are briefly covered.

In Chapter 3, the fabrication process steps used to make the microfluidic cantilever are presented. Then, the performances of some of the fabricated microfluidic cantilevers in both dynamic and static mode are demonstrated. In the dynamic mode of operation, the performance of the device upon filling the cantilever with a liquid sample, as well as the changes in the frequency and quality factor as the device's dimension varies is presented. In the static mode of operation, only the performance of a BMC to the changes in temperature is examined, because the fabricated microcantilevers were used as a PCDS platform in this work. The deflection of the BMC is linearly proportional to the changes in temperature, which is similar to the linear deflection of a generic bi-material cantilever as a function of temperature. In addition, following the insight obtained during the fabrication of the microfluidic cantilevers, some suggestions are presented for improving the efficiency of the fabrication process.

In Chapter 4, IR spectrum of the confined ethanol-water mixtures that were collected using the photothermal cantilever deflection technique are presented. During the

measurements, the frequency of the device was monitored to confirm the presence of the liquid sample in the device. All the collected spectra show two distinguishable peaks in the 1000-1200 cm^{-1} region which are related to $C-C-O$ asymmetric stretch of the anti and gauche conformers of ethanol. Collected spectra were then analysed to study the effect of solvent-solute interactions on the absorption peaks. The results show that IR absorption peak positions for both conformers are a nonlinear function of ethanol concentration. To understand this nonlinearity, a simple model based on Hooke's law was developed. The model shows that the absorption peak positions are inversely related to the induced dipole moments in the mixture, resulting from changes in the concentration. This result matches our experimental result with a high accuracy.

In Chapter 5, the focus is on the static bending of the microfluidic cantilever due to the induced stress resulting from a mismatch of thermal expansions of the construction layers. Due to the significance of the thermal sensitivity of a bi-material microcantilever in calorimetric spectroscopy, an attempt was made to model the BMC's thermal sensitivity. Adapting the approach developed by Timoshenko,(11) bending of a uniformly heated BMC resulting from thermally induced surface stresses was modeled. This model was validated by the results of photothermal bending experiments carried out on two different designs of BMC where the microfluidic channel height is 1.6 or 3.1 μm. In addition, capability of the model to accurately predict thermal sensitivity and thermal bending of BMCs with different dimensions are presented.

Chapter 6 is focused on the actuation of an electrolyte-filled microfluidic cantilever device by applying AC potential differences. Two different electrolyte solutions (NaHSO$_4$ and NaCl solutions) were used for the study presented in this chapter. In

addition, the effect of the concentration, the strength of the applied AC voltage, the size of the microfluidic cantilever, the intrinsic charge on the device, and the frequency of the applied AC voltage in the obtained results were studied. The study shows that to actuate the cantilever, the frequency of the AC voltage must match the fundamental frequency of the device. At the matched frequencies, the applied voltage is directly proportional to the resonance amplitude. While the results indicate that the cantilever's surface charge does not play a considerable role in the cantilever's amplitude, the resonance amplitude is extremely affected as the device's size changes.

Lastly, a summary of the main observations in this work are presented in Chapter 7. In addition, bases on these observations, some suggestions for future research related to the studied field are proposed.

1.3.   References

1.   Burg TP, Manalis SR. Suspended microchannel resonators for biomolecular detection. Appl Phys Lett. 2003;83:2698–700.

2.   Burg TP, Godin M, Knudsen SM, Shen W, Carlson G, Foster JS, et al. Weighing of biomolecules, single cells and single nanoparticles in fluid. Nature. 2007;446(7139):1066–9.

3.   Bridle H, Wang W, Gavriilidou D, Amalou F, Hand DP, Shu W. Static mode microfluidic cantilevers for detection of waterborne pathogens. Sensors Actuators, A Phys. 2016;247:144–9.

4.   Khan MF, Schmid S, Davis ZJ, Dohn S, Boisen A. Fabrication of resonant micro cantilevers with integrated transparent fluidic channel. Microelectron Eng. 2011;88(8):2300–3.

5.   Manzoor Bukhari SA, Khan MF, Goswami A, McGee R, Thundat T. Thermomechanical analysis of picograms of polymers using a suspended microchannel cantilever. RSC Adv. 2017;7(14):8415–20.

6.   SadAbadi H, Packirisamy M. Nano-integrated suspended polymeric microfluidics (SPMF) platform for ultra-sensitive bio-molecular recognition of bovine growth hormones. Sci Rep. 2017;7:10969.

7.   Thundat T, Abraham R, Khan F, Kim S, Lee J. Time-of-flow micromechanical mass spectroscopy ans micromechanical infrared spectroscopy using microfluidic cantilever. Seattle, Washington: The Electrochemical Society; 2018. p. 2479.

8.   Ghoraishi MS, Hawk JE, Phani A, Khan MF, Thundat T. Clustering mechanism of ethanol- water mixtures investigated with photothermal microfluidic cantilever

deflection spectroscopy. Sci Rep. 2016;(23966).

9.   Etayash H, Khan MF, Kaur K, Thundat T. Microfluidic cantilever detects bacteria and measures their susceptibility to antibiotics in small confined volumes. Nat Commun. 2016;7(12947):1–9.

10.   Khan MF, Miriyala N, Lee J, Hassanpourfard M, Kumar A, Thundat T. Heat capacity measurements of sub-nanoliter volumes of liquids using bimaterial microchannel cantilevers. Appl Phys Lett. 2016;108(21).

11.   Timoshenko S. Analysis of bi-metal thermostats. J Opt Soc Am. 1925;11(3):233–55.

Chapter 2:

Background

2.1. Introduction

This chapter focuses on presenting the background knowledge relevant to this thesis. The knowledge on the basics of cantilever sensors in different modes of operation is highly relevant to the entire work demonstrated in this thesis. This knowledge helps to comprehend the relation between readout signals and specific phenomena that were investigated. The background knowledge on microfabrication and photothermal cantilever spectroscopy are specifically relevant to the work presented in Chapter 3 and Chapter 4, respectively.

2.2. Cantilever sensors

Cantilevers are among the simplest MEMS structures that can respond to different chemical, biological, or physical stimuli. They can be used as basic building blocks for more complex MEMS devices. Even though microcantilevers are very well known for their applications in atomic force microscopy (AFM), cantilevers with various geometries have been used for numerous molecular sensing applications since the 1940s.[1,2] For example, three geometries of cantilever devices are shown in Figure 2.1.[1]
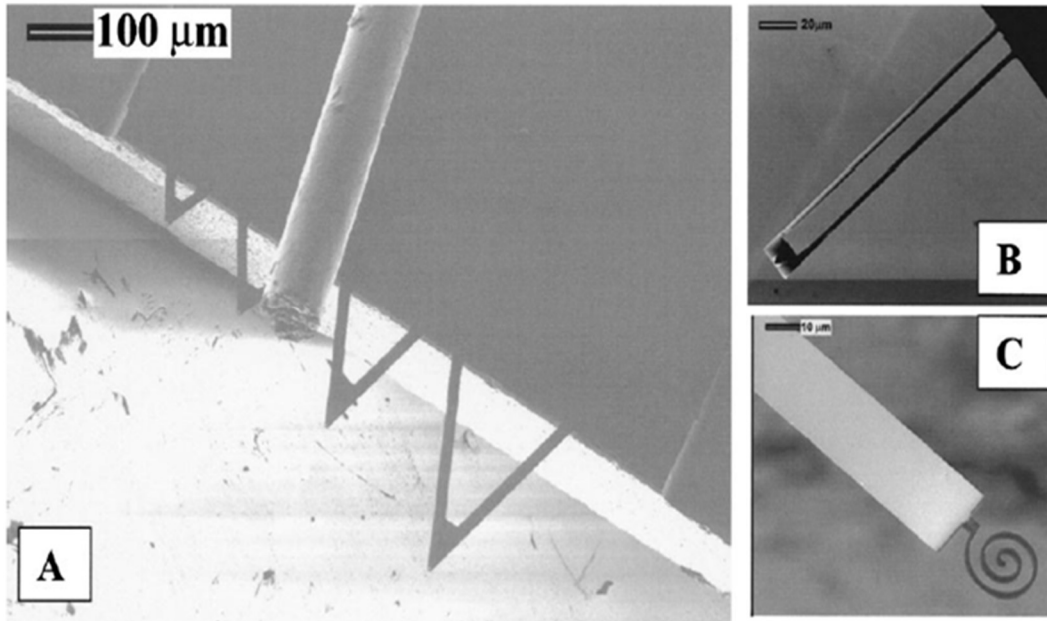
Figure 2.1. a) Commercially available AFM cantilevers. For comparison, a human hair is also included. b) and c) Modified cantilevers for calorimetric purposes (reprinted from Lavrik N V et al.(1) with permission from Copyright Clearance Center).

High sensitivity, low cost, diversity in size, shape, and material, and portability of the microcantilevers make them functional sensing platforms for significant applications in different media. Use of cantilever devices for gas phase analysis alone resulted in spectacular developments in the field of chemical sensing. Some examples are:

- Mercury vapors detection.(3)

- Humidity sensing using gelatin coated as well as poly(N-vinylpyrrolidinone) and poly(ethyleneglycol) coated cantilevers.(4,5)

- Ethanol vapor detection using Novolac-coated cantilevers.(6)

Despite the higher performance of the microcantilever sensors in gas phase, they have been employed for liquid phase sensing for different purposes, such as:

- To measure the pH of a solution using modified silicon and silicon nitride cantilevers for a pH range of 2-12.(7)

- To detect chemical compounds in aqueous electrolytes using AFM for force measurements.(8,9)

- To detect heavy metal ions such as Cs^+.(10)

- To detect aromatic as well as volatile organic compounds in aqueous solutions, such as 2,3-dihydroxynaphthalene, chloroform, and methylene chloride.(11,12)

Furthermore, combinations of cantilever sensors and surface modification techniques are used for numerous applications in bioscience.(13–17)

All the aforementioned applications of the cantilever sensors rely on operating the device in either static or dynamic mode. In the static mode of operation, deflection is the measured parameter, while in the dynamic mode, frequency and quality factor are the measured parameters. Any extrinsic or intrinsic stress on the cantilever results in a static deflection of the device, whereas frequency of the cantilever changes due to variations in the mass or viscoelastic properties. Figure 2.2 shows the conversion path between different input stimuli and resulting output signal, in either the static or dynamic mode of operation.(1,18–20)
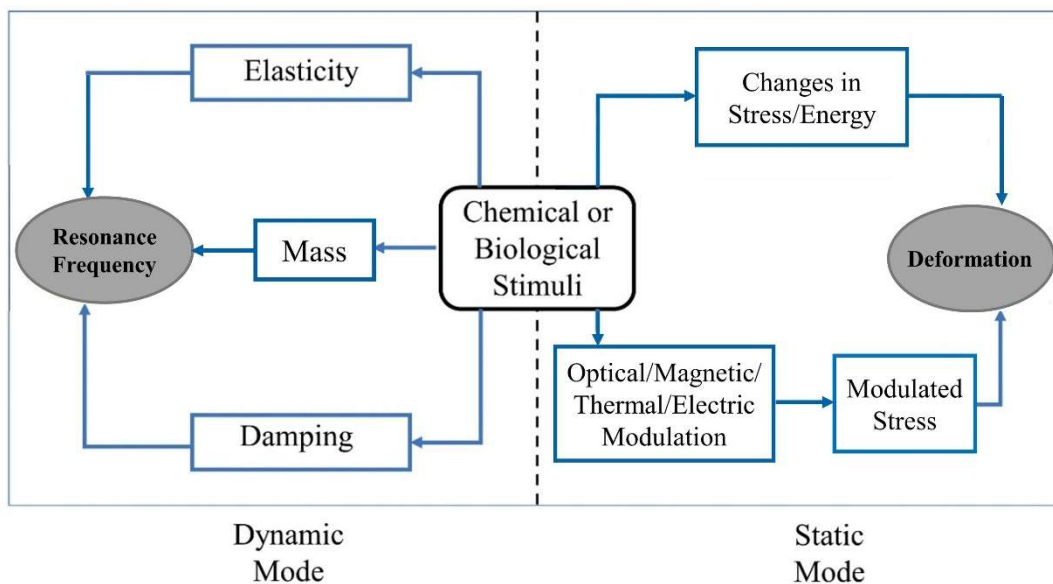
Figure 2.2. The interactions between the cantilever transducers and the environment are related to changes in either the static or dynamic response of the device.

In the static mode of cantilever operation, the deflection of the device is the main mechanical output. Such a deflection may have different origins such as thermal, electrical, and magnetic. Despite the origin of the force, the resulting mechanical stress created on the cantilever surface leads to the deflection of the device.(18,20–26) The capability of the cantilever sensors to relate different phenomena to a simple output signal (i.e., measurable static deflection of the device) makes them valuable devices for molecular level investigations in many fields. Here, a few examples are provided where different stimuli result in the cantilever's deflection:

- Swelling of nanoparticle coating due to application of a potential.(27)

- Chemisorption of molecules on coated cantilevers.(28)

- Swelling of the cantilever's coating after interaction with the analytes.(29–31)

- Temperature-induced stress in bi-material cantilevers.(32,33)

11

In Figure 2.3, resulting deflections of the cantilever due to either chemisorption of molecules or swelling of the coating are demonstrated.(1)

a)   b)
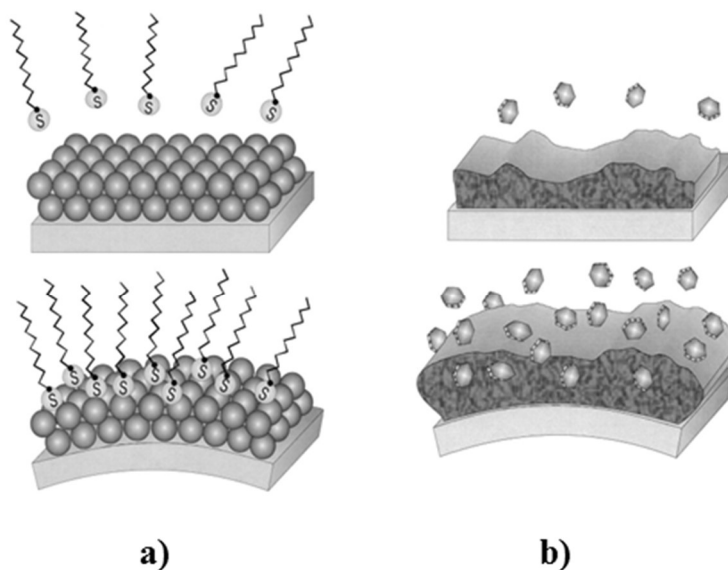
Figure 2.3. a) Bending schematic of a gold coated cantilever due to chemisorption of straight chain thiol molecules, b) the schematic of a cantilever's deformation after the analyte interacts with the responsive phase and makes it swell (reprinted from Lavrik N V et al.(1) with permission from Copyright Clearance Center).

Availability of a suitable model, to quantitatively analyze a microcantilever response to stress, depends on the specifics of the device and the origin of the applied stress. In many situations deflection of a cantilever due to surface stress can be predicted using modified Stoney's equation, developed in the beginning of the 20th century, where the radius of the curvature (R) of a substrate after the thin film deposition, is related to the changes in surface stress ($\Delta\sigma$), the thickness of the structure (t), Young's modulus (E), and Poisson's ratio (υ) (see Equation 2.1).(11,12,21,34)

$$\frac{1}{R} = \frac{6(1-\upsilon)}{Et^2}\Delta\sigma .$$

(2. 1)

In 1925, Timoshenko provided a general theory describing the bending of a bi-metal strip as a result of a uniform heating. The modified Timoshenko's equation was later used to relate bending (ΔZ) of bi-material cantilevers, consist of two layers with different thermal expansions, to the variations in temperature (ΔT) (see Equation 2.2).

$$\Delta Z = \frac{3l^2}{t_1+t_2}\left[\frac{\left(1+\frac{t_1}{t_2}\right)^2}{3\left(1+\frac{t_1}{t_2}\right)^2 + \left(1+\frac{t_1 E_1}{t_2 E_2}\right)\left(\frac{t_1^2}{t_2^2}+\frac{t_2 E_2}{t_1 E_1}\right)}\right](\gamma_1-\gamma_2)\Delta T ,$$

(2. 2)

where t_1 and t_2 are the thicknesses; E_1 and E_2 are Young's moduli; and γ_1 and γ_2 are thermal expansion coefficients of the two material layers.(1,35) In this work, photo-induced static deflection of modified microfluidic cantilevers was employed to explore ethanol-water interactions in liquid phase. Using microfluidic cantilevers for the purpose of photothermal spectroscopy not only improve the sensitivity, but also often can eliminate the need for surface functionalization of the device. In addition, because the final performance of this platform is directly related to its thermal sensitivity, in this work a new model was developed based on Timoshenko's model to explain this relation. The developed model is described in Chapter 5.

Unlike the static mode of operation where the static deflection of a cantilever reflects a change in the input signal, in the dynamic mode, frequency of the vibration and quality factor are the main measured parameters. When a cantilever is operated in the dynamic

mode, loaded mass and viscoelastic properties of the media change the resonance frequency of the device. Through modifying the device's geometry and materials, cantilevers with wide ranges of frequencies can be fabricated. Depending on the frequency of the vibration and the quality factor of the device, detection of femtogram mass is not outside the realm of possibilities.(36–39) In general, greater mass sensitivity is achieved by reducing the mass of the cantilever. However, operation of the cantilever sensor in higher vibrational modes can also improve the mass sensitivity. The first four modes of vibration for a cantilever sensor are shown in Figure 2.4. The resonance frequency of the nth vibrational mode ($f_{R,n}$) can be related to the material and geometrical properties of the cantilever by (40–43)

$$f_{R,n} = \frac{\kappa_n^2}{l^2(2\pi)}\sqrt{\frac{EI}{\rho A}}, \qquad (2.3)$$

where

E = Elastic modulus of the material,

ρ = Mass density,

I = Moment of inertia of the cantilever,

l = Cantilever's length,

A = Cantilever' cross sectional area, and

κ_n = Constant for mode n ($\kappa_1 = 1.87$, $\kappa_2 = 4.69$, $\kappa_3 = 7.69$, and $\kappa_n = \pi(n - 0.5)$).

In this work, fabricated microfluidic cantilevers were used in their first vibrational mode to investigate ion interactions with an external electric field, while monitoring the

amplitude of the vibration. The amplitude of vibration of a cantilever device driven by an external force (F_0) is given by

$$A = \frac{F_0}{\sqrt{\left(k - m\omega^2\right)^2 + c^2\omega^2}} \, ,$$
(2. 4)

where k, m, ω, and c are spring constant, mass, undamped natural frequency, and damping constant, respectively.(44)
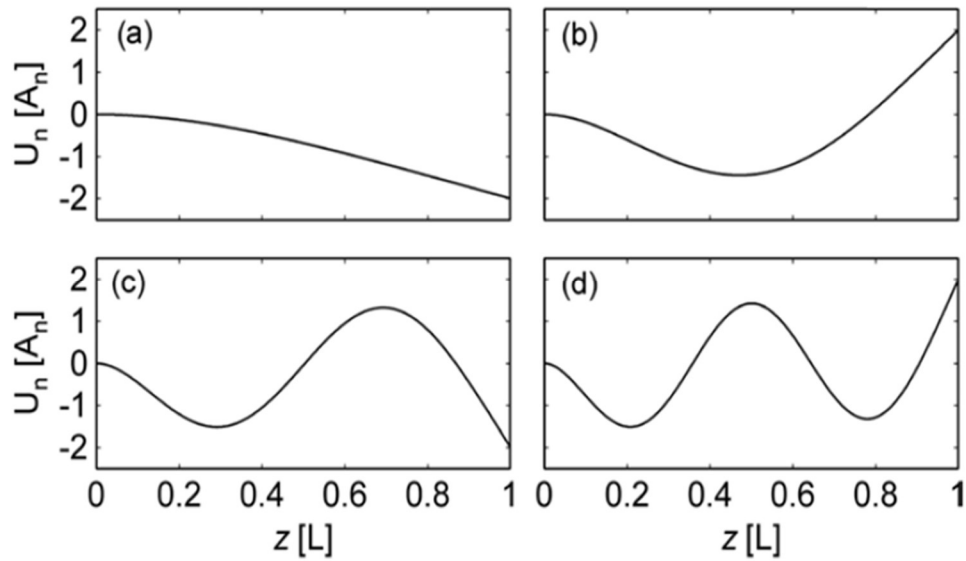
Figure 2.4. The side view schematics of the first four bending vibrational modes of a cantilever device. The amplitude of the vibration presented in units of A_n, along the length of the cantilever (L). The point L=0 refers to the base of the cantilever. The figure illustrates that there are certain points along the length of the device which do not vibrate (i.e., nodal points) (reprinted from Boisen A et al.(43) with permission from Copyright Clearance Center).

2.3. Photothermal cantilever deflection spectroscopy

Photothermal spectroscopy is based on tracking photo-induced variations in the thermal state of a sample. Various methods are employed to monitor a parameter associated with sample heating. For example, photothermal deflection is based on monitoring changes in a refractive index resulted from sample heating. Alternatively, changes in the sample temperature can be monitored by utilizing a temperature transducer in calorimetric methods.(45)

In 1993, Gimzewski JK et al. introduced a new form of calorimeter with an approximate sensitivity of 1pJ. This calorimeter was built upon the bending of an aluminum coated silicon-based micromechanical cantilever sensor. As O_2 reacts with H_2, over a Pt surface coated on the aluminum layer, some heat evolves in the system. This resulted in a thermally induced bending of the highly sensitive microcantilever, due to unequal thermal expansion of the aluminum and silicon layers. The sample heating was measured by monitoring the bending of the cantilever. A schematic diagram of the device, used for the purpose of calorimetry, is shown in Figure 2.5.(32)
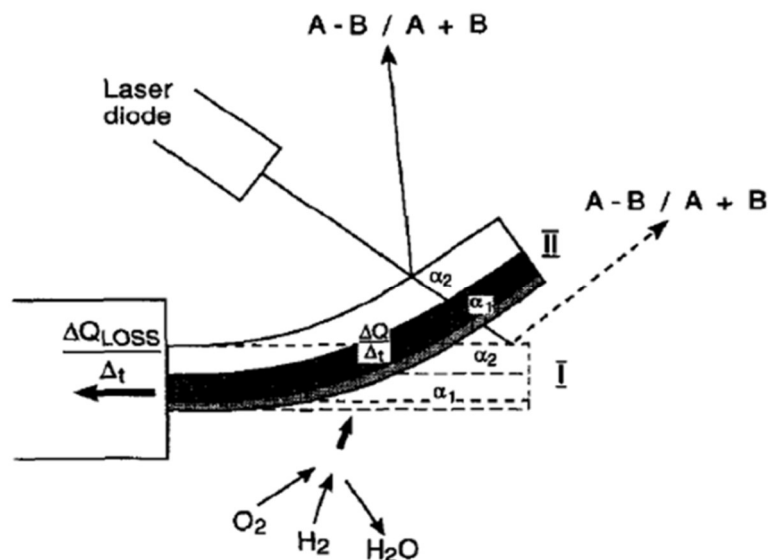
Figure 2.5. The schematic of the cantilever device used by Gimzewski JK et al. for the purpose of calorimetry. White shows the silicon layer, black shows the aluminum layer, and gray bottom layer shows Pt coating. As O_2 reacts with H_2, over a Pt catalytic layer, the heat of the reaction results in the microcantilever bending. This bending was monitored by tracking the position of a reflected optical beam off the lever into a position sensitive detector (reprinted from Gimzewski JK et al.(32) with permission from Copyright Clearance Center).

Later, the same group applied this cantilever-based calorimeter approach to monitor photo-induced changes in the thermal state of dye molecules. After the molecule absorbs light and gets excited to a higher energy level, some of the absorbed energy releases in the form of heat, during the relaxation process. Monitoring the cantilever bending as a function of the illumination wavelength provides the spectral response of the sample. Though the idea of measuring photo-induced heat was not new, using a bi-material cantilever transducer for this purpose was original. This novel idea enabled Gimzewski and coworkers to achieve a power sensitivity of 100 pW, which is two orders of magnitude better than the older methods, for example, monitoring the refractive index of

17

liquid positioned close to the sample was used to detect heat. Figure 2.6 shows the photothermal spectrum of a fluorescent dye, fluorescein, obtained when using microcantilevers by Branes et al.(33)
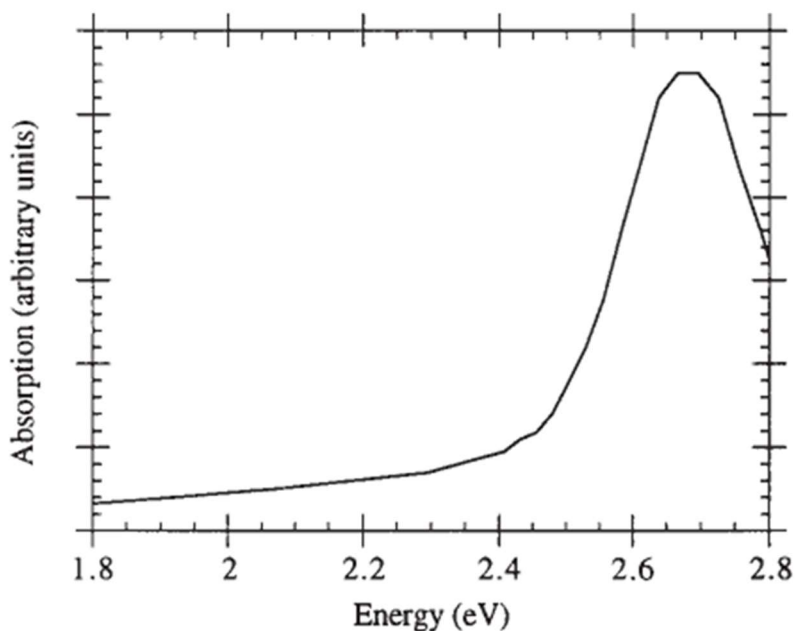
Figure 2.6. The photothermal absorption spectra of fluorescein dye, deposited as a monolayer on the cantilever sensor. Fluorescein dye has an absorption peak at 469 nm (i.e., 2.65 eV) and emission at 509 nm (i.e., 2.44 eV) (reprinted from Barnes JR et al.(33) with permission from Copyright Clearance Center).

In pursuit of improving the previous studies, Varesi J et al. were able to enhance the power sensitivity of a cantilever-based calorimeter by nearly an order of magnitude. This was achieved through optimizing the thickness ratio of the cantilever's constructing layers as well as using a higher modulation frequency for the incident radiation.(46) In 2013, Canetta and Narayanaswamy improved the heat sensitivity even further, up to 1 pW, by reducing the conductance of the cantilever to 153 nW/K.(47) Due to the high

sensitivity of bi-metallic microcantilevers to heat, this platform has been employed for many different applications, including:

- Detection of subnanograms of cyclotrimethylene trinitramine (RDX) and trinitrotoluene (TNT).(48)

- Detection of nanograms quantities of fatal Bacillus anthracis (known as anthrax).(49)

- Spectroscopic measurements in a wide range of wavelengths (i.e., from ultraviolet to the MIR).(50)

- Sensing generated heat by a single mammalian cell.(51)

- Fabrication of uncooled infrared camera for IR imaging.(52)

- Detection of chemicals such as tetrachloroethylene, dimethylnaphthalene, 1,8-dimethylnaphthalene, and trichloroethylene by combining adsorption-induced and photo-induced stresses.(53)

The aforementioned examples demonstrate high sensitivity of the photothermal spectroscopy measurement and its applicability for different types of materials, with no limitation on the transparency. In addition, this technique is non-destructive and non-contact with operational capability in both air and vacuum.

Even though the cantilever-based spectrometer is a very promising platform, it is not suitable for spectroscopy measurements in liquid phase, especially water media. This is mainly because operation of the device in liquid media decreases the sensitivity significantly. This challenge can be overcome by confining the liquid in a bi-material microfluidic cantilever platform. Simultaneously, the low resolution, as well as low signal to noise ratio of MIR spectroscopy in aqueous media, can be addressed by employing a

quantum cascade laser as the light source. This idea was used in this work to extract detailed information on intermolecular interactions between ethanol and water as the IR spectra of the mixture were collected.

2.3.1.   Quantum cascade laser (QCL)

A QCL, introduced in 1994 by Faist J et al., is a semiconductor laser that operates based on electronic transitions within the conduction bands.(54) Such a laser source has the advantages of room temperature operation, portability, and high power which make QCLs very promising sources for gas sensing applications.(55–57) They also offer significant advantages when it is required to perform liquid phase measurements.

QCLs can allow to solve the difficulty of conducting MIR spectroscopy on aqueous solutions. Although IR spectroscopy is a universal technique capable of revealing molecule-specific information, it suffers from strong absorptions of water in the MIR region. For example, the absorption related to the bending vibration of water in the MIR region prevents acquisition of useful information on the amid-I band of proteins. Therefore, optical paths are limited to less than 10 μm for reliable measurements, using Fourier-transform infrared spectroscopy (FTIR), in this spectral region. Dedicated transmission cells and attenuated total reflection (ATR) technique offer a short optical path for spectroscopy measurements. However, reducing the optical path results in poor sensitivity. By replacing the light source in MIR spectroscopy with a QCL, the optical path length and sensitivity can be improved.(58–61) Performing IR spectroscopy on highly sensitive cantilever platforms while using a QCL as the light source can further improve the sensitivity of MIR spectroscopy.

2.4.   Microfabrication

Complex mechanical parts such as membranes, sensors, actuators, pumps, and electronic parts are common examples of MEMS. In general, bulk micromachining and surface micromachining are two predominant technological processes underlying MEMS. The process of microfabrication of MEMS devices can be used to either fabricate a single device or thousands of devices. Batch processing not only reduces the cost of individual devices, but also minimizes the dimensional variations.(62–64)

Size, dimensional reproducibility, and the material used to construct a sensor control the final performance and applications of the device. Microfabrication techniques make it possible to achieve small device size, resulting in a small sampling volume, required for many chemical and biological sensors. Also, as a result of precise control over the geometry during the fabrication steps, high reproducibility of the fabricated devices is easy to achieve.(62,64–66) Depending on the requirements of the device, different materials, or combination of materials, have been employed in the microfabrication processes. Examples include:

- Polymers such as photoresist SU-8, poly(methyl methacrylate) (PMMA), polycarbonate (PC), poly(dimethylsiloxane) (PDMS), and Polyimide.(67,68)

- Silicon material such as silicon oxide, silicon nitride, polycrystalline silicon (polysilicon), and silicon rich silicon nitride (SRN).(63,64,69,70)

- Metal films such as gold, Nickel, and Titanium.(64,71–73)

Among the different materials available for fabrication of microcantilever based sensors, silicon materials are the most preferred substrates where low pressure chemical vapor deposition (LPCVD) and plasma-enhanced chemical vapor deposition (PECVD) are

often employed to form a silicon-based film. However, it is worth mentioning that recently, material such as graphene and diamond-like carbon have been offered as promising alternatives to silicon.(74,75)

2.4.1.   Cantilever fabrication

Fabrication of resonant microstructures, including microcantilever sensors, can be summarized into deposition, patterning, and etching. During the deposition, a selected material will be deposited on a single crystal silicon wafer with a thickness of 350–500 µm. It is important to modify the conditions of the deposition process in order to minimize the stress and subsequent deformations developed in the device during the fabrication. Lateral sizes of the device are usually defined by the thicknesses of the deposited films; whereas, in plane geometries are defined during patterning steps. Patterning steps for a micrometer size cantilever include UV lithography that is followed by reactive ion etching (RIE) of the deposited layer. However, to fabricate a nanoscale cantilever, electron beam lithography is employed as a substitute to UV lithography. Eventually, the cantilever device will be released by either etching away the sacrificial layer (surface micromachining) or etching through the bulk of the wafer from the backside (bulk micromachining). Fabrication of a standard cantilever using a sacrificial layer, is demonstrated in Figure 2.7. (76,77)
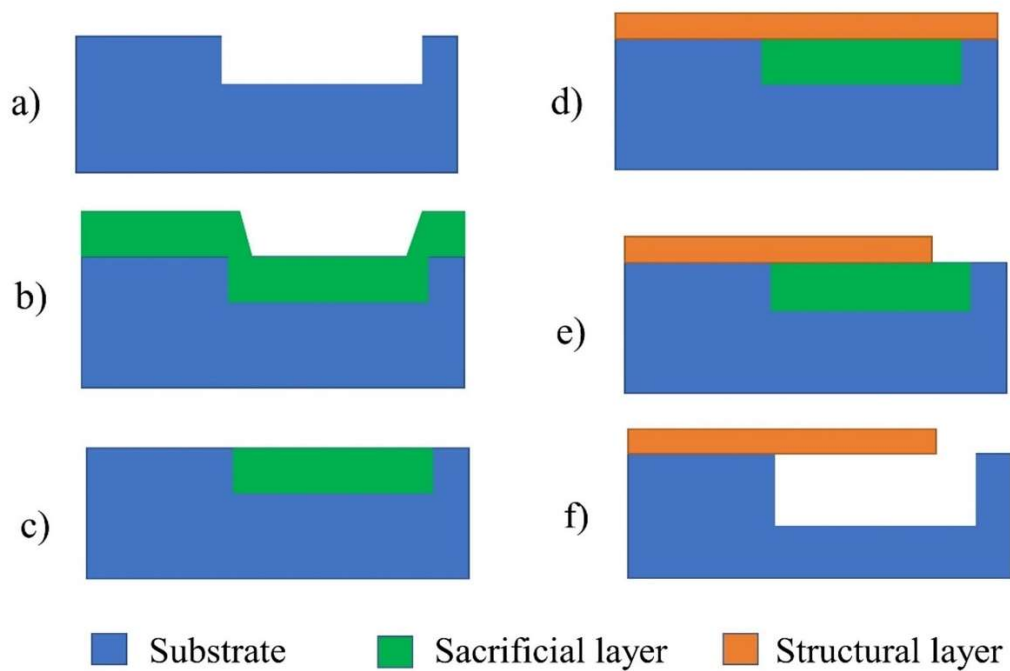
Figure 2.7. Fabrication steps using surface micromachining where patterning of the silicon substrate is followed with deposition of a sacrificial layer which will be removed in the final step. The cantilever in plane geometry is defined by patterning the structural layer located on top of the sacrificial layer, a) substrate patterning and etching, b) deposition of a sacrificial layer, c) planarization, d) deposition of a structural layer, e) patterning the structural layer, and f) removal of the sacrificial layer.

Using a sacrificial layer helps to eliminate the need for through-wafer etching of the silicon in potassium hydroxide (KOH), which is time consuming. When using a sacrificial layer, under-etch rate is generally low because the etchant has little access to this layer. However, the cantilever is often vulnerable to adhesion to the underneath substrate since there is a small gap between the two. This phenomenon is called release

stiction. Also, the need for a sacrificial layer limits material choice in the fabrication process.(43,77–80)

The etch-through process of releasing a cantilever does, however, have the advantages of allowing both sides of the device to be easily accessed for inspections. In bulk micromachining, an etch stop layer is required. The etch stop layer will protect the device from being etched during the back side etching, using KOH etching or reactive ion etching, and must be removed in a later step to release the cantilever. For comparison, microfabrication of a cantilever fabricated on a standard silicon wafer, based on bulk micromachining is presented in Figure 2.8. (76,77)
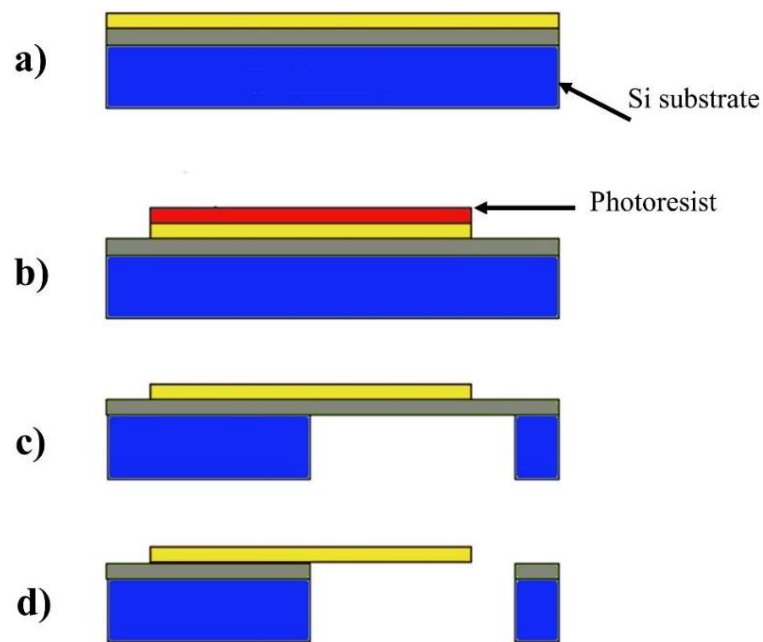
Figure 2.8. Step process in bulk microfabrication of a silicon-based cantilever: a) deposition of structural layer, b) patterning of the device by photolithography and subsequent etching, c) release of the cantilever device by etching through the wafer from the backside, and d) removing the etch stop layer. Blue, gray, yellow, and red represent silicon wafer, etch stop layer, silicon-based cantilever, and photoresist, respectively.

To investigate the potential applications of a cantilever device for chemical or biological sensing as well as measuring properties of liquid samples, the operation of the device in liquid phase is required. However, the viscosity of the liquid causes an obstruction to precisely measure the frequency response of conventional microcantilevers. Strong damping of a cantilever device in a liquid environment, as opposed to vacuum, reduces the quality factor of the device up to five orders of magnitude. This results in broadening of the frequency response of devices in liquid and consequently attenuates the vibration amplitude.(81,82) This limitation can be overcome by embedding a channel in a microcantilever where a liquid sample can be confined.(83)

Microcantilevers with embedded channels attracted scientific communities to analyze liquid samples. This is mainly because they maintain a high quality factor usually achievable only with vacuum environments. Improvement to the quality factor is a result of exposing the outside of the device to air or vacuum.(84–89)

Depending on the final requirements of the device, different techniques can be employed to fabricate micro-resonators with embedded channels. Sacrificial layer methods are commonly used when it is required to minimize the mass of the resonator. When using this method, a material which can be easily etched is deposited on a substrate as a sacrificial material. This material is patterned, and thereafter encapsulated, with the structural material of the cantilever. Photolithography is usually used to pattern openings which give access to the sacrificial layer in the etching step where a microfluidic channel forms. To create the cantilever resonator, a part of the channel is then undercut. (83,90,91)

When using a sacrificial technique to fabricate micro-resonators, a high etch rate selectivity between the structural layer and the sacrificial layer is necessary. This is

mainly because of the substantial length of the microfluidic channel. To ensure a high etch rate selectivity, selection of the materials for each layer plays an important role. For example, aluminum and passivation dielectrics were used for sacrificial and structural material, respectively, to fabricate several hundreds of micrometer long channels. Also, a combination of low-stress silicon nitride and polysilicon were used as structural and sacrificial material to fabricate microfluidic cantilevers.(92) A sacrificial based method was used in this work for fabrication of microfluidic cantilevers with different sizes to investigate liquid samples, as explained in chapters 4 and 6.

The injection moulding process and 3D printing also became impressive alternatives to the classical surface micromachining and have been used for fabrication of polymeric microcantilevers. For example, McFarland AW et al. successfully fabricated polymeric microcantilever from polystyrene, polypropylene, and nanoclay polymer composite with thicknesses ranging from 2 to 40 μm, an aspect ratio (i.e., length/thickness) of more than 170, and spring constants from 0.01 to 10 N/m.(93–97) Table 2.1 compares properties of different materials commonly used for fabrication of cantilever sensors as well as properties of fabricated microcantilever devices.(43)

Table 2.1. Comparison of cantilever materials as well as fabrication methods. Si is crystalline silicon and SiN is LPCVD silicon nitride.(43)

Material	Si	SiN	SU-8	Polystyrene
Cantilever fabrication				
Fabrication method	Etching	Etching	UV	Injection
Fabrication costs	High	High	Medium	Low
Cantilever properties				
Thickness	500 nm	500 nm	2 μm	5 μm
Young's modulus	180 GPa	290 GPa	4 GPa	3 GPa
Poisson's ratio	0.28	0.27	0.22	0.34
Spring constant	4.5 mNm	7.3 mNm	6.4 mNm	75 mNm
Resonance frequency	2.8 kHz	3.2 kHz	2.4 kHz	5.5 kHz
Surface stress sensitivity $\Delta z / \Delta \sigma$	12 m^2/N	7.6 m^2/N	36.6 m^2/N	6.6 m^2/N
Mass sensitivity $\Delta f / \Delta m$	24.4 Hz/ng	21.2 Hz/ng	10. Hz/ng	10.6 Hz/ng
Measurements				
Reflection of optical beams without metal	High	High	Low	Low
Moisture absorption	Low	Low	High	Medium
Time-stability	Years	Years	Months	——

2.5.   References

1.   Lavrik N V., Sepaniak MJ, Datskos PG. Cantilever transducers as a platform for chemical and biological sensors. Rev Sci Instrum. 2004;75(7):2229–53.

2.   Binnig G, Quate CF. Atomic force microscope. Phys Rev Lett. 1986;56(9):930–3.

3.   Thundat T, Wachter EA, Sharp SL, Warmack RJ. Detection of mercury vapor using resonating microcantilevers. Appl Phys Lett. 1995;66:1695–7.

4.   Thundat T, Chen GY, Warmack RJ, Allison DP, Wachter E a. Vapor detection using resonating microcantilevers. Anal Chem. 1995;67(3):519–21.

5.   Ferrari V, Marioli D, Taroni A, Ranucci E, Ferruti P. Development and application of mass sensors based on flexural resonances in alumina beams. IEEE Trans Ultrason Ferroelectr Freq Control. 1996;43(4):601–8.

6.   Adams JD, Parrott G, Bauer C, Sant T, Manning L, Jones M, et al. Nanowatt chemical vapor detection with a self-sensing, piezoelectric microcantilever array. Appl Phys Lett. 2003;83(16):3428–30.

7.   Ji HF, Hansen KM, Hu Z, Thundat T. Detection of pH variation using modified microcantilever sensors. Sensors Actuators, B Chem. 2001;72(3):233–8.

8.   Butt HJ, Jaschke M, Ducker W. Measuring surface forces in aqueous electrolyte solution with the atomic force microscope. Bioelectrochemistry Bioenerg. 1995;38(1):191–201.

9.   Söngen H, Marutschke C, Spijker P, Holmgren E, Hermes I, Bechstein R, et al. Chemical identification at the solid–liquid interface. Langmuir. 2017;33(1):125–9.

10.   Ji H-F, Dabestani R, Thundat T, Brown GM, Britt PF. A novel self-assembled

monolayer (SAM) coated microcantilever for low level caesium detection. Chem Commun. 2000;(6):457–8.

11. Tipple CA, Lavrik N V., Culha M, Headrick J, Datskos P, Sepaniak MJ. Nanostructured microcantilevers with functionalized cyclodextrin receptor phases: Self-assembled monolayers and vapor-deposited films. Anal Chem. 2002;74(13):3118–26.

12. Headrick JJ, Sepaniak MJ, Lavrik N V., Datskos PG. Enhancing chemi-mechanical transduction in microcantilever chemical sensing by surface modification. Ultramicroscopy. 2003;97(1–4):417–24.

13. Subramanian A, Oden PI, Kennel SJ, Jacobson KB, Warmack RJ, Thundat T, et al. Glucose biosensing using an enzyme-coated microcantilever. Appl Phys Lett. 2002;81(2):385–7.

14. Hansen KM, Ji HF, Wu G, Datar R, Cote R, Majumdar A, et al. Cantilever-based optical deflection assay for discrimination of DNA single-nucleotide mismatches. Anal Chem. 2001;73(7):1567–71.

15. Raiteri R, Grattarola M, Butt HJ, Skládal P. Micromechanical cantilever-based biosensors. Sensors Actuators B Chem. 2001;79(2–3):115–26.

16. Baselt DR, Lee GU, Colton RJ. Biosensor based on force microscope technology. J Vac Sci Technol B. 1996;14(2):789–93.

17. Baselt DR, Lee GU, Hansen KM, Chrisey LA, Colton RJ. A high-sensitivity micromachined biosensor. Proc IEEE. 1997;85(4):672–80.

18. Fritz J, Baller MK, Lang HP, Rothuizen H, Vettiger P, Meyer E, et al. Translating biomolecular recognition into nanomechanics. Science. 2000;288(5464):316–8.

19.   Wachter EA, Thundat T. Micromechanical sensors for chemical and physical measurements. Rev Sci Instrum. 1995;66(6):3662–7.

20.   Betts TA, Tipple CA, Sepaniak MJ, Datskos PG. Selectivity of chemical sensors based on micro-cantilevers coated with thin polymer films. Anal Chim Acta. 2000;422(1):89–99.

21.   Sader JE. Surface stress induced deflections of cantilever plates with applications to the atomic force microscope: Rectangular plates. J Appl Phys. 2001;89(5):2911–21.

22.   Sader JE. Surface stress induced deflections of cantilever plates with applications to the atomic force microscope: V-shaped plates. J Appl Phys. 2002;91(11):9354–61.

23.   Miyatani T, Fujihira M. Calibration of surface stress measurements with atomic force microscopy. J Appl Phys. 1997;81(11):7099–115.

24.   Hu Z, Thundat T, Warmack RJ. Investigation of adsorption and absorption-induced stresses using microcantilever sensors. J Appl Phys. 2001;90(1):427–31.

25.   Godin M, Tabard-Cossa V, Grütter P, Williams P. Quantitative surface stress measurements using a microcantilever. Appl Phys Lett. 2001;79(4):551–3.

26.   Fang W. Determination of the elastic modulus of thin film materials using self-deformed micromachined cantilevers. J Micromechanics Microengineering. 1999;9(3):230–5.

27.   Raguse B, Müller KH, Wieczorek L. Nanoparticle actuators. Adv Mater. 2003;15(11):922–6.

28.   Yang R, Huang X, Wang Z, Zhou Y, Liu L. A chemisorption-based

microcantilever chemical sensor for the detection of trimethylamine. Sensors Actuators, B Chem. 2010;145(1):474–9.

29.   Fagan BC, Tipple CA, Xue Z, Sepaniak MJ, Datskos PG. Modification of micro-cantilever sensors with sol-gels to enhance performance and immobilize chemically selective phases. Talanta. 2000;53(3):599–608.

30.   Snow D, Weeks BL, Kim DJ, Loui A, Hart BR, Hope-Weeks LJ. Static deflection measurements of cantilever arrays reveal polymer film expansion and contraction. J Colloid Interface Sci. 2007;316(2):687–93.

31.   Then D, Vidic A, Ziegler C. A highly sensitive self-oscillating cantilever array for the quantitative and qualitative analysis of organic vapor mixtures. Sensors Actuators, B Chem. 2006;117(1):1–9.

32.   Gimzewski JK, Gerber C, Meyer E, Schlittler RR. Observation of a chemical-reaction using a micromechanical sensor. Chem Phys Lett. 1994;217(5–6):589–94.

33.   Barnes JR, Stephenson RJ, Welland ME, Gerber C, Gimzewski JK. Photothermal spectroscopy with femtojoule sensitivity using a micromechanical device. Nature. 1994;372:79–81.

34.   Stoney G. The tension of metallic films deposited by electrolysis. Proc R Soc London. 1909;82(553):172–5.

35.   Timoshenko BYS. Analysis of bi-metal thermostats. J Opt A. 1925;11(l):233–55.

36.   Ilic B, Czaplewski D, Zalalutdinov M, Craighead HG, Neuzil P, Campagnolo C, et al. Single cell detection with micromechanical oscillators. J Vac Sci Technol B. 2001;19(6):2825–8.

37. Oden PI. Gravimetric sensing of metallic deposits using an end-loaded microfabricated beam structure. Sensors Actuators, B Chem. 1998;53(3):191–6.

38. Lavrik N V., Datskos PG. Femtogram mass detection using photothermally actuated nanomechanical resonators. Appl Phys Lett. 2003;82(16):2697–9.

39. Thundat T, Warmack RJ, Chen GY, Allison DP. Thermal and ambient-induced deflections of scanning force microscope cantilevers. Appl Phys Lett. 1994;64(21):2894–6.

40. Ghatkesar MK, BarGhatkesar MK, Barwich V, Braun T, Ramseyer J-P, Gerber C, et al. Higher modes of vibration increase mass sensitivity in nanomechanical microcantilevers. Nanotechnology. 2007;18(44):445502.

41. Dohn S, Sandberg R, Svendsen W, Boisen A. Enhanced functionality of cantilever based mass sensors using higher modes and functionalized particles. Appl Phys Lett. 2005;86:233501–3.

42. Sarid D. Scanning force microscopy with applications to electric, magnetic, and atomic forces. New York: Oxford university press; 1991.

43. Boisen A, Dohn S, Keller SS, Schmid S, Tenje M. Cantilever-like micromechanical sensors. Reports Prog Phys. 2011;74(3):36101.

44. Rao SS. Mechanical vibrations, fifth edition. Upper Saddle River, N.J.: Pearson Prentice Hall; 2011.

45. Bialkowski SE. Photothermal spectroscopy methods for chemical analysis. New York: Wiley; 1996.

46. Varesi J, Lai J, Perazzo T, Shi Z, Majumdar A. Photothermal measurements at picowatt resolution using uncooled micro-optomechanical sensors. Appl Phys

Lett. 1997;71(3):306–8.

47.   Canetta C, Narayanaswamy A. Sub-picowatt resolution calorimetry with a bi-material microcantilever sensor. Appl Phys Lett. 2013;102(10):103112–4.

48.   Krause AR, Van Neste C, Senesac L, Thundat T, Finot E. Trace explosive detection using photothermal deflection spectroscopy. J Appl Phys. 2008;103(9):094906–6.

49.   Wig A, Arakawa ET, Passian A, Ferrell TL, Thundat T. Photothermal spectroscopy of Bacillus anthracis and Bacillus cereus with microcantilevers. Sensors Actuators, B Chem. 2006;114(1):206–11.

50.   Li G, Burggraf LW, Baker WP. Photothermal spectroscopy using multilayer cantilever for chemical detection. Appl Phys Lett. 2000;76(9):1122–4.

51.   Voiculescu I, Liu F, Ono T, Toda M. Investigation of bimaterial cantilever beam for heat sensing in liquid. Sensors Actuators, A Phys. 2016;242:58–66.

52.   Perazzo T, Mao M, Kwon O, Majumdar A, Varesi JB, Norton P. Infrared vision using uncooled micro-optomechanical camera. Appl Phys Lett. 1999;74(23):3567–9.

53.   Datskos PG, Rajic S, Sepaniak MJ, Lavrik N, Tipple CA, Senesac Datskou LR. Chemical detection based on adsorption-induced and photoinduced stresses in microelectromechanical systems devices. J Vac Sci Technol B. 2001;19(2001):1173–9.

54.   Faist J, Capasso F, Sivco DL, Sirtori C, Hutchinson AL, Cho AY. Quantum cascade laser. Science. 1994;264(5158):553–6.

55.   Sigrist MW, Bartlome R, Marinov D, Rey JM, Vogler DE, Wächter H. Trace gas

monitoring with infrared laser-based detection schemes. Appl Phys B Lasers Opt. 2008;90(2):289–300.

56. Gmachi C, Capasso F, Sivco DL, Cho AY. Recent progress in quantum cascade lasers and applications. Reports Prog Phys. 2001;64:1533–601.

57. Hodgkinson J, Tatam RP. Optical gas sensing: a review. Meas Sci Technol. 2013;24(1):012004 (1-59).

58. Kölhed M, Haberkorn M, Pustogov V, Mizaikoff B, Frank J, Karlberg B, et al. Assessment of quantum cascade lasers as mid infrared light sources for measurement of aqueous samples. Vib Spectrosc. 2002;29(1–2):283–9.

59. Schaden S, Haberkorn M, Frank J, Baena JR, Lendl B. Direct determination of carbon dioxide in aqueous solution using mid-infrared quantum cascade lasers. 2004;58(6):667–70.

60. Lendl B, Reidl-Leuthner C, Ritter W. Mid-IR quantum cascade lasers as an enabling technology for a new generation of chemical analyzers for liquids. In: Proceeding of SPIE. San Francisco; 2011.

61. Koelhed M, Lendl B, Karlberg B. On-line infrared detection in aqueous micro-volume systems. Analyst. 2003;128(1):2–6.

62. Maboudian R. Surface processes in MEMS technology. Surf Sci Rep. 1998;30:207–69.

63. Hierlemann A, Brand O, Hagleitner C, Baltes H. Microfabrication techniques for chemical/biosensors. In: Proceedings of the IEEE. 2003. p. 839–63.

64. Deisingh AK. MEMS technology in analytical chemistry. Analyst. 2003;128(1):9–11.

65.   Lang W. Silicon microstructuring technology. Mater Sci Eng R-Reports. 1996;17(1):1–55.

66.   Weibel DB, Diluzio WR, Whitesides GM. Microfabrication meets microbiology. Nat Rev Microbiol. 2007;5(3):209–18.

67.   Kim BJ, Meng E. Review of polymer MEMS micromachining. J Micromechanics Microengineering. 2016;26(1):1–20.

68.   Becker H, Gärtner C. Polymer microfabrication technologies for microfluidic systems. Anal Bioanal Chem. 2008;390(1):89–111.

69.   Desai TA, Hansford D, Ferrari M. Characterization of micromachined silicon membranes for immunoisolation and bioseparation applications. J Memb Sci. 1999;159(1–2):221–31.

70.   Abgrall P, Gué A-M. Lab-on-chip technologies: making a microfluidic network and coupling it into a complete microsystem—a review. J Micromechanics Microengineering. 2007;17:R15–49.

71.   Zhang KL, Chou SK, Ang SS, Tang XS. A MEMS-based solid propellant microthruster with Au/Ti igniter. Sensors Actuators A Phys. 2005;122:113–23.

72.   Xu D, Wang L, Ding G, Zhou Y, Yu A, Cai B. Characteristics and fabrication of NiTi/Si diaphragm micropump. Sensors Actuators A Phys. 2001;93(1):87–92.

73.   Lee D, Wei X, Chen X, Zhao M, Jun SC, Hone J, et al. Microfabrication and mechanical properties of nanoporous gold at the nanoscale. Scr Mater. 2007;56(5):437–40.

74.   Geim AK, Novoselov KS. The rise of graphene. Nat Mater. 2007;6(3):183–91.

75.   Robertson J. Diamond-like amorphous carbon. Mater Sci Eng R Reports.

2002;37(4–6):129–281.

76.   M A McCord and M J Rooks. Handbook of microlithography, micromachining and microfabrication. Bellingham, Washington: SPIE Optical Engineering Press; 1997.

77.   Madou M. Fundamentals of microfabrication. Boca Raton, Fla: CRC press; 1997.

78.   Brugger J, Beljakovic G, Despont M, Rooij NF, Vettiger P. Silicon micro/nanomechanical device fabrication based on focused ion beam surface modification and KOH etching. Microelectron Eng. 1997;35:401–4.

79.   Steckl AJ, Mogul HC, Mogren S. Localized fabrication implantation of Si nanostructures by focused ion beam. Appl Phys Lett. 1992;60:1833–5.

80.   Bustillo JM, Howe RT, Muller RS. Surface micromachining for microelectromechanical systems. Ultramicroscopy. 1988;86(8): 1552-1574.

81.   Sader JE. Frequency response of cantilever beams immersed in viscous fluids with applications to the atomic force microscope. J Appl Phys. 1998;84(1):64–76.

82.   Burg T, Sader J, Manalis S. Nonmonotonic energy dissipation in microfluidic resonators. Phys Rev Lett. 2009 Jun;102(22):228103.

83.   Burg TP, Manalis SR. Suspended microchannel resonators for biomolecular detection. Appl Phys Lett. 2003;83:2698–700.

84.   Sadabadi H, Packirisamy M. Nano-integrated suspended polymeric microfluidics (SPMF) platform for ultra-sensitive bio-molecular recognition of bovine growth hormones. Sci Rep. 2017;7(1):10969.

85.   Von Muhlen MG, Brault ND, Knudsen SM, Jiang S, Manalis SR. Label-free biomarker sensing in undiluted serum with suspended microchannel resonators.

Anal Chem. 2010;82(5):1905–10.

86.   Burg TP, Godin M, Knudsen SM, Shen W, Carlson G, Foster JS, et al. Weighing of biomolecules, single cells and single nanoparticles in fluid. Nature. 2007;446(7139):1066–9.

87.   Manzoor Bukhari SA, Khan MF, Goswami A, McGee R, Thundat T. Thermomechanical analysis of picograms of polymers using a suspended microchannel cantilever. RSC Adv. 2017;7(14):8415–20.

88.   Miriyala N, Khan MF, Thundat T. Thermomechanical behavior of a bimaterial microchannel cantilever subjected to periodic IR radiation. Sensors Actuators, B Chem. 2016;235:273–9.

89.   Etayash H, Khan MF, Kaur K, Thundat T. Microfluidic cantilever detects bacteria and measures their susceptibility to antibiotics in small confined volumes. Nat Commun. 2016;7(12947):1–9.

90.   Khan MF, Schmid S, Davis ZJ, Dohn S, Boisen A. Fabrication of resonant micro cantilevers with integrated transparent fluidic channel. Microelectron Eng. 2011;88(8):2300–3.

91.   Barton RA, Ilic B, Verbridge SS, Cipriany BR, Parpia JM, Craighead HG. Fabrication of a nanomechanical mass sensor containing a nanofluidic channel. Nano Lett. 2010;10(6):2058–63.

92.   Westberg D, Paul O, Andersson G, Baltes H. A CMOS-compatible fluid density sensor. J Micromechanics Microengineering. 1997;7(3):253–5.

93.   Mcfarland AW, Poggi MA, Bottomley LA, Colton JS. Injection moulding of high aspect ratio micron-scale thickness polymeric microcantilevers. Nanotechnology.

2004;15:1628–32.

94. Kim WW, Gang MG, Min BK, Kim WB. Experimental and numerical investigations of cavity filling process in injection moulding for microcantilever structures. Int J Adv Manuf Technol. 2014;75(1–4):293–304.

95. McFarland AW, Colton JS. Chemical sensing with micromolded plastic microcantilevers. J Microelectromechanical Syst. 2005;14(6):1375–85.

96. Credi C, Fiorese A, Tironi M, Bernasconi R, Magagnin L, Levi M, et al. 3D printing of cantilever-type microstructures by stereolithography of ferromagnetic photopolymers. ACS Appl Mater Interfaces. 2016;8(39):26332–42.

97. Stassi S, Fantino E, Calmo R, Chiappone A, Gillono M, Scaiola D, et al. Polymeric 3D printed functional microcantilevers for biosensing applications. ACS Appl Mater Interfaces. 2017;9(22):19193–201.

Chapter 3:

Fabrication of microfluidic resonators

3.1. Introduction

The cost efficacy, small size, and high integration capability with electric circuits of has made MEMS attractive to many disciplines. Over the last few years, MEMS microfabrication has been subjected to extensive development. In fact, developed methods for microfabrication of conventional electronic devices play a major role in the functionality and reliability of MEMS. Some of the very common basic components in many MEMS devices are micro membranes and microcantilevers.(1,2)

Wet bulk microfabrication and surface microfabrication are two very common categories of microfabrication. Wet bulk microfabrication employs wet etchants to sculpt three dimensional features into the bulk of crystalline or noncrystalline materials with some common materials being silicon, quartz, SiC, Ge, and GaAs. On the other hand, in surface microfabrication, layer by layer deposition and patterning are the basic means of creating required features. Features made by bulk microfabrication are usually larger than those fabricated through surface microfabrication. An important benefit of surface microfabrication is that patterned features, in each layer, are not limited by crystallography of the substrate. In surface microfabrication, dry etching is employed to define the desired features in the x, y plane, while the role of wet etching is to release built-up structures. In this work, surface microfabrication was mostly employed to create

the required features, except for the last step of the fabrication where a combination of both methods was required to release the devices.

Selection of the proper materials for different layers of the device is critical in the final functionality of the fabricated device. Even though a plethora of substrates and thin films can be used for bulk and surface microfabrication, silicon based substrates are among the most favoured ones, especially for cantilever sensors.(3–6) In fact, several groups have used low-stress, low pressure chemical vapor deposited silicon nitride and polysilicon to fabricate resonators with embedded channels.(7–10)

Microcantilevers with embedded channels attracted research groups to analyze liquid samples. This is mainly because they maintain a high quality factor usually achievable only in vacuum. Therefore, they have been employed for performing measurements in many fields such as biology, engineering, physical chemistry, and more.(11–16) Depending on the final requirements of the device, different techniques can be employed to fabricate micro-resonators with embedded channels. Sacrificial layer methods are commonly used when it is required to minimize the mass of the resonator.(7–9) A sacrificial based method was used in this work for fabrication of microfluidic cantilevers with different sizes to investigate liquid samples as explained in chapters 4 and 6.

3.2.   Objective

The objectives in the fabrication of the microfluidic cantilevers are the following:

1) Employ single-sided polished Si-wafer as a substitute for double side polished Si-wafer. This helps reduce the cost of the fabrication process.

2) Increase the sensitivity of the previous iteration of this device by decreasing the thickness of the channel wall and decreasing channel heights. Two channel heights were fabricated to allow for handling molecules of different sizes if required.

3) Accomplish proper alignment accuracy for fabrication of feature sizes down to 2.5 μm for all five masks.

4) Release the devices with multiple dimensions and different designs on the same wafer. This helps reduce the cost of fabrication when multiple cantilever designs need to be investigated.

5) Accomplish backside alignment without damaging protruding patterns fabricated on the front side of the wafer.

3.3.   Design and chip layout

Microfluidic cantilevers were designed by Khan MF and not myself; however, the mask layout is included in Appendix A for future users who would like to follow this line of research. A part of the mask layout is shown in Figure 3.1. The hatched lines between the chips show the location of the through-wafer holes. These border holes will be etched into the wafer during the KOH etching process (the last step of the fabrication) while the cantilevers are released. These through-wafer holes were designed so that one can dice the wafer into individual chips at the end of the fabrication. The mask layout for a cantilever located on Chip 11 is shown in Figure 3.2. Variations in the dimensions and designs of the other microfluidic cantilevers are shown in Appendix A. Appendix A also

includes the mask layout of the double-clamped microfluidic resonator located on Chip 10.
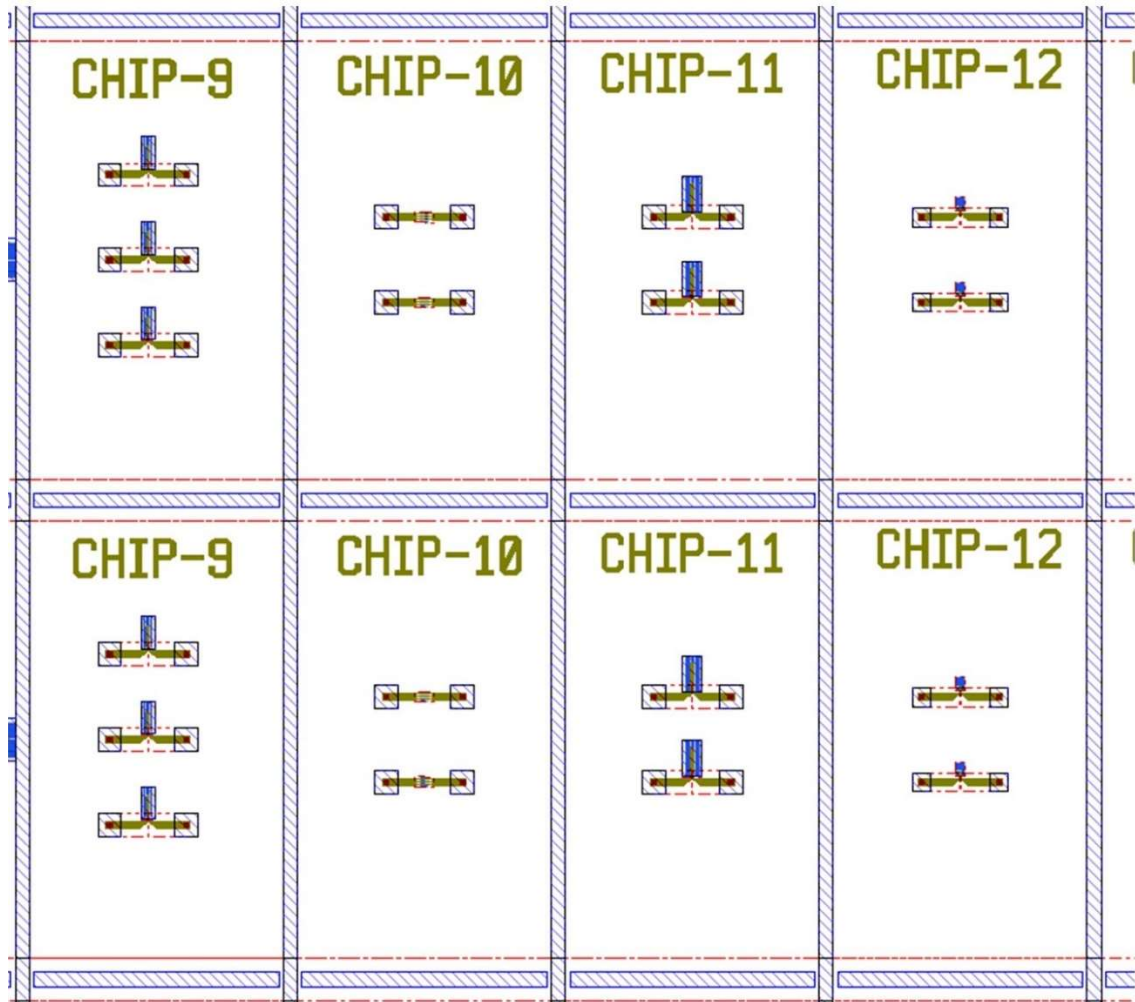
Figure 3.1. Mask layout and orientation of the chips. The size and design of the cantilevers vary from one chip to anther.
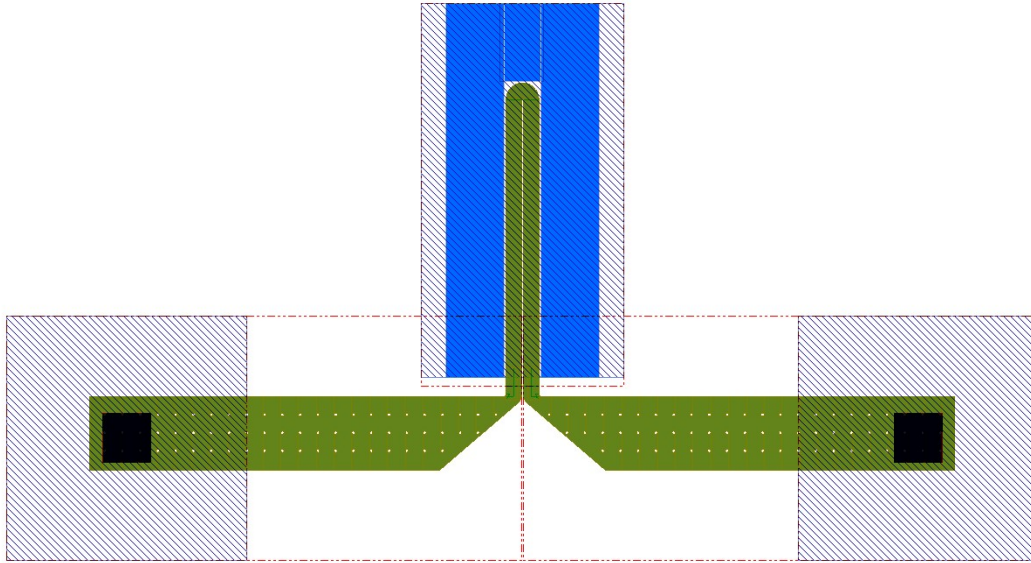
Figure 3.2. Mask layout for a cantilever located on Chip 11. Black squares show the locations of inlet and outlet. Green shows the microfluidic part. Blue shows the location of the through-wafer hole beneath the cantilever. The hatched area shows the location of the backside patterns. These patterns define the location of the through-wafer holes.

3.4.   Fabrication process steps

In this section, a detailed description of the steps developed for the fabrication of microfluidic cantilevers is described. This process employs five masks. The fabrication process is similar to that of other microfluidic cantilevers (8,10) where polysilicon is the sacrificial material and low-stress low-pressure chemical vapor deposited (LPCVD) silicon nitride is the structural material. Most techniques described in this section of the work are standard techniques in microfabrication processes. However, while working toward achieving objectives defined in section 3.2, several challenges were encountered. Some key issues for each process are discussed below.

3.4.1. Wafer preparation

Four-inch diameter silicon wafers with a thickness of 380 ± 25 µm and $\langle 100 \rangle$ orientation were purchased. The silicon wafers have a polished surface and lapped backside. Before any processing, the wafers were cleaned using a piranha etch solution (3:1 concentrated sulfuric acid, H_2SO_4, with hydrogen peroxide, H_2O_2) to remove organic and metallic contaminations. Wafer cleaning enhances adhesion of the next layer to the existing one. To prevent thermal shock, wafers were inserted in the piranha solution slowly.(6) The wafers remained in the solution for 15 minutes to complete the cleaning process.

3.4.2. Silicon process

The process flow for the fabrication of microfluidic channel cantilevers is illustrated in Figure 3.3. First, the wafers were coated with 500 nm low-stress LPCVD silicon nitride (Figure 3.3 (a)). The inlet and outlet were then etched to a depth of 500 nm using RIE in sulfur hexafluoride (Figure 3.3 (b)). A profilometer scan was used to monitor the depth of etching throughout the fabrication process whenever RIE was used to create a pattern. The aforementioned inlet and outlet provide access to the polysilicon layer that must be etched in the final step of the fabrication.
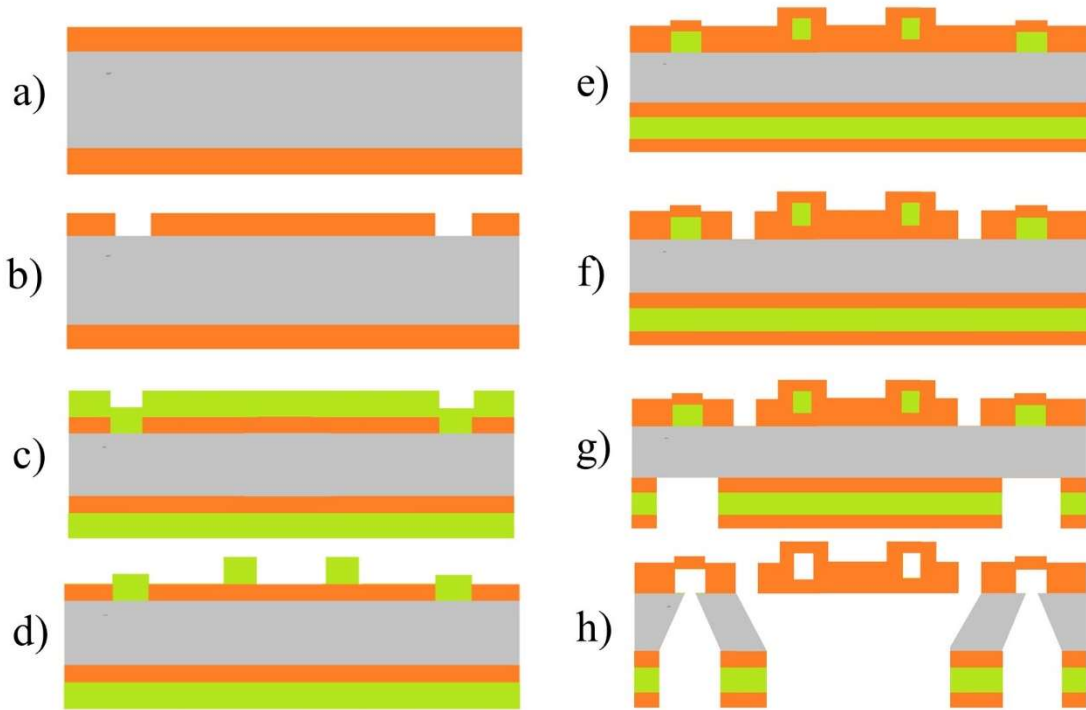
Figure 3.3. Fabrication process flow. Gray, orange, and green represent silicon, low stress silicon rich silicon nitride and polysilicon, respectively. This figure is not to scale.

Next, the LPCVD polysilicon layer was deposited with a thickness of 3 μm (Figure 3.3 (c)). Then, this layer was etched to a depth no less than 3 μm so that there was no polysilicon on the surface of the silicon nitride except where the microfluidic areas will later be created (Figure 3.3 (d)). An outline of the microfluidic channel created in this stage is shown in dark green in Figure 3.2.

After patterning the polysilicon layer, a second layer of low-stress LPCVD silicon nitride was deposited on the wafers to close the microfluidic channel (Figure 3.3 (e)). Next, both low-stress LPCVD silicon nitride layers were etched to a depth no less than 1000 nm to create an outline of the cantilever, located beneath the

microfluidic channel (Figure 3.3 (f)). The locations of through-wafer holes, for fluid injection, were then defined in the backside of the wafer. To align through-wafer holes with the inlet and outlet, patterned in the first step, a double side alignment technique was used. Simultaneously, the location of the second set of through-wafer holes for the purpose of accessing the backside of the cantilever was defined. These through-wafer holes must be aligned with the cantilever devices defined in the sixth step (Figure 3.3 (f)). Next, both low-stress LPCVD silicon nitride layers as well as the polysilicon layer were etched from the back side of the wafer using RIE (Figure 3.3 (g)).

The polysilicon layer, sandwiched between the structural nitride layers, was then dissolved in a six-molar aqueous solution of KOH at 85 ºC as the solution was stirred with a speed of 60 RPM. This etch took approximately 20 hrs. During the same etching process, the through-wafer holes were created as silicon was etched in the KOH solution (Figure 3.3 (h)). The wafers were monitored frequently during the etching process to ensure no overetching occurred. The frequency of inspection was increased specifically toward the end of the process. Figure 3.4 shows two examples of the microscopic images obtained during KOH etching to evaluate the extent of the etching. After the etching process was completed, the wafers were rinsed and dried. At the end, wafers were diced into individual chips where each chip contained two or three microfluidic cantilever devices. For example, a picture of one of the chip (Chip 11) is presented in Figure 3.5. In addition, microscopic images of cantilevers located on Chip 9 and Chip 14 are shown in Appendix A.
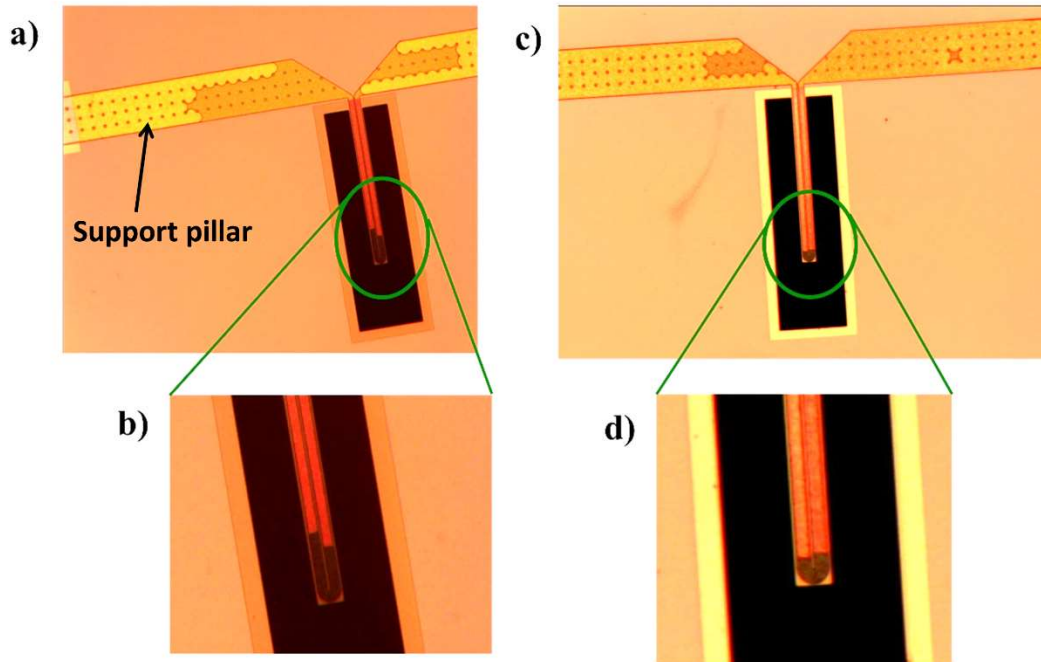
Figure 3.4. Microscopic images of the cantilever devices during the KOH etching. Images b) and d) show the tip portions of the cantilevers presented in images a) and c), respectively. The dark area at the tip of the device shows the remaining polysilicon that has not been etched yet.

Figure 3.5. A picture of Chip 11 after completion of the fabrication process. This chip contains two microfluidic cantilever devices.

The same process flow was followed to fabricate the microfluidic cantilevers with different wall thicknesses and channel heights. Table 3.1 shows all combinations of channel heights and wall thicknesses employed in fabrication of the microfluidic cantilevers in this work.

Table 3.1. Different design categories of microfluidic cantilevers

	Design Z1	Design Z2	Design Z3	Design Z4
Channel height	3 (μm)	1.5 (μm)	3 (μm)	1.5 (μm)
Wall thickness	500 (nm)	500 (nm)	250 (nm)	250 (nm)

Through-wafer holes created beneath the cantilever gave access to the backside of the device to deposit a secondary layer as required for the experiments presented in chapters 4 and 5. Only one array of cantilevers was designed without an access hole beneath the cantilever. This design was not developed for spectroscopy measurements; therefore, accessing the backside of the cantilever device was not required. Figure 3.6 shows microscopic images of this microfluidic cantilever device.
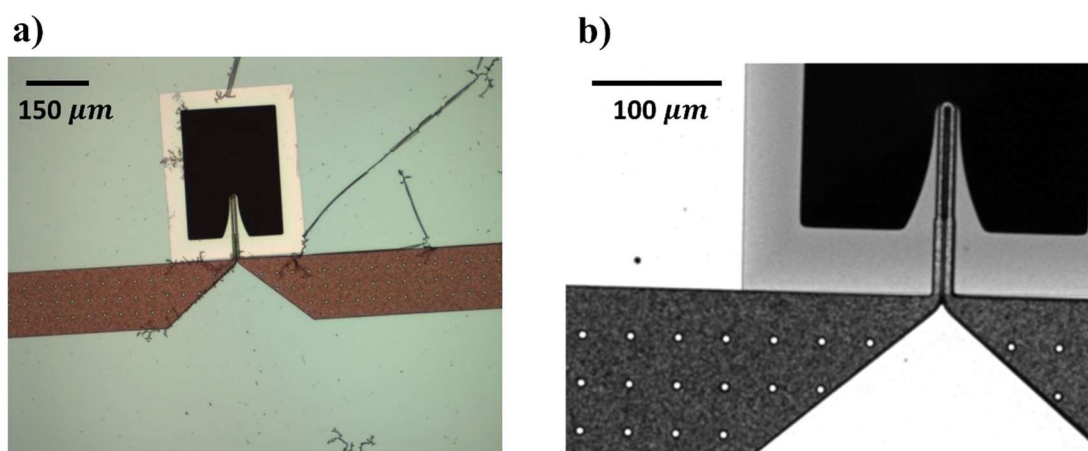
Figure 3.6. Microscopic images of the microfluidic cantilever where black in image a shows the etched pit beneath the cantilever. Black scale bars in images a and b are 150 and 100 μm, respectively.

3.5.   Device performance and characterization

Cantilever sensors are used as humidity sensors, metal ion sensors, calorimetric sensors, viscosity sensors, explosive detection devices, and more. All of these capabilities rely on operating the device in either static or dynamic mode. In the static mode of operation, deflection is the measured parameter. In the dynamic mode, frequency and quality factor are the measured parameters. Any extrinsic or intrinsic stress on the

cantilever results in a static deflection of the device, whereas the frequency of the cantilever alters due to the changes in the mass or in the viscoelastic properties.(17,18) Below, the performances of some of the fabricated microfluidic cantilevers are presented.

3.5.1. Frequency and quality factor

In the dynamic mode of operation, the sensing principle of a cantilever device is based on converting changes in mass into changes in resonance frequency. The changes in the resonance frequency of the cantilever are related to detected mass by the following equation:(19)

$$\Delta m = \frac{k}{4\pi^2}\left(\frac{1}{f_2^2} - \frac{1}{f_1^2}\right), \qquad\qquad (3.1)$$

where

k: Spring constant of the cantilever

f : Frequency of the vibration

Δm : Changes in the mass.

A fabricated microfluid cantilever with 600 μm length, 76 μm width, and 1.5 μm channel height was used to demonstrate the performance of the device upon filling the cantilever with a liquid sample. Resonance frequency of the microfluidic cantilever device in air was measured as the device was driven using a piezoelectric. As shown in Figure 3.7, the frequency of the device decreases upon filling the cantilever with ethanol. To obtain the quality factors and the center frequencies of the devices, the frequency responses of the devices were fitted by a Lorentzian function.
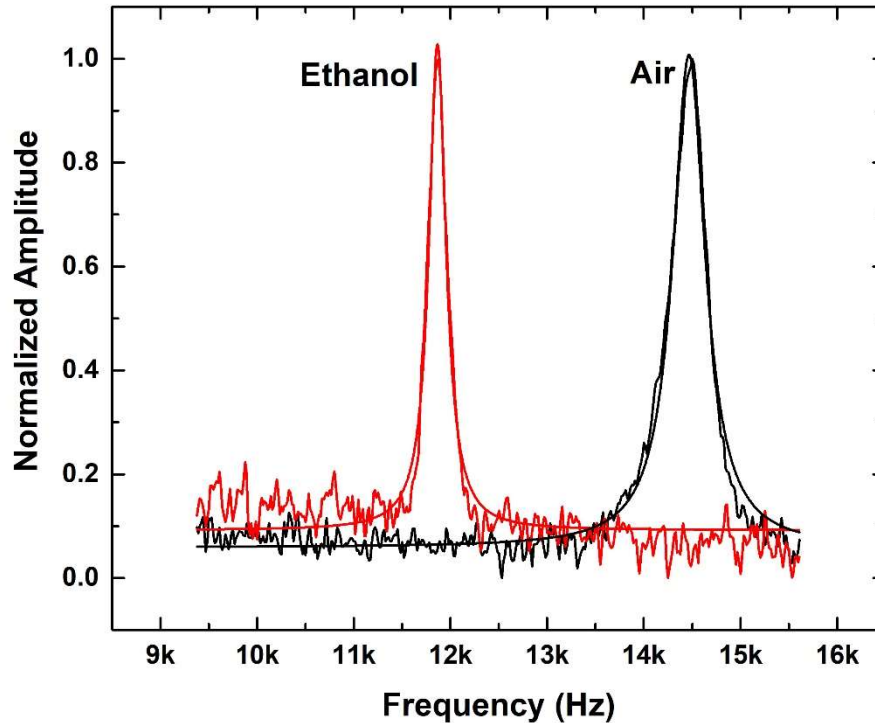
Figure 3.7. Changes in the resonance frequency of the cantilever device upon filling the device with ethanol. The quality factors and center frequencies are (from right to left): Q=35, 56, f_0=14.5, 11.9 kHz.

The natural frequency of a cantilever device can be related to its effective mass (m^*) and spring constant (k) by $\omega_0 = \sqrt{k/m^*}$. In general, a higher mass sensitivity is achieved by increasing the frequency of the device. Reducing the mass of the cantilever device increases the frequency. Figure 3.8 shows variations in the frequency of two kinds of fabricated cantilevers. Cantilever A is 100 µm long. This cantilever is similar to the cantilever shown in Figure 3.6. Cantilever B is 500 µm long and 44 µm wide. The channel height in both cantilever A and B is 3 µm. Quality factors and center frequencies of the cantilever A and B (reported in the caption of Figure 3.8) were obtained by fitting the

frequency response of the devices by a Lorentzian function. The quality factor of the device is inversely proportional to the damping constant and directly proportional to the resonance frequency of the system. If one operates the device in vacuum, the quality factor increases as a result of reducing the damping constant.
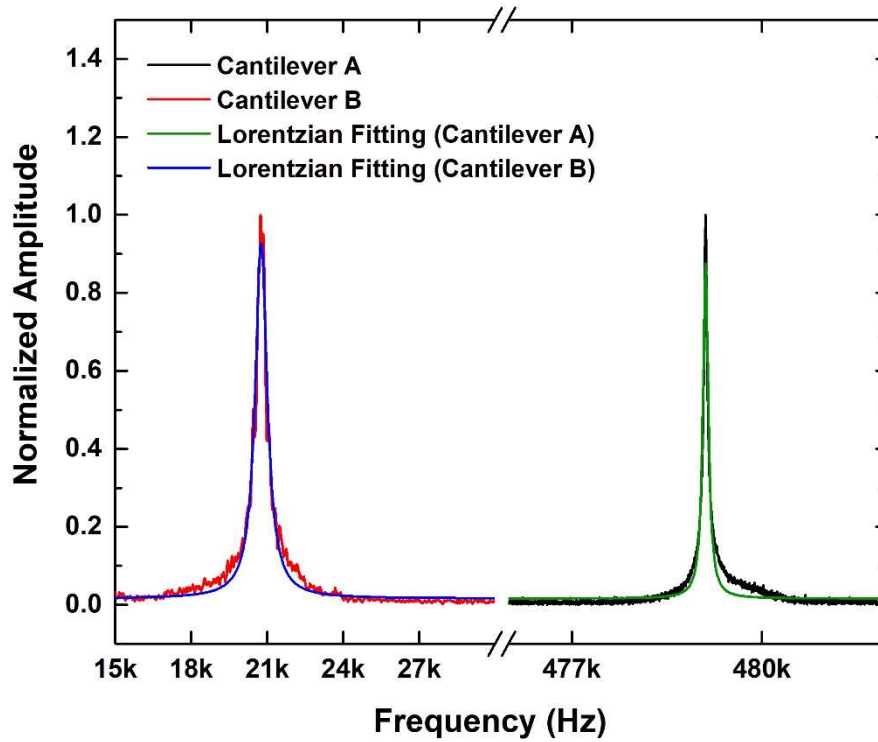
Figure 3.8. Variations in the natural frequency of two fabricated microfluidic cantilevers with different sizes. The quality factors and center frequencies are (from right to left): Q=4700, 36 and f_0=479.1, 20.8 kHz.

3.5.2. Static deflection of the device

Static deflection of a cantilever may have different origins, such as thermal, electrical, and magnetic.(17,20–22) Here, only the performance of the modified cantilever to the changes in temperature is presented, because the fabricated microcantilever was used as a photothermal cantilever deflection spectroscopy platform in this work. The modified cantilever has a 200 nm gold layer deposited on the backside of the device. Figure 3.9 shows the static deflection of the bi-material microfluidic cantilever due to the mismatch in the thermal expansion coefficients of the layers as the temperature of the device increases. The deflection of the cantilever as a function of temperature was measured as the device was heated using a hot plate. A thermocouple was used to monitor the temperature of the hot plate. Thermally induced bending of the cantilever was monitor with a similar set-up, as explained in Chapter 4.
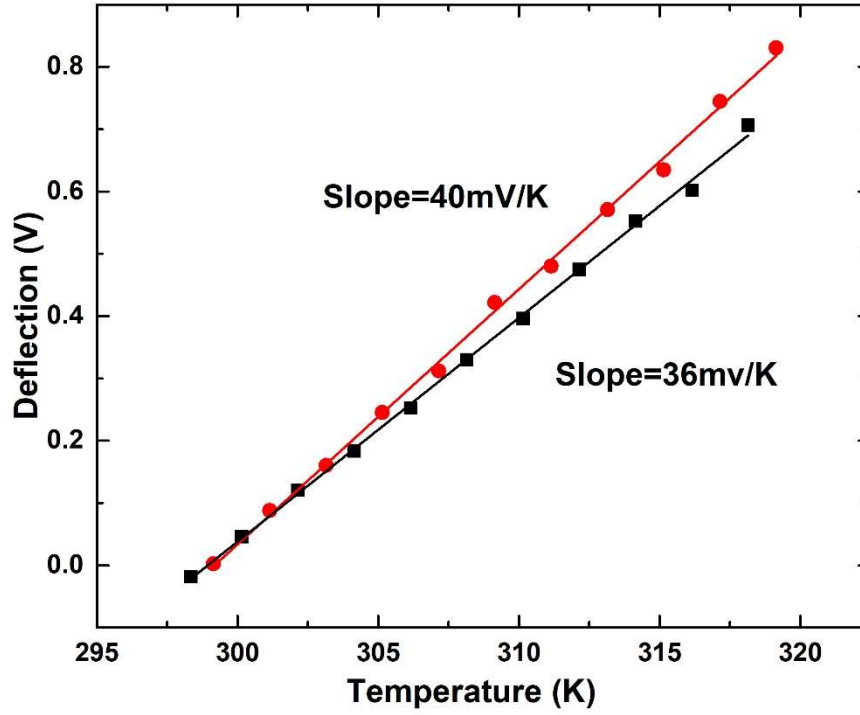
Figure 3.9. The static deflection of the bi-material microfluidic cantilever as a function of changes in the temperature. This cantilever is 600 μm long and 76 μm wide with the channel height of 1.5 μm. The red line and black line show the linear fittings for the experiments conducted on two different cantilever devices of the same size.

The relation between the deflection (Δz) of a rectangular cantilever beam, due to bi-metallic bending phenomena, and the material parameters is shown in the following equation:(20)

$$\Delta z = \frac{3\sigma(1-\upsilon)t_2}{E}\left(\frac{l}{t_1}\right)^2.$$

(3. 2)

In Equation 3.2, E, υ, t_1, t_2, l, and σ are Young's modulus, Poisson ratio, the substrate's thickness, a thickness of a deposited (thin) film, length of the device, and generated surface stress, respectively. The temperature induced surface stress (σ) is linearly proportional to the external variation of the temperature (ΔT). Thus, the deflection of the beam is linearly proportional to the changes in the temperature. This is consistent with the linear variation of the deflection of the bi-material microfluidic cantilever as a function of temperature shown in Figure 3.9.

3.6.   Material and methods

3.6.1.   Structural and sacrificial materials

Low stress silicon rich silicon nitride (SRN) was used as the main structural material for the fabrication of the microfluidic channel cantilevers for the following reasons:

1) Low residual stress of SRN allows the fabrication of the microfluidic channel cantilevers with minimal stress-induced curvatures.

2) LPCVD method result in high uniformity in the thickness and the composition of SRN.

3) SRN acts as an almost perfect etch mask for KOH. It was very important for the cantilever structure to remain intact during the long release process where KOH etching was used.

4) Silicon rich silicon nitride is optically transparent which is important for performing the experiments presented in Chapter 4.

To minimize the residual stress developed in the process of fabrication, the same material (i.e., SRN) was selected for the first and second structural layer.

Use of a sacrificial layer for the purpose of creating a thin microfluidic channel is an old technology.(23) In this work, polysilicon was used as a sacrificial layer. After depositing the polysilicon layers with different thicknesses, SEM images were obtained to validate the thicknesses of the deposited layers. Figure 3.10 and Figure 3.11 show the SEM images of the polysilicon layers, deposited on a silicon wafer, with a thickness of 1.5 and 3 μm, respectively.
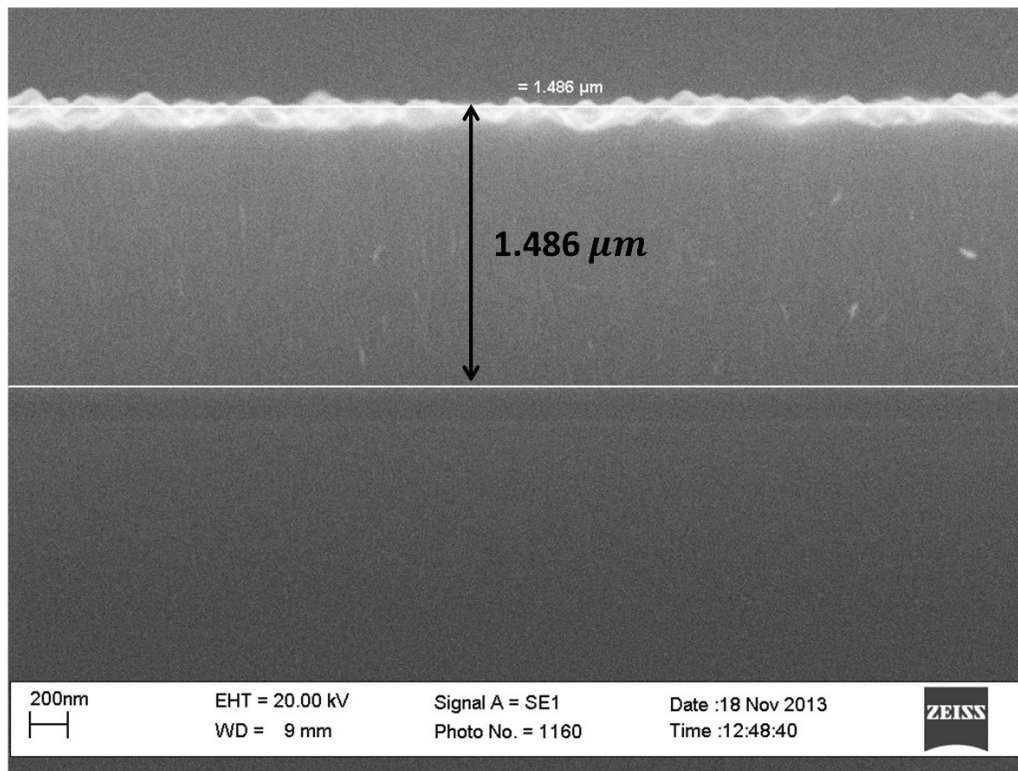
Figure 3.10. A SEM image of a 1.5 μm LPCVD deposited polysilicon layer.
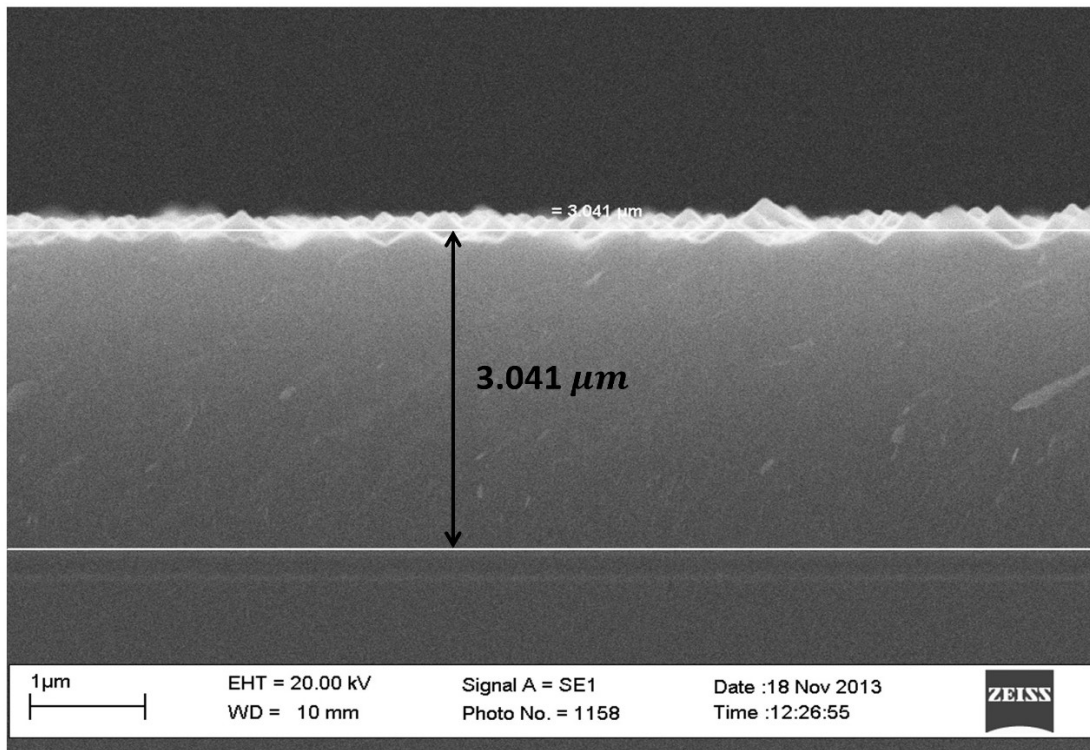
Figure 3.11. A SEM image of a 3 µm LPCVD deposited polysilicon layer.

For a successful fabrication, a very high selectivity of the etchant between a sacrificial material and a structural layer (silicon nitride) is one of the main requirements. Such a selectivity was achieved by employing potassium hydroxide (KOH) as the etchant.

3.6.2. Etchant chemical

The purpose of wet etching in this fabrication was twofold: first, to create a long microfluidic channel; and secondly, to release the cantilever device. Sacrificial polysilicon etching has been reported using both tetramethylammonium hydroxide (TMAH) and KOH as etchants.(24,25) KOH was used as the etchant, because its etch rate is much faster on the ⟨100⟩ plane than on the ⟨111⟩ plane and results in the formation of

etch pits. The etch pits are like an inverted four-sided pyramid. Such etch pits were formed under the inlet and the outlet of the microfluidic cantilever, from which fluid can be directed into the device using either negative pressure or a pumping technique. After placing the wafers in the KOH solution, wet etch begins with removing Si and eventually etching away the polysilicon sacrificial layer sandwiched between the silicon nitride layers (in this etching process silicon nitride acts as the mask material). Byproducts of the KOH wet etch are liquid or gas molecules that are soluble in the etchant solution. These were rinsed off after the etch process was completed.

3.6.3. Deposition method

To deposit low-stress silicon nitride and polysilicon LPCVD was used instead of atmospheric pressure chemical vapor deposition (APCVD) and PECVD due to the following reasons:

1) Even though APCVD has a high deposition rate and it is a simple chemical vapor deposition, it suffers from very poor step coverage, as well as particle contamination.

2) While LPCVD and PECVD are two different means of depositing silicon nitride and are capable of producing thin films with low stress, LPCVD can provide a higher film density with lower cost per device since multiple wafers can be processed simultaneously.

3) In addition, deposited films by LPCVD form on both the front side and back side of the wafer, which results in the development of an equal amount of stress on both sides. Therefore, the wafer remains flat.

Low-stress silicon nitride was deposited from a 10:2 ratio of dichlorosilane (as silicon containing gas) and ammonia at 835°C and 250 mTorr. This results in a deposition rate of 3.94 Å/min. During the process of deposition, byproducts are released in the form of volatile gases. The following equation shows the reaction which takes place during the deposition of the silicon nitride.

$$3SiCl_2H_2 + 4NH_3 \longrightarrow Si_3N_4 + 6HCl + 6H_2. \tag{3. 3}$$
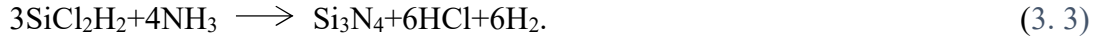
Polysilicon was deposited from SiH_4 (at 80 sccm) at 300 °C and 300 mTorr using LPCVD. The following equation shows the reaction which takes place during the deposition of the polysilicon.(25–27)

$$SiH_4 \longrightarrow Si + 2H_2. \tag{3. 4}$$

3.6.4.   Patterning and pattern transfer

In this work, photolithography technique was used to transfer patterns from the masks onto the thin films deposited on the substrates. Transfer of patterns by photolithography requires three basic steps.(3,28) First, the wafer was covered with an appropriate photoresist. Next, the wafer was exposed to UV, and finally, unexposed regions of the photoresist were removed (i.e., development).

Before covering the wafer with an appropriate photoresist, to enhance the adhesion between resist and the wafer, a very common adhesion promoter hexamethyldisilazane (HMDS) was coated on the wafer using a yield engineering systems (YES) vacuum chamber. The YES vacuum chamber makes it possible to do dehydration and priming in the same process chamber.(28,29) The initial dehydration secures a uniform and stable wafer priming.

HPR504 positive photoresist was employed in this work because it has better step coverage, a very good plasma etch resistance, and smaller feature sizes, 0.5 μm or less, compared to that of a negative photoresist. After priming the wafer, a uniform layer of HPR504 photoresist was coated on the wafer at 4000 RPM for 30 seconds as the wafer was held on a spinner chuck by means of vacuum. This resulted in a thickness of 1.25 μm. Spin coating of the HPR504 photoresist under the aforementioned conditions produced a sufficiently thick layer of the resist to transfer the pattern precisely to the substrate, and to not suffer from a high variation in the resist thickness.(6,30–34) Variation in the thickness of HPR504 photoresist as a function of spin speed is shown in Appendix B.

After the photoresist coating, the wafer was soft baked for 90 seconds at 115 ℃ on the hot plate to minimize the solvent concentration in the photoresist before proceeding to the exposure step. Compared to the conventional oven baking, hot plate soft backing reduces the chance of solvent trapping. Soft baking is helpful in improving the lithography process in several different ways. It improves the resist adhesion to the wafer while at the same time it decreases the chance of mask contamination or mask sticking to the photoresist. Also, soft backing prevents formation of N_2 bubbles during exposure and following thermal processes, such as etching. In addition, soft backing decreases the dark erosion during the resist development.

Because a certain amount of water in the resist is essential for a sufficient development, a subsequent rehydration for 15 min was performed to improve the exposure and developing of the photoresist.(4) Before the exposure, a mask was aligned with the previously defined patterns existing on the wafer. While the first set of patterns

was transferred to the wafer, a set of alignment marks was also transferred to the wafer. These high precision features, alignment marks, act as references when positioning the following patterns to the previous ones. Alignment marks have to allow not only alignment in x and y directions but also the theta alignment. As a result, one set of alignment marks was patterned on each side of the wafer. Also, it is important to be able to verify alignment marks after the wafer is processed during the deposition or resist coating. Therefore, alignment marks were included in the following patterns in case the original ones became eliminated as fabrication progresses. After securing a proper alignment, the wafer was exposed to UV light for 3 seconds.

HPR504 photoresist is a diazonaphthoquinone (DNQ) based resist. After the sensitizer DNQ was exposed to UV light, with the energy that corresponds to one of the DNQ absorption bands, it forms a ketene. In the next step, ketene reacts with the water absorbed in the Novolac resin during the dehydration step and produces carboxylic acid (see Figure 3.12).(6) 3-indenecarboxylic acid is an alkaline soluble and will be dissolved in the developing step.
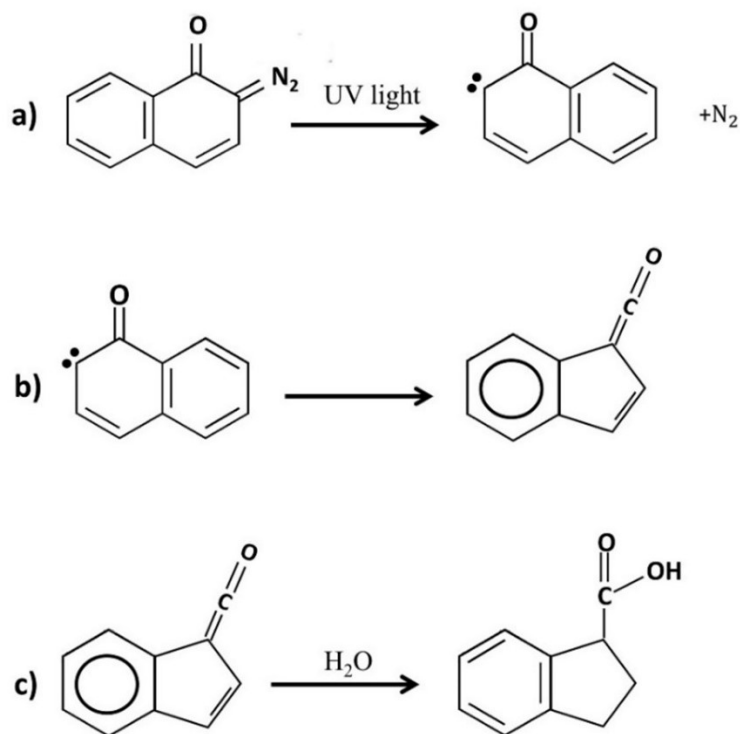
Figure 3.12. Photolysis mechanism for DNQ-based resist, a) insoluble sensitizer is exposed to UV light, which leads to photolysis, b) consequent rearrangement to form a ketene, and c) reaction of ketene with water and formation of base-soluble indene-carboxylic acid.

In the next step, the patterns were developed for 23 seconds in the alkali developer. The short development time reduces the chance of pattern distortion or swelling, as well as undesirable reduction in the resist thickness in the protected areas. Subsequently, the wafer was thoroughly rinsed and dried to stop further reactions between the photoresist and the developer after development was accomplished. In this stage, the wafer was inspected to confirm a proper alignment. Figure 3.13 shows an example of an unacceptable alignment for the fabrication of the microfluidic cantilever. In this case, an approximately 3 μm misalignment resulted in an inappropriate positioning of the outline

of the microfluidic channel as presented in Figure 3.13(b). Whenever the same or similar misalignment occurred as a result of the patterning process, the photoresist was completely washed off and the patterning procedure was repeated for the same mask.
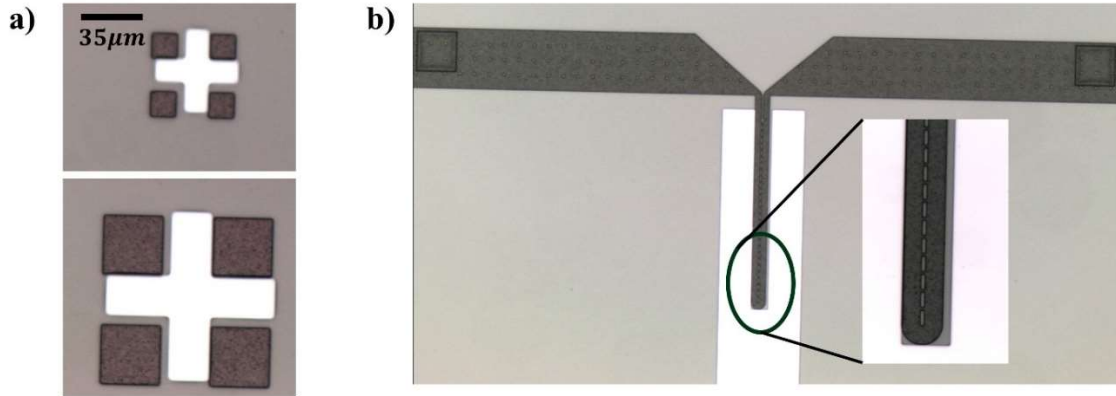
Figure 3.13. Microscopic images confirm misalignment of the mask and the wafer. These images were captured after patterning the outline of the cantilever regions on the second silicon nitride layer. a) alignment marks, b) a misaligned cantilever device relative to the microfluidic channel.

After a proper alignment was achieved, the patterns were etched into the previous layer by RIE. A profilometer scan was then used to measure the depth of etching. If the desirable depth of etching was not achieved, RIE was repeated for additional time. After achieving a proper depth of etching, a Branson Barrel etcher was used to remove the photoresist. Figure 3.14 shows an example of the profilometer scan obtained after the outline of the cantilevers were etched into the silicon nitride layers for the devices with wall thicknesses of 500 nm and the channel heights of 1.5 µm. This measurement shows that an etching depth of 1089 nm was obtained after RIE was completed. Profilometer measurements were conducted at five different locations for each wafer.
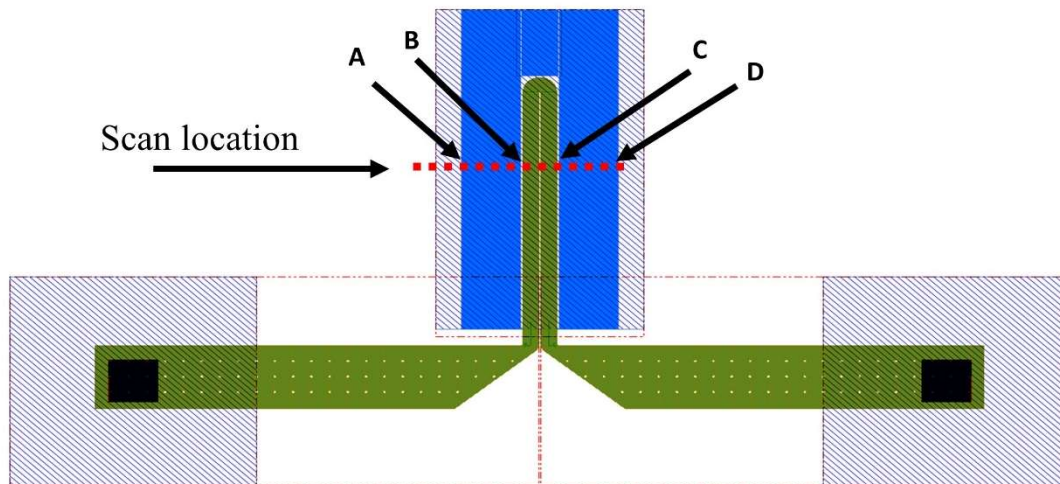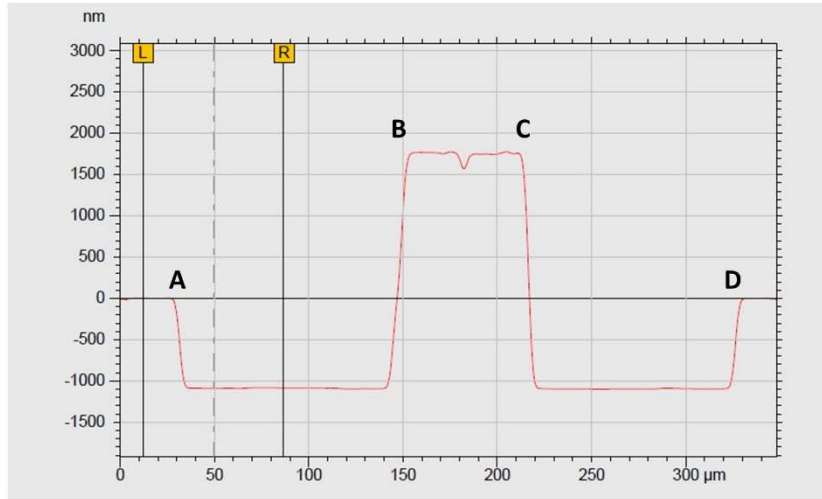
Figure 3.14. A profilometer scan of a cantilever device with the wall thickness of 500 nm and the channel height of 1.5 μm. Etched height was measured as 1089 nm. Approximate location of the scan is represented with the red dotted line on the schematic of the cantilever.

3.6.5. Double side patterning

Double side alignment technique was used in this work to define the locations of through-wafer holes in the backside of the wafer. To achieve alignment of patterns on

the opposite sides of the substrate, a set of gold alignment marks was created on the front side of the wafer.

Sputtering and liftoff were employed to create desired gold marks on the wafer. For a successful liftoff process, first a layer of HPR506 photoresist was coated on the wafer at 4000 RPM for 40 seconds. This resulted in a thickness of 1.75 μm. This thickness was small enough to allow solvent to seep underneath the photoresist during the liftoff process. The coated photoresist was then patterned. The resist's patterns must be a mirror of the desired gold patterns. Later, a 10 nm Cr layer and 50 nm gold layer were deposited on the wafer, using the sputtering System #3 (Floyd) in University of Alberta nanoFAB. Next, the wafer was immersed in an acetone bath for approximately 40 min, while sonicating the solution, to remove the gold layer deposited on the photoresist.

In this stage, the wafer must be placed in the mask aligner in the facedown position. Therefore, it is required to protect the features created on the front side of the wafer. To do so, a thick layer of AZ P4620 photoresist was spin coated on the front side of the wafer. Next, a HPR504 photoresist was coated on the back side of the wafer at 4000 RPM for 30 seconds. Then, we used IR light to see through the wafer and line up the paterns on the front and back side of the wafer. Use of a single-sided polished wafer reduced the accuracy of the alignement due to increased scattering of the IR light from the unpolished backside of the wafer.

3.7.   Conclusions and future work

Microcantilever sensors have been reported as a very sensitive sensing platform, especially when they are operated in vacuum or air. This platform has been used for spectroscopy techniques by measuring released heat as molecules are promoted to the excited level. However, to perform liquid spectroscopy using a cantilever sensor with high sensitivity, it is required to confine the liquid in the sensor. In this work, employing surface microfabrication on 350 μm thick silicon wafers, successful fabrication of the microfluidic cantilever devices with quite a few different lengths and widths was achieved. The devices have either a wall thickness of 500 or 250 nm and a channel height of either 1.5 or 3 μm. Depending on the dimension of the device, confining one picolitre to hundreds of picolitre (300 pL) of a liquid sample inside the device is achievable. Performance of the fabricated devices are demonstrated in Chapter 4, Chapter 5, and Chapter 6 as the device was operated in either the static or dynamic mode.

The following bullet points highlight the catastrophic flaws one needs to avoid if employing the fabrication process presented in this work:

- Use of single-sided polished wafer, because it reduces the accuracy of the double side alignment process and it lowers the yield.

- Designing the mask so that the layouts of some devices are located on the edges of the wafer. During the process of fabrication, one must use tweezers to handle the wafer. Therefore, devices located on the edge of the wafer are prone to damage due to the applied pressure from the tweezers.

- Designing the microfluidic cantilever with different volumes of the channel in one mask. This increases the under-cut of the cantilevers as some devices need to be etched for a longer period of time while the others are completely released.

- Designing the location of the inlet and outlet asymmetrically in relation to the main microfluidic channel.

- Designing continuous through-wafer holes between the chips. This results in breaking the wafer into individual chips during the long KOH etching. As the devices need to be inspected several times during the KOH etching, it is important to secure the integritiy of the wafer until all the devices are released.

In additon, in the current design the cantilevers are protruded from the surface of the wafer. Therefore, they are more vulnerable to damage during the alignment processes (especially the backside alignment). Hence, it is ideal to change the design so that the cantilever devices are embedded in the silicon wafer. Further, it is desirable to reduce the undercut by modifying the etching process.

3.8. References

1. Lee S-JJ, Sundararajan N. Microfabrication for microfluidics. Boston: Artech House; 2010.

2. Chakraborty S. Microfluidics and microfabrication. New York: Springer; 2010.

3. Huang Y, Vasan ASS, Doraiswami R, Osterman M, Pecht M. MEMS reliability review. IEEE transitions device Mater Reliab. 2012;12(2):482–92.

4. Mitra SK, Chakraborty S. Microfluidics and nanofluidics handbook: fabrication, implementation and applications. Boca Raton, FL: CRC press; 2012.

5. Madou MJ. Fundamental of microfabrication and nanotechnology, 3rd ed. Vol. 3. Boca Raton, FL: CRC press; 2012.

6. Madou JC. Fundamentals of mirofabrication: the science of miniaturization, 2 nd ed. Boca Raton, FL: CRC press; 2001.

7. Burg TP, Manalis SR. Suspended microchannel resonators for biomolecular detection. Appl Phys Lett. 2003;83:2698–700.

8. Khan MF, Schmid S, Davis ZJ, Dohn S, Boisen A. Fabrication of resonant micro cantilevers with integrated transparent fluidic channel. Microelectron Eng. 2011;88(8):2300–3.

9. Barton RA, Ilic B, Verbridge SS, Cipriany BR, Parpia JM, Craighead HG. Fabrication of a nanomechanical mass sensor containing a nanofluidic channel. Nano Lett. 2010;10(6):2058–63.

10. Burg TP, Mirza AR, Milovic N, Tsau CH, Popescu G a., Foster JS, et al. Vacuum-packaged suspended microchannel resonant mass sensor for biomolecular detection. J Microelectromechanical Syst. 2006 Dec;15(6):1466–76.

11.   Sadabadi H, Packirisamy M. Nano-integrated suspended polymeric microfluidics (SPMF) platform for ultra-sensitive bio-molecular recognition of bovine growth hormones. Sci Rep. 2017;7(1):10969.

12.   Von Muhlen MG, Brault ND, Knudsen SM, Jiang S, Manalis SR. Label-free biomarker sensing in undiluted serum with suspended microchannel resonators. Anal Chem. 2010;82(5):1905–10.

13.   Burg TP, Godin M, Knudsen SM, Shen W, Carlson G, Foster JS, et al. Weighing of biomolecules, single cells and single nanoparticles in fluid. Nature. 2007;446(7139):1066–9.

14.   Manzoor Bukhari SA, Khan MF, Goswami A, McGee R, Thundat T. Thermomechanical analysis of picograms of polymers using a suspended microchannel cantilever. RSC Adv. 2017;7(14):8415–20.

15.   Miriyala N, Khan MF, Thundat T. Thermomechanical behavior of a bimaterial microchannel cantilever subjected to periodic IR radiation. Sensors Actuators, B Chem. 2016;235:273–9.

16.   Etayash H, Khan MF, Kaur K, Thundat T. Microfluidic cantilever detects bacteria and measures their susceptibility to antibiotics in small confined volumes. Nat Commun. 2016;7(12947):1–9.

17.   Boisen A, Dohn S, Keller SS, Schmid S, Tenje M. Cantilever-like micromechanical sensors. Reports Prog Phys. 2011;74(3):36101.

18.   Lavrik N V., Sepaniak MJ, Datskos PG. Cantilever transducers as a platform for chemical and biological sensors. Rev Sci Instrum. 2004;75(7):2229–53.

19.   Thundat T, Warmack RJ, Chen GY, Allison DP. Thermal and ambient-induced

deflections of scanning force microscope cantilevers. Appl Phys Lett. 1994;64(21):2894–6.

20.   Toda M, Inomata N, Ono T, Voiculescu I. Cantilever beam temperature sensors for biological applications. IEEJ Trans Electr Electron Eng. 2017;12(2):153–60.

21.   Raiteri R, Grattarola M, Butt H, Skladal P. Micromechanical cantilever-based biosensors. Sensors Actuators B Chem. 2001;79:115–26.

22.   Bridle H, Wang W, Gavriilidou D, Amalou F, Hand DP, Shu W. Static mode microfluidic cantilevers for detection of waterborne pathogens. Sensors Actuators, A Phys. 2016;247:144–9.

23.   Sugiyama S, Suzuki T, Kawahata K, Shimaoka K, Takigawa M, Igarashi I. Micro-diaphragm pressure sensor. In: International Electron Devices Meeting. Los Angeles; 1986. p. 184–7.

24.   Berenschot JW, Tas NR, Lammerink TSJ, Elwenspoek M, Van Den Berg A. Advanced sacrificial poly-Si technology for fluidic systems. J Micromechanics Microengineering. 2002;12(5):621–4.

25.   Stern MB, Geis MW, Curtin JE. Nanochannel fabrication for chemical sensors. J Vac Sci Technol B Microelectron Nanom Struct. 1997;15(6):2887.

26.   Chu W-H, Ferrari M. Silicon nanofilter with absolute pore size and high mechanical strength. In: Proceeding of the society of photo-optical instrumentation engineers(SPIE). 1995. p. 9–20.

27.   Sivaram S. Chemical vapor deposition thermal and plasma deposition of electronic materials.New York: Van Nostrand Reinhold; 1995.

28.   Levinson HJ. Principles of lithography, third edition. Bellingham, Wash: SPIE

Press; 2010.

29. Xiao H. Introduction to semiconductor manufacturing technology, second edition. Bellingham, Wash: SPIE Press; 2012.

30. Tan ZCH, Le P, Lem H. Evaluation of DNQ/novolac resist for 130 nm device maskmaking. Microelectron Eng. 1998;41:315–8.

31. Suzuki K, Smith BW. Microlithography science and technology, second edition. Boca Raton: CRC press Taylor & Francis Group; 2007.

32. Tan ZCH, Le P, Coleman T. Potential of DNQ/novolac and chemically amplified resist for 100 nm device generation maskmaking. Microelectron Eng. 2001;57:431–538.

33. Bruenger WH, Buchmann LM, Torkler M, Sinkwitz S. HPR 506 photoresist used as a positive tone ion resist. J Vac Sci Technol B. 1996;14(6):3924–7.

34. Scheckler EW, Ogawa T, Yamanashi H, Soga T, Ito M. Resist pattern fluctuation limits in extreme-ultraviolet lithography. J Vac Sci Technol B. 1994;12(4):2361–71.

Chapter 4:

Photothermal microfluidic cantilever deflection spectroscopy of ethanol-water mixtures

4.1.   Introduction

Infrared spectroscopy is a fast, non-destructive technique, broadly employed in different disciplines due to the fact that most molecules on Earth absorb IR radiation.(1,2) Infrared spectroscopy is not only used to identify functional groups in mixtures but also to study the structure of compounds.(3–6) Although IR spectroscopy is widely used in the study of solid samples due to its high sensitivity, it has remained a challenge to use this method with liquid samples. Because water has strong absorptions in the MIR region this makes the application of IR spectroscopy in aqueous solutions very difficult. Also, due to the low-resolution spectrum of liquid samples, information content of the spectrum is reduced.(7) Thus, IR spectroscopy does not offer a suitable platform to acquire detailed information about intermolecular interactions in aqueous solutions.

In 1993, Gimzewski JK et al. used a modified cantilever device to measure the heat of a reaction.(8) Noting the device's high sensitivity to heat, the same group used a modified cantilever platform for spectroscopic study and achieved sensitivity down to 100 pW.(9) However, spectroscopy of a liquid sample with a standard bi-material microcantilever is challenging because the device must be submerged in the liquid. Operation of the device in liquid media decreases the sensitivity significantly. The studies

described in this chapter use a microfluidic cantilever, capable of holding picoliters of liquid sample, for the purpose of liquid spectroscopy.

4.1.1. Aqueous mixtures of ethanol

Aqueous mixtures of alcohol are complex systems with complicated intermolecular interactions that have been investigated in many different fields, including microbiology, physics, chemistry, biotechnology, and engineering. Improved understanding about alcohol-water interactions and their structural properties has helped various scientific communities to use aqueous mixtures of alcohol to their benefit.(10–15)

In the field of biology, two studies related to alcohol-water include a study on the effect of ethanol on DNA relaxation and the structure of proteins;(10) and the importance of hydrophobic and hydrophilic interactions of alcohol-water mixtures for proteins stabilization. It is well reported that proteins are denatured in organic solutions such as ethanol; however, they can fold into their native state when in water.(11,12) It is also reported that when proteins unfold, the exposure of hydrophobic groups makes a significant difference in the heat capacity of denatured, as well as stabilized native, proteins. The aforementioned information highlights the importance of studying protein behaviours in alcohol-water mixtures. These kinds of behaviours could be related to the presence of non-polar groups in alcohol or the formation of specific molecular structure of water and alcohol in the mixture.(11)

In the pharmaceutical field, the effect of ethanol-water's complex interactions on the permeability of drugs in hydrophobic polymers, as a result of the polymers' swelling, has been examined. Polymer membranes are very common in drug-controlled-release devices. Ethanol-water mixtures serve the crucial role of dissolving the drug; however,

they can also cause swelling of the membrane and, therefore, change the rate of drug release. Another study examined the solubility of poly(ethylene-co-vinyl alcohol) in ethanol-water, where poly(ethylene-co-vinyl alcohol) is not soluble in pure water or pure ethanol.(13) Hoogenboom R et al. reported tunable solubility of copolymers based on 2 - phenyl - 2 - oxazoline and 2 - methyl - 2 - oxazoline in the mixture of ethanol-water. Since alcohol and water have very low toxicity, such impressive properties can be employed in drug delivery applications by changing the solubility of the drug in the alcohol-water mixtures.(15) These effects might be attributable to the formation of hydrogen bonds between the ethanol-water complex and surrounding molecules.(13)

The amphiphilic nature of ethanol gives amazing power to this short-chain alcohol. Since ethanol is soluble in water, as well as in fat, it is able to cross the cell membrane. It helps maintain the structure of water around hydrophobic molecules such as methane.(14) Ethanol's effects on the stability of amino acids as well as a sudden volume change of poly(2-methacryloyloxyethyl phosphorylcholine(MPC)) in the water-ethanol mixture are among some interesting studies involving aqueous ethanol solution.(12,16) These are just a few examples of the importance of ethanol solutions. This highlights the necessity of greater understanding of interactions between ethanol and water. Over the last decades, several studies have examined the structural features of ethanol-water solutions. However, there remains an ongoing debate on the effect of the intermolecular interactions in the properties of ethanol-water mixtures. (12,17–26)

4.1.2. Techniques to study mixtures of alcohol-water

Over the past few decades, many different experimental and computational methods have been beneficial in providing enhanced insight about the structure of alcohol-water

74

mixtures. Examples include dielectric relaxation spectroscopy,(27) ultrasonic absorption spectroscopy,(28,29) shear impedance spectrometry,(30) light-Scattering,(31) nuclear magnetic resonance (NMR),(32,33) FTIR and IR spectroscopy,(33) mass spectroscopy and X-ray diffraction,(34) Ultraviolet–visible (UV-Vis) and fluorescence spectroscopy,(35) and Raman spectroscopy.(23) In addition, molecular dynamics simulations have been widely used to shed light on understanding alcohol-water mixtures.(36–43)

Infrared spectroscopy is one of the commonly employed vibrational spectroscopy methods to investigate alcohol-water mixtures, including ethanol-water mixtures. This method works based on the interactions between molecules and the electric field vector of light. Infrared spectroscopy is a fast, sensitive, and information-rich technique where position, intensity, width, and shape of the peaks carry useful information about the analyte. Despite the many advantages of IR spectroscopy, it is not an ideal technique for aqueous solutions, especially if water is part of the solution.(1,7)

In this work, the capability of the microfluidic channel cantilever platform to study ethanol-water mixtures by collecting IR spectra was investigated.

4.1.3.   Photothermal spectroscopy

Photothermal phenomena have been employed for decades to improve the performance of cantilever sensors in both dynamic and static mode of operation. The principle behind both photothermal excitation and photothermal bending of cantilevers are the same: a cantilever is a platform to transfer optical energy to mechanical energy. Photothermal bending of cantilevers has been employed in this work because it is more sensitive and theoretically well established.(9,44)

For the first time, in 1993, Gimzewski JK et al. combined the idea of heat-induced bending of a strip composed of bi-material with photothermal phenomena using a cantilever platform for chemical sensing. This innovative idea resulted in a platform for molecular spectroscopy with 100 pW power sensitivity. When light was shined on the cantilever, some of the absorbed photons transferred to heat. The generated heat caused the cantilever to bend because of differences in the thermal expansion of the comprising layers.(8,9)

Even though this system has high sensitivity when performing in air or vacuum, its operation in liquid media decreases the sensitivity significantly, for several reasons. Attenuation of light through liquid media, before reaching the cantilever, reduces the input energy and, therefore, lowers the bending of the cantilever. In addition, the liquid media surrounding the cantilever dissipates the generated heat faster than air, which also reduces the bending of the device. Furthermore, optical read out and alignments can be difficult when the device is submerged in liquid. Finally, functionalization of the cantilever surface might be required to increase the population of analytes on the surface of the cantilever. Thus, operation of a cantilever in a liquid media not only reduces the sensitivity, but also complicates the experimental set-up.

Significant increases in sensitivity can be achieved by confining the liquid inside the cantilever. The idea of confining liquid inside the cantilever was presented for the first time by MIT researcher Scott Manalis to reduce viscous drag when a cantilever is operating in the dynamic mode.(45)

The fabricated microchannel resonator, by the MIT group, thoroughly changed the approach toward liquid based detection using cantilever sensors. However, the fabrication

of the device is complicated and thus expensive. In addition, since the exterior of the microchannel resonator is vacuum sealed using a capping wafer, for the purpose of a higher sensitivity, the user does not have access to the device structure.(46) Therefore, deposition of a second layer , required for photothermal spectroscopy, on the cantilever is not possible unless it is added during the fabrication process. Adding a second layer of material to the cantilever structure, during the fabrication, makes the fabrication more complicated.

In this research, microfluidic cantilevers are fabricated so that any required secondary layers can be deposited as needed during the course of experimentation. Also, the fabrication process of the microfluidic cantilevers presented in this work is less complicated mainly because the device is not vacuum packed. The microfluidic cantilever provides us with an excellent platform to study liquid analytes and light interaction with the samples.

4.2. Objective

The objectives in the study in this chapter are the following:

1) Confining picoliters of ethanol-water binary mixtures in microfluidic cantilever sensors;

2) Collecting IR spectrum of the confined liquid samples using the photothermal cantilever deflection technique;

3) Investigating the effect of concentration of ethanol, in peak positions of C-C-O asymmetric stretch in the collected spectrums; and

4) Investigating the effect of concentration of ethanol in peak heights of C-C-O asymmetric stretch at a fixed wavenumber.

4.3. Experimental design

4.3.1. Microfluidic cantilever device

Figure 4.1 shows scanning helium ion microscope (HIM) images of a device employed for exploring ethanol-water interactions using a photothermal cantilever deflection spectroscopy (PCDS) setup. The cantilever located underneath of the microfluidic channel has a thickness of 0.5 μm, a width of 74 μm, and a length of 600 μm. Dimensions of the microfluidic channel are presented in Figure 4.1.
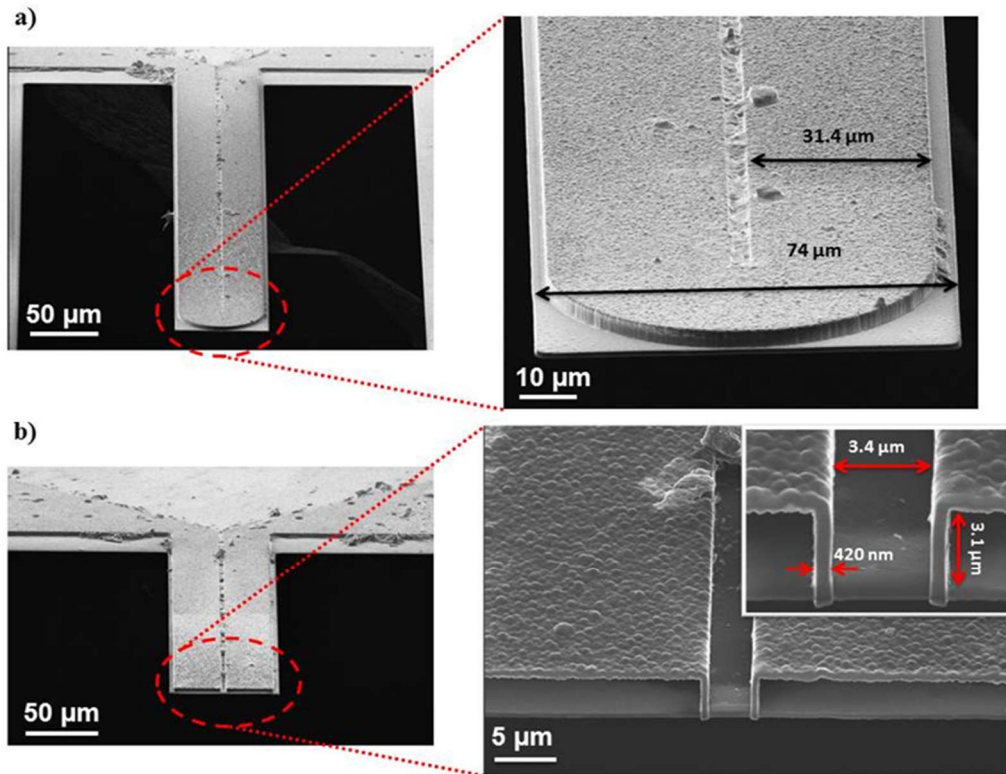
Figure 4.1. HIM image of a microfluidic cantilever: a) top view of the microfluidic cantilever, and b) top view of a cut microfluidic cantilever and a cross section of the channel constructed on top of the cantilever.

4.3.2. Fluid delivery

Fluid transfer to the cantilever is achieved from the backside of the chip via anisotropically etched through-holes. Each chip contains two or three microfluidic cantilever devices, as explained in Chapter 3. The fluidic connections should be leak tight and compatible with the chemicals used for cleaning.

Figure 4.2 illustrates the package design for transferring the fluid, as well as holding the chip in position for signal read out. The assembly consists of Teflon tubes, stainless steel tubes, a PDMS layer, a polyether ether ketone (PEEK) holder, and aluminum clamps. The assembly is clamped onto an optical table along with read out setup and the IR source.

Teflon tubes, carrying liquid, were connected to the PEEK holder by stainless steel tubes inserted in the PEEK. The connection of Teflon tube to the stainless steel tube, as well as the connection of the stainless tube to PEEK, is a friction fit connection. The holes in the PEEK holder were drilled with two different diameters at each end to seal the stainless steel tubing at the back and to minimize leaking on the top. A leak-tight seal was achieved between the holes in the PEEK block and the stainless steel tubing, which are connected to the exchangeable Teflon tubes. The PDMS piece was located between the chip and the PEEK for sealing purposes (fabrication of the PDMS layer is explained in section 4.5.2 of this chapter). An aluminum holder was screwed on top of the chip to clamp all the layers down, to ensure proper alignment and sealing between the chip, the PDMS, and the PEEK.

The assembly shown in the Figure 4.2 was custom made based on the dimensions and specifications of the chips and the microfluidic cantilevers employed for this chapter of the work. Any changes in future fabricated devices, following this thesis, will require a new design for a proper fluid transfer.
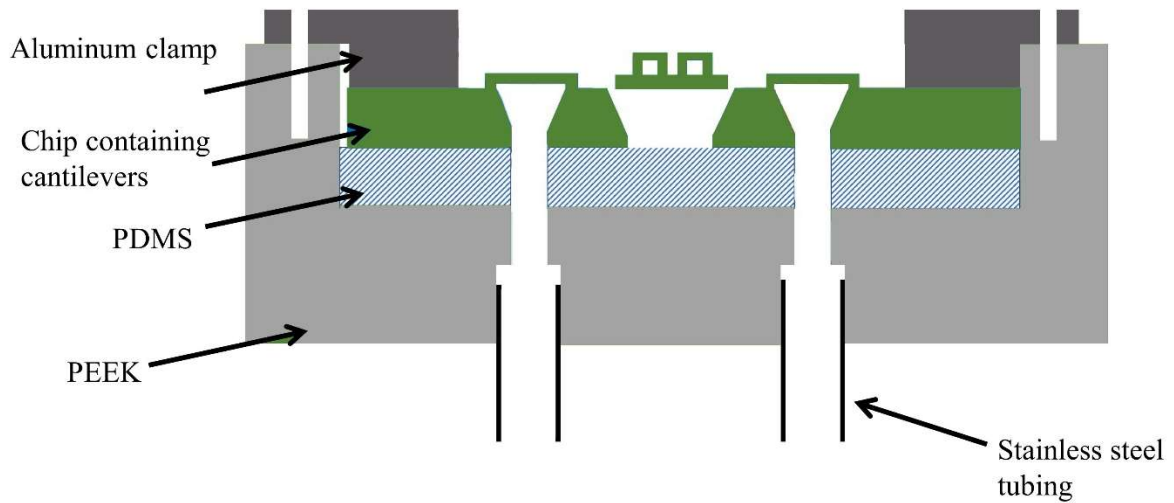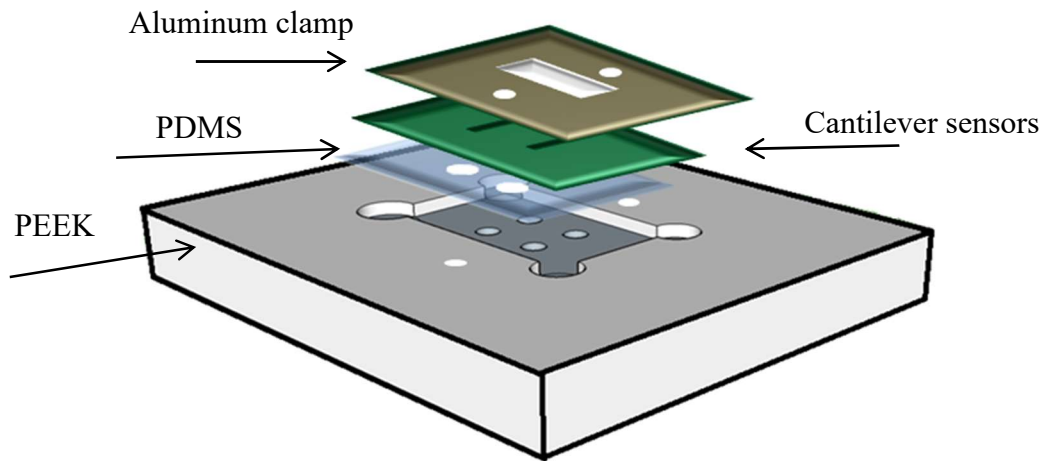
Figure 4.2. Schematic of package design for fluid transfer, profile (top) and side view (bottom).

4.3.3. Measurement set-up

Thermally induced bending of the microfluidic cantilever was recorded by tracking the position of a laser beam reflected off of the cantilever onto a position sensitive diode (PSD) whose output voltage is proportional to the cantilever bending. The output signal

from the PSD was fed to a lock-in amplifier (SRS 850 Stanford Systems) and spectrum analyser (SRS 760 Stanford Systems) to monitor the amplitude of bending and frequency of vibration of the cantilever as various concentrations of ethanol-water mixtures were loaded into the channel. The photothermal spectrum of each mixture was obtained by illuminating the cantilever with monochromatic infrared radiation using a QCL (Daylight Solutions) which was pulsed at 40 Hz using an SRS DS345 function generator. The IR beam, with wavelengths varying from 8.3 μm to 10.4 μm, was focused onto the cantilever (Figure 4.3). In addition, the photothermal spectrum of the bi-material cantilever filled with water shown in Figure 4.4 was collected and used for reference correction. All the samples were positioned into the device by applying a negative pressure at the outlet of the bi-material microfluidic cantilever.
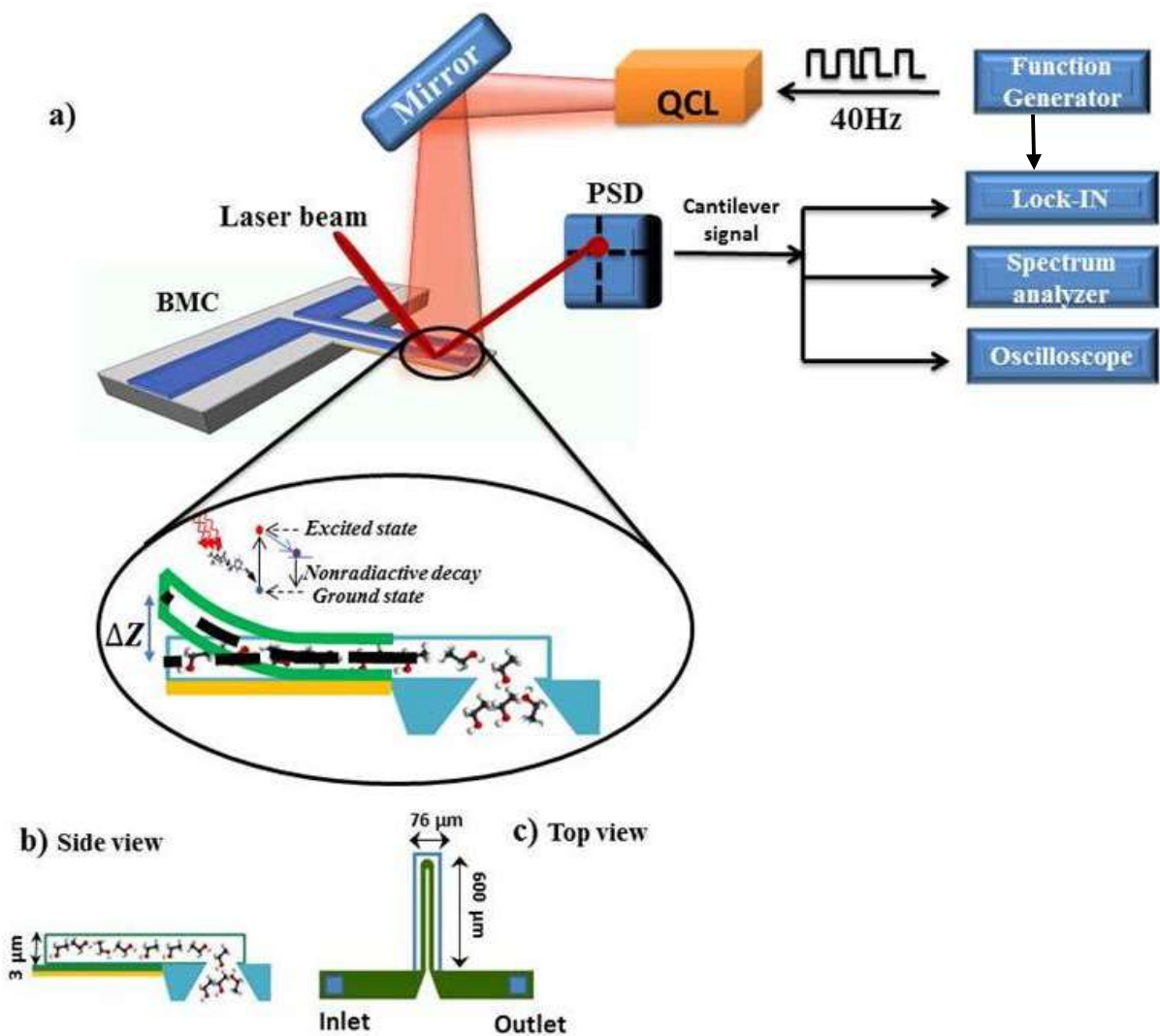
Figure 4.3. a) Experimental set-up to collect IR spectrum of ethanol-water mixtures and a schematic representing photothermally induced deflection of the cantilever, b) cross-section of the microfluidic cantilever, and c) top view of the microfluidic cantilever.
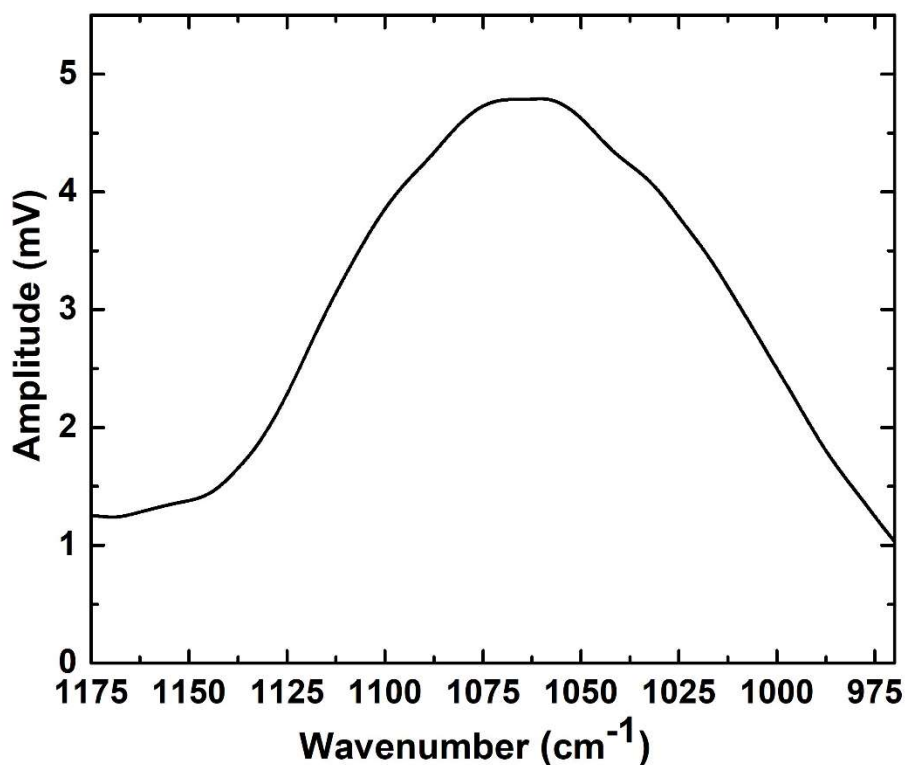
Figure 4.4. Photothermal spectrum of the bi-material cantilever filled with water used for reference correction.

4.3.4. Data collection

After loading the sample in the bi-material microfluidic cantilever, IR spectra of ethanol-water mixtures were collected for 20-100 wt% ethanol (EtOH) solutions. IR spectra of each concentration was collected three times. The frequency of the cantilever was monitored as an indicator of the proper loading of the samples in the cantilever as well as the proper removal of the solutions.

4.4. Results and discussions

4.4.1. Spectrum collection and reproducibility

The principle of photothermal cantilever deflection spectroscopy is based upon measuring very small changes in thermal energy released after infrared radiation is absorbed by the molecules. After the molecules are illuminated by the IR radiation, if the radiation matches the vibration energy of the molecular bonds, they will be excited to a higher energy level. Eventually during the relaxation process the vibrational energy will be lost in the form of heat. The generated heat can be monitored by the deflections of the bi-material cantilever. Photothermal deflections of the cantilever at different wavenumbers represent the IR spectrum of the samples.

The photothermal microfluidic cantilever deflection spectra of ethanol-water mixtures are presented in Figure 4.5 to Figure 4.13. Each figure shows three different spectra collected using a bi-material microfluidic cantilever platform where concentrations are unvaried.
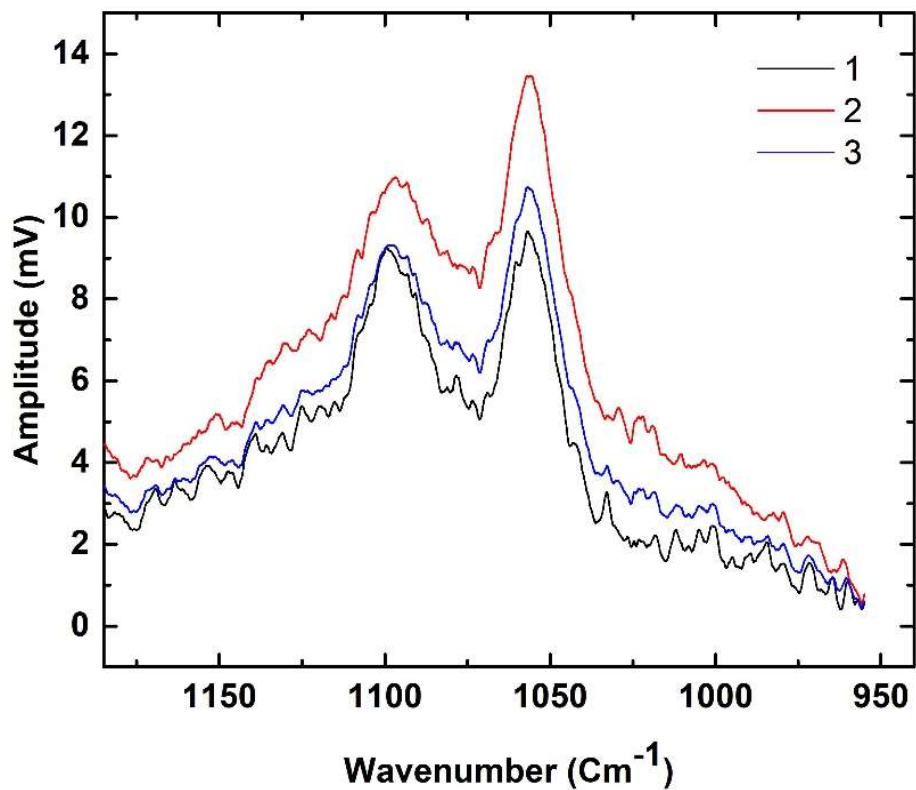
Figure 4.5. Photothermal cantilever deflection spectra of 20 wt% EtOH from 1180 cm^{-1} to 940 cm^{-1}. Number 1, 2, and 3 indicate different measurements of the same concentration.
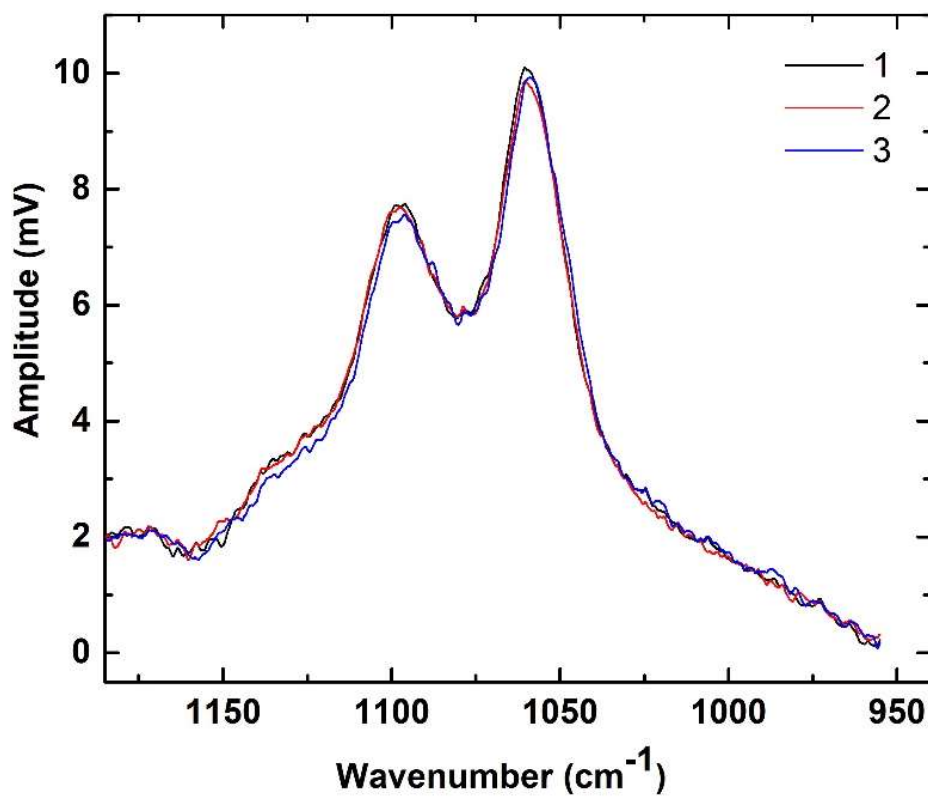
Figure 4.6. Photothermal cantilever deflection spectra of 30 wt% EtOH from 1180 cm^{-1} to 940 cm^{-1}. Number 1, 2, and 3 indicate different measurements of the same concentration.
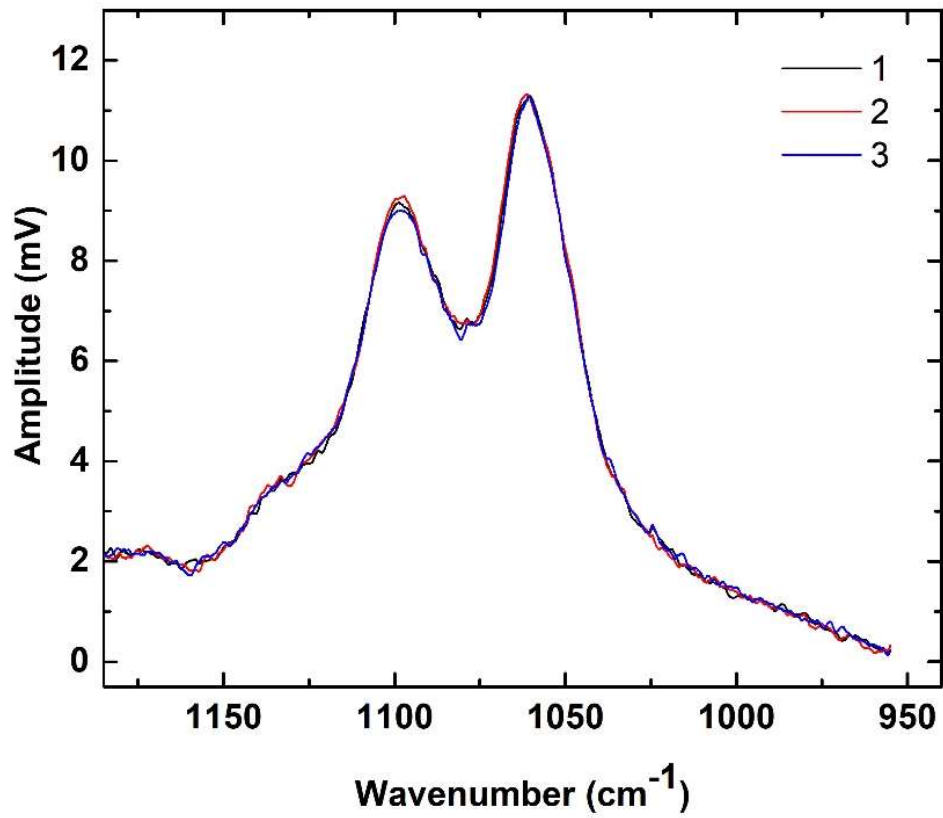
Figure 4.7. Photothermal cantilever deflection spectra of 40 wt% EtOH from 1180 cm^{-1} to 940 cm^{-1}. Number 1, 2, and 3 indicate different measurements of the same concentration.

Figure 4.8. Photothermal cantilever deflection spectra of 50 wt% EtOH from 1180 cm⁻¹ to 940 cm⁻¹. Number 1, 2, and 3 indicate different measurements of the same concentration.
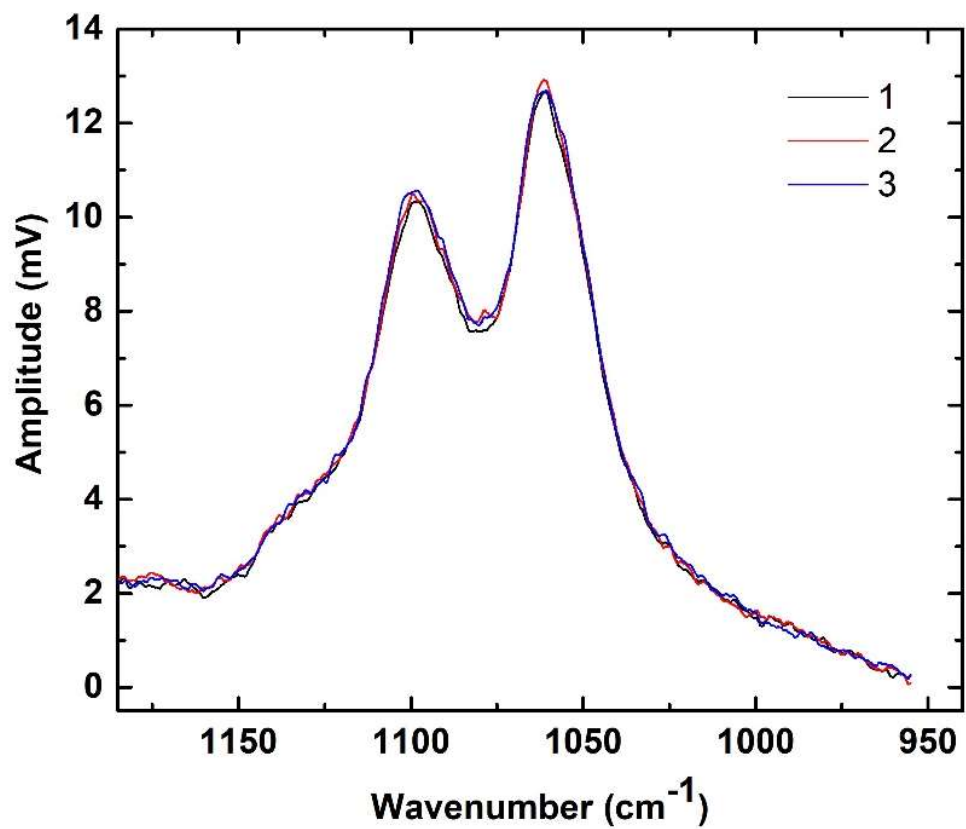
Figure 4.8. Photothermal cantilever deflection spectra of 50 wt% EtOH from 1180 cm^{-1} to 940 cm^{-1}. Number 1, 2, and 3 indicate different measurements of the same concentration.
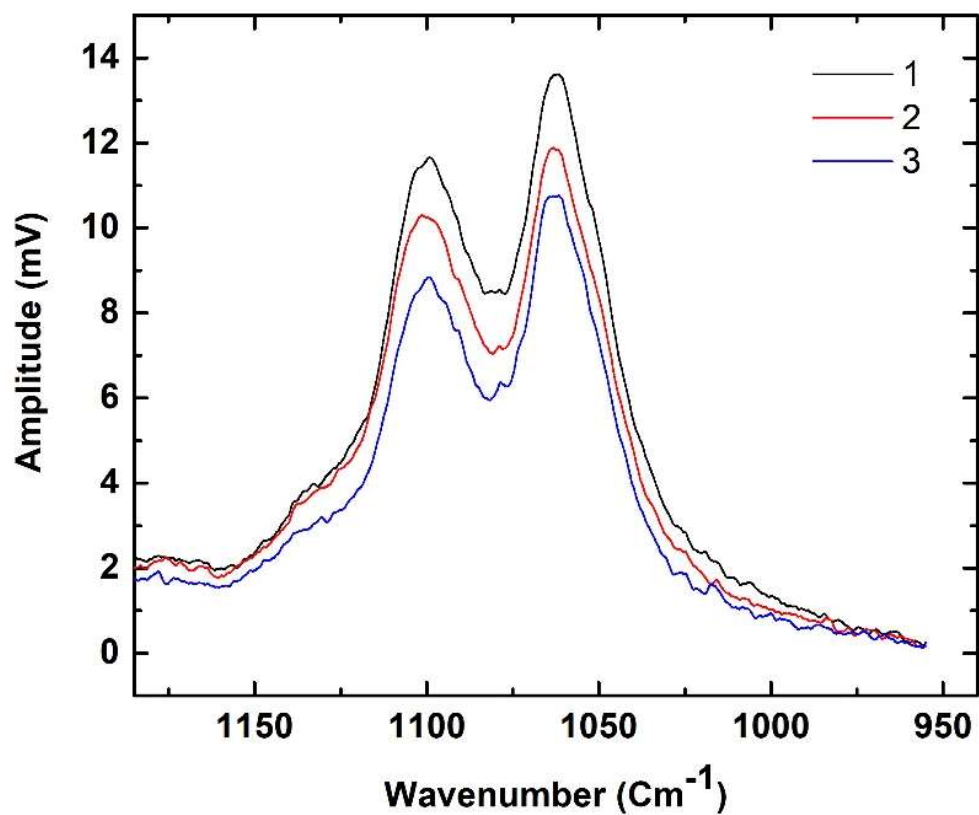
Figure 4.9. Photothermal cantilever deflection spectra of 60 wt% EtOH from 1180 cm^{-1} to 940 cm^{-1}. Number 1, 2, and 3 indicate different measurements of the same concentration.
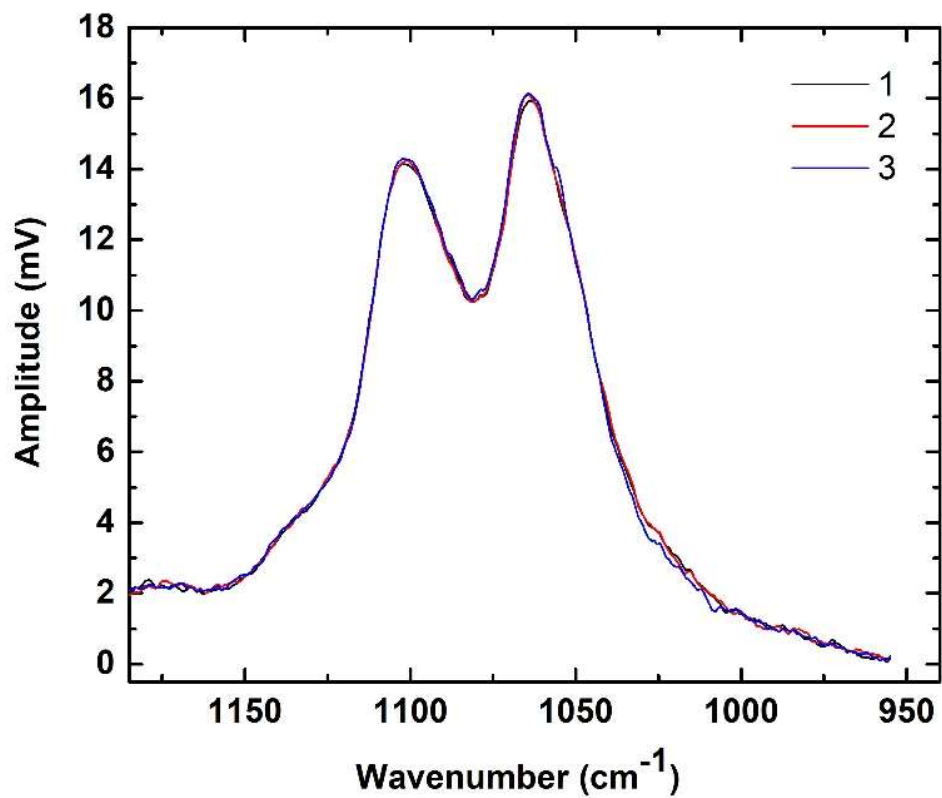
Figure 4.10. Photothermal cantilever deflection spectra of 70 wt% EtOH as wavenumber changes from 1180 cm^{-1} to 940 cm^{-1}. Number 1, 2, and 3 indicate different measurements of the same concentration.
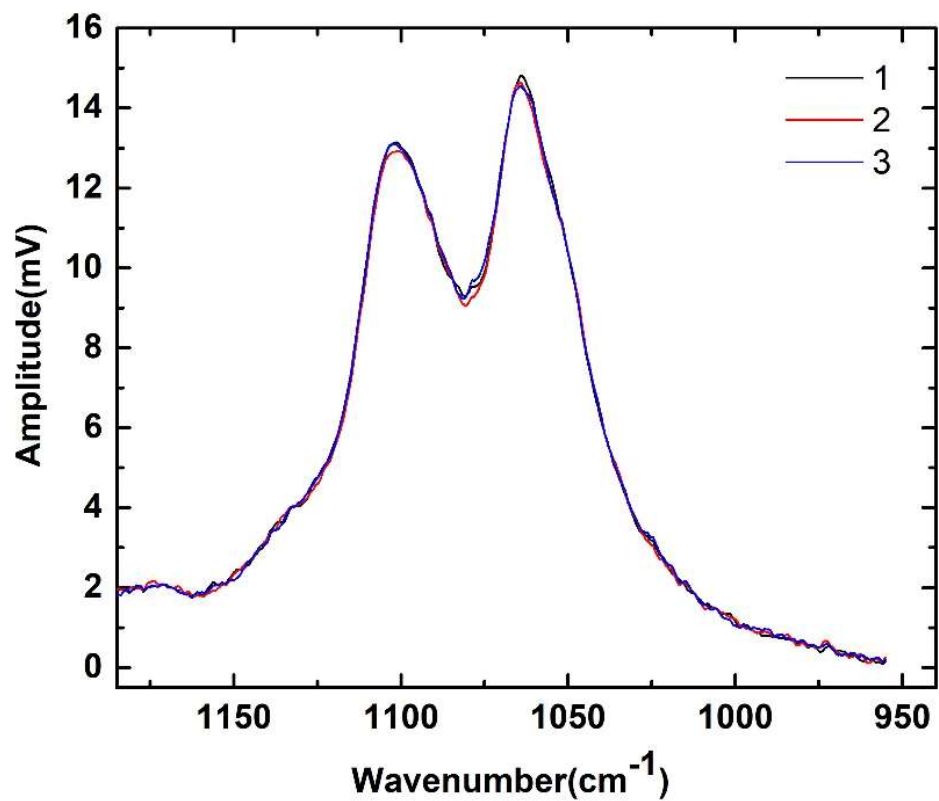
Figure 4.11. Photothermal cantilever deflection spectra of 80 wt% EtOH as wavenumber changes from 1180 cm⁻¹ to 940 cm⁻¹. Number 1, 2, and 3 indicate different measurements of the same concentration.
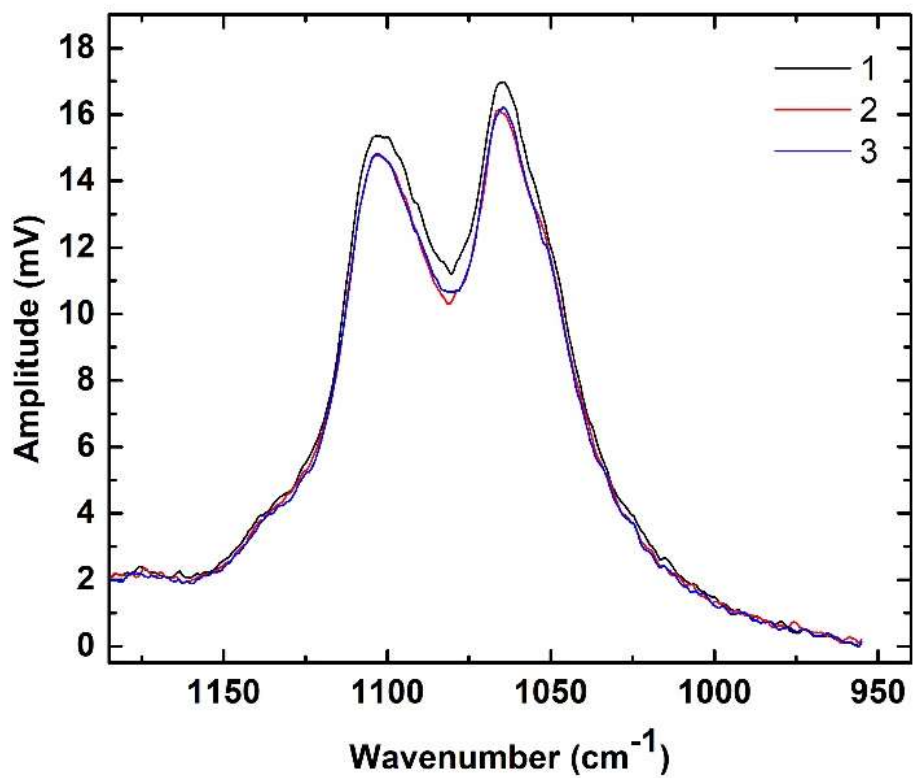
Figure 4.12. Photothermal cantilever deflection spectra of 90 wt% EtOH as wavenumber changes from 1180 cm^{-1} to 940 cm^{-1}. Number 1, 2, and 3 indicate different measurements of the same concentration.
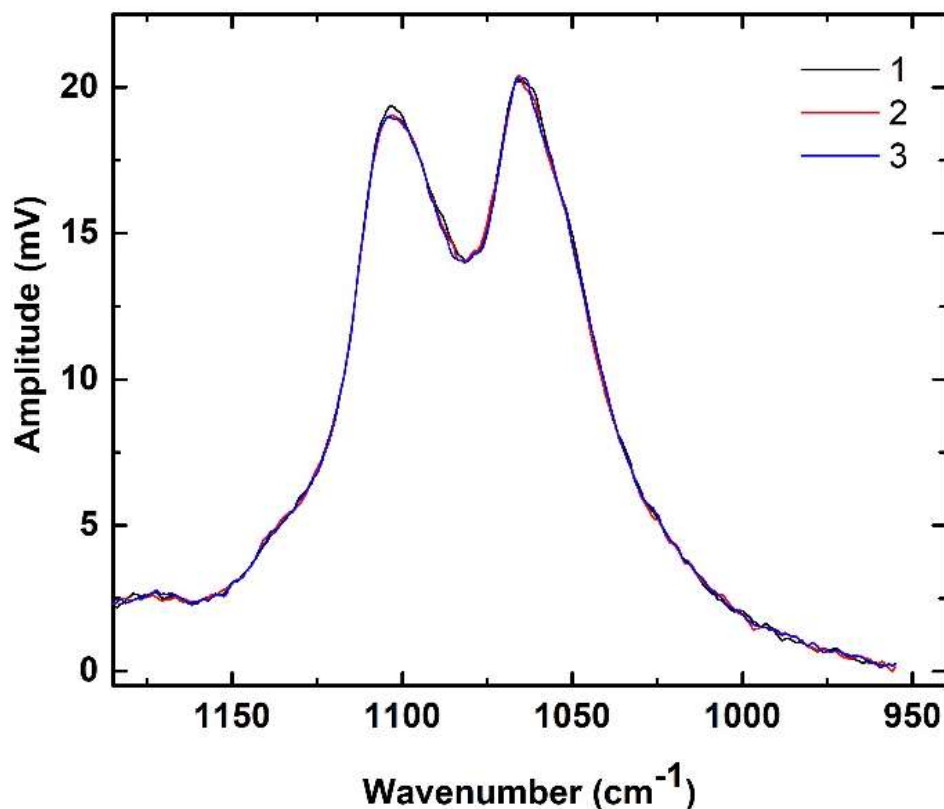
Figure 4.13. Photothermal cantilever deflection spectra of 100 wt% EtOH as wavenumber changes from 1180 cm^{-1} to 940 cm^{-1}. Number 1, 2, and 3 indicate different measurements of the same concentration.

As evident from the spectra of the mixtures (Figure 4.5 to Figure 4.13), there are two distinguishable peaks in 1000-1200 cm^{-1} region in all the collected spectra. These peaks are consistent with the ethanol IR spectrum recorded by the National Institute of Standards and Technology (NIST) (Figure 4.14). For the majority of the collected spectra, both peak heights and peak positions are reproducible, at a fix concentration of ethanol, as shown in each figure (Figure 4.5 to Figure 4.13). There are some variations in the peak heights for 20 wt% and 60 wt% EtOH solutions; however, these variations do not influence the peak positions.

Figure 4.14. IR absorption spectrum of ethanol solution with 4 cm^{-1} resolution from the National Institute of Standards and Technology.

4.4.2. Origin of absorption peaks in the IR spectrum

Ethanol consists of two conformers, anti and gauche, in equilibrium. Each of the conformers shows their own associated absorption bands in the IR spectra.[47,48] $C-C-O$ asymmetric stretch in ethanol, also referred to as $C-O$ stretch, absorbs IR radiation in two distinguishable wavenumbers in 1000-1200 cm^{-1} region. These two absorption peaks are approximately 40 cm^{-1} away from each other and are related to the anti and gauche conformers of ethanol.[1,47] In this work, $C-O$ stretch is referred to as $C-C-O$ asymmetric stretch as it is more appropriate.[1] The more intense peak in the region, located around 1045 cm^{-1}, belongs to the $C-C-O$ asymmetric stretch of the anti conformer and this peak is more often referred to in the studies. The higher intensity of this peak compared to the gauche conformer's peak is due to the more favourability of the anti conformer in the mixture.[47] In this work, the absorptions of both anti and

gauche conformers were investigated. The average peak position for both conformers are plotted as ethanol's concentration varies in the mixture (see Figure 4.15). Inset graph in Figure 4.15 represents averaged IR spectra of binary mixtures collected using the PCDS set-up.
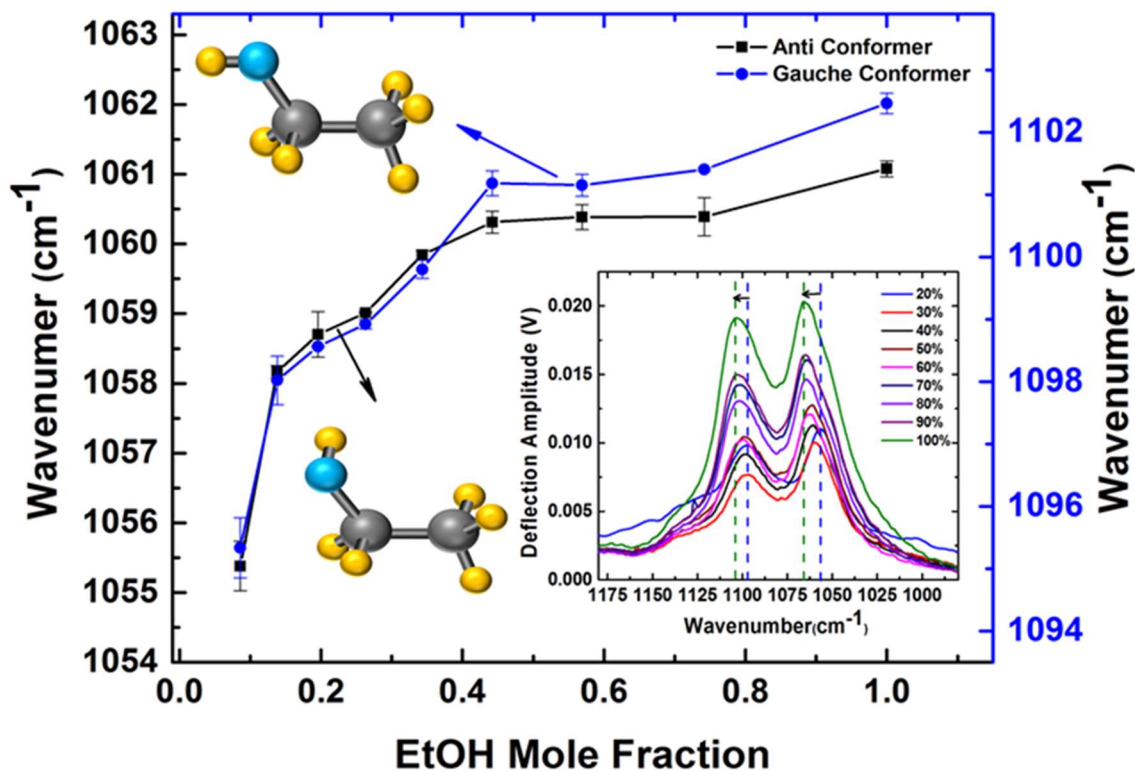
Figure 4.15. Effect of concentration on IR peak position (ν) for anti and gauche conformers of ethanol. Concentration of ethanol changes from 20 wt% to 100 wt%. Inset graph shows IR spectra of the binary mixtures collected using PCDS method where purple dashed are fixed at peak positions for ethanol 20 wt% and olive dashed are fixed at peak positions for ethanol 100 wt%. Error bar refers to the standard deviation of the peak positions from mean peak position at each concentration.

4.4.3. Nonlinear changes in absorption peak positions

The results show that IR absorption peak positions for both conformers are nonlinear functions of ethanol concentration. However, the results of Burikov S et al. and Mizuno K et al. show no changes or linear changes in the absorption peak positions as ethanol concentration changes.(20,49) As a part of this work, attenuated total reflection (ATR) technique was also employed to compare IR spectra of ethanol-water mixtures using both ATR-FTIR and PCDS techniques. Original ATR-FTIR spectra of the binary mixtures are presented in Figure 4.16. Normalized peak position related to the anti conformer obtained using ATR-FTIR, FTIR and Raman spectroscopy along with PCDS results are compared in Figure 4.17.
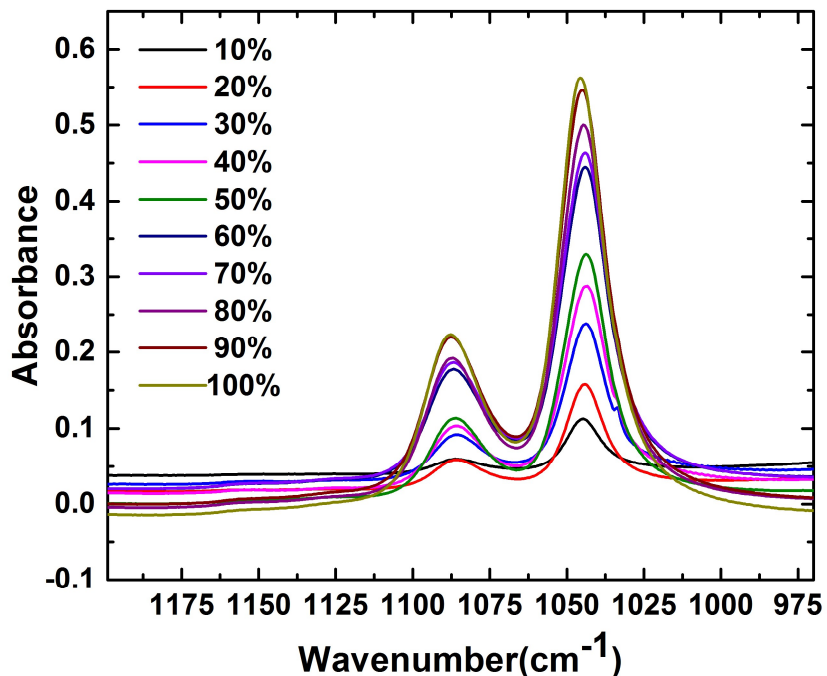
Figure 4.16. ATR-FTIR spectrum of EtOH-water mixtures as concentration of EtOH changes from 10 wt% to 100 wt%.
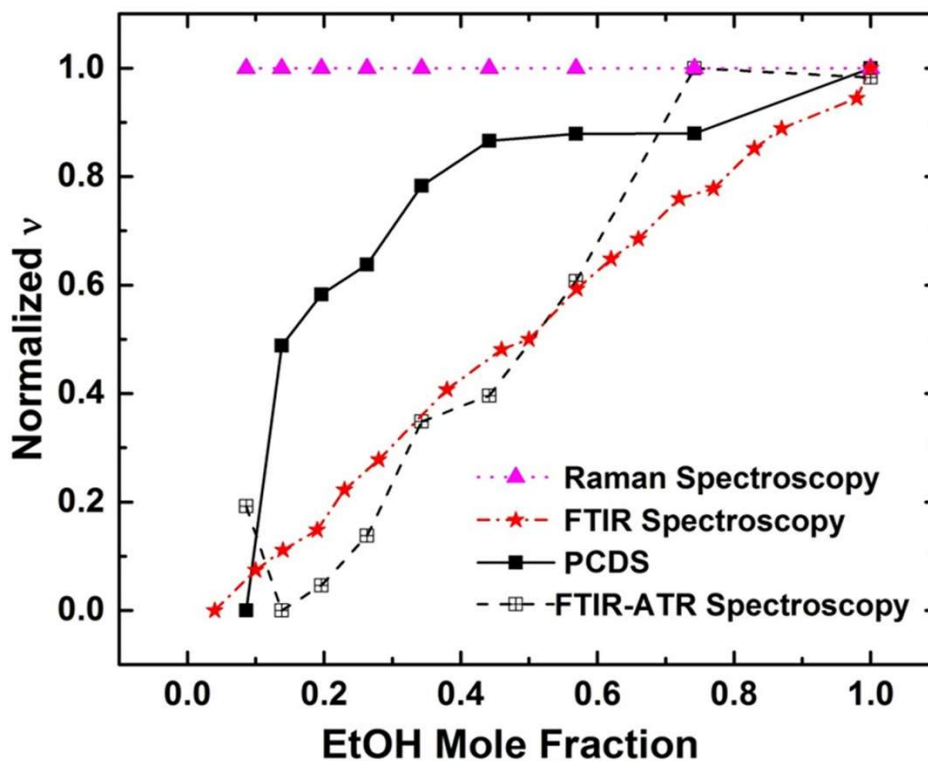
Figure 4.17. Normalized peak positions for the anti conformer as a function of ethanol concentration using Raman, FTIR, ATR-FTIR, and photothermal spectroscopy. (▲) shows reported results of Burikov S et al. using Raman spectroscopy, (★) shows results of Mizuno et al. using FTIR spectroscopy,(⊞) and (■) show our experimental results using ATR-FTIR spectroscopy and PCDS, respectively.

In order to understand the nonlinearity between absorption peak positions and concentration of the mixtures, we started from Hooke's law. Using Hooke's law, atoms and the connecting bonds can be modeled as a simple harmonic oscillator. Therefore, vibrational frequency of a chemical bond (f) in the molecule can be related to the force constant (k) and reduced mass (m^*) as:

$$f = \frac{1}{2\pi}\sqrt{\frac{k}{m^*}}\ . \tag{4.1}$$

Frequency of oscillation can be expressed in terms of wavenumber (v) using $f = Cv$, where C is the wave's velocity. When a molecule that carries the charge dq experiences an electric field E, a shift of $dx=Edq/k$ develops in the equilibrium position of the molecule. The change in equilibrium position results in an induced dipole $\mu = E(dq)^2/k$. In the new equilibrium position, the charge separation changes, and accordingly, the correlated bond stiffness in the molecule changes. Thus, molecule excitation occurs with absorption of IR light with slightly different energy (frequencies). IR absorption wavenumber at any equilibrium position of the molecule can be related to the internal electric field created in the binary mixture, due to the polar media surrounding the analyte. To do so, associated force constant from induced dipole relation must be substituted into Equation 4.1, which results in the following:

$$v = \frac{dq}{2\pi C}\sqrt{\frac{E}{m^*}}\sqrt{\frac{1}{\mu}}\ . \tag{4.2}$$

Equation 4.2 shows that the absorption peak position is nonlinearly related to the induced dipole moment in the mixture resulting from changes in the concentration.

Figure 4.18 shows the normalized IR abortion peak position for both anti and gauche conformers as a function of the scaled dipole moments of ethanol, corresponding to each concentration of the mixture. Not surprisingly, IR absorption wavenumber, v, follows a power law dependence on inverse dipole moment, $1/\mu$, of ethanol in the mixture with R^2

of 0.92 for the anti and R^2 of 0.97 for the gauche conformer. This relationship between v and $1/\mu$ agrees with Equation 4.2. According to Equation 4.2 the slope of the relationship between v and $1/\mu$ can be associated to the electric field affecting the ethanol molecule, as well as ethanol's effective mass. Power law dependence between v and $1/\mu$ indicates that as concentration of ethanol in the mixture increases, the slope of v and $1/\mu$ dependence decreases. This result is consistent with the results reported by Noskov SY et al. on the decrease in dipole moment of ethanol in the binary mixtures due to increases in ethanol concentration.(50) For comparison of our technique with ATR-FTIR, the relationship between absorption peak positions and dipole moments, v vs $1/\mu$ is plotted for both anti and gauche conformers using ART-FTIR data (see Figure 4.19).
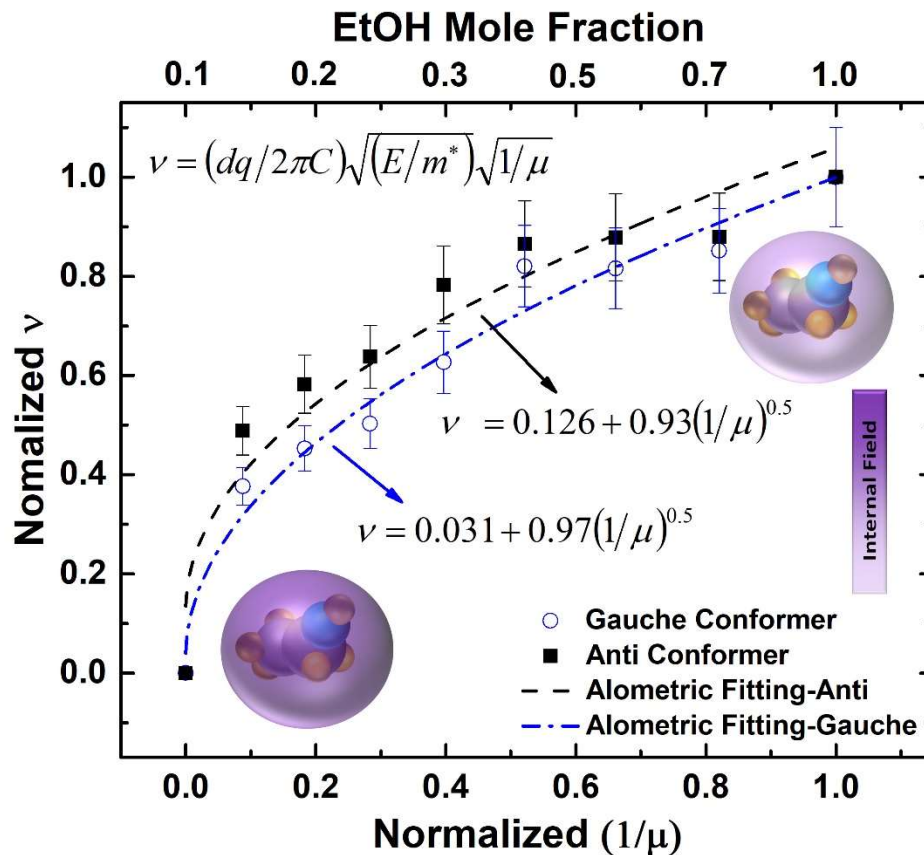
Figure 4.18. Peak position (ν) dependence on ($1/\mu$) of ethanol, as concentration of ethanol changes from 20 wt% to 100 wt%. The dipole moments, correspond to mixture concentrations in the experiments as derivable from reference 50, presented in a normalized scale. Peak positions were obtained from PCDS experiments. Normalized peak positions vs normalized ($1/\mu$) follows a power law relation ($R^2 = 0.92$ for the anti conformer and $R^2 = 0.97$ for the gauche conformer).
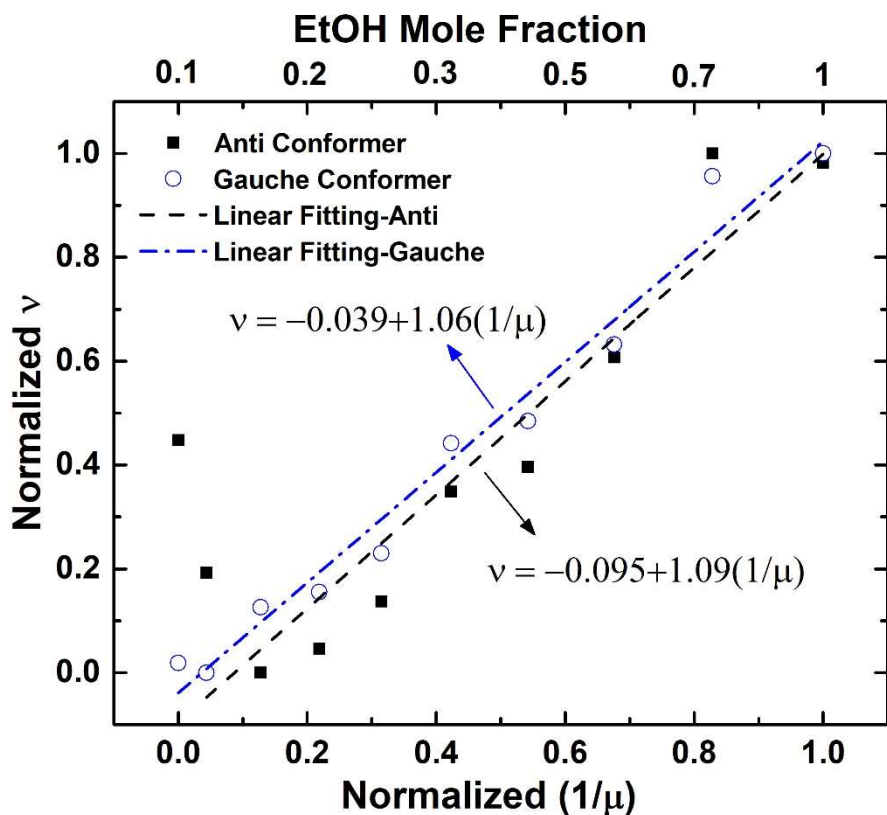
Figure 4.19. Peak positions (v) for this figure are related to ATR-FTIR spectrum. Normalized peak positions relation with normalized ($1/\mu$) follows a linear relation ($R^2 = 0.87$ for the anti conformer and $R^2 = 0.97$ for the gauche conformer). 10 wt% ethanol data point is excluded for linear fitting of the anti conformer.

Figure 4.19 shows that peak positions have a linear relation with inverse of dipole moments, $1/\mu$, for both anti and gauche conformer. The linear fit relations are shown in the figure and the R^2 of 0.87 and 0.97 are obtained for fitting associated to the anti and the gauche conformers, respectively. Since dipole moments of ethanol can be affected by temperature, the variation in the enthalpy of mixing might be the reason for the considerably higher peak position for anti conformer at 10 wt%, shown in Figure 4.19. Compared to FTIR spectroscopy, ATR-FTIR spectroscopy is a powerful technique and

only requires a small volume of sample. However, the implementation of the set-up limits us from exploring intermolecular interactions of volatile samples, where the sample may evaporate and leads to undesirable changes in concentration. In addition, PCDS technique presented in this work requires at least four orders of magnitude less sample comparing to the ATR-FTIR.

4.4.4.   Changes in the peak intensity

Another important feature in an IR spectrum is the absorption peak intensity. Absorption peak intensity can be related to the concentration through Beer-Lambert's Law shown in Equation 4.3 where absorbance, A, is linearly related to concentration, c, of an analyte and proportionality constants are absorptivity, ε, and extinction length, l.(1)

$$A = \varepsilon \, l \, c \tag{4. 3}$$

Figure 4.20 presents IR absorption intensity, obtained using PCDS, at a fixed wavenumber as a function of ethanol concentration.
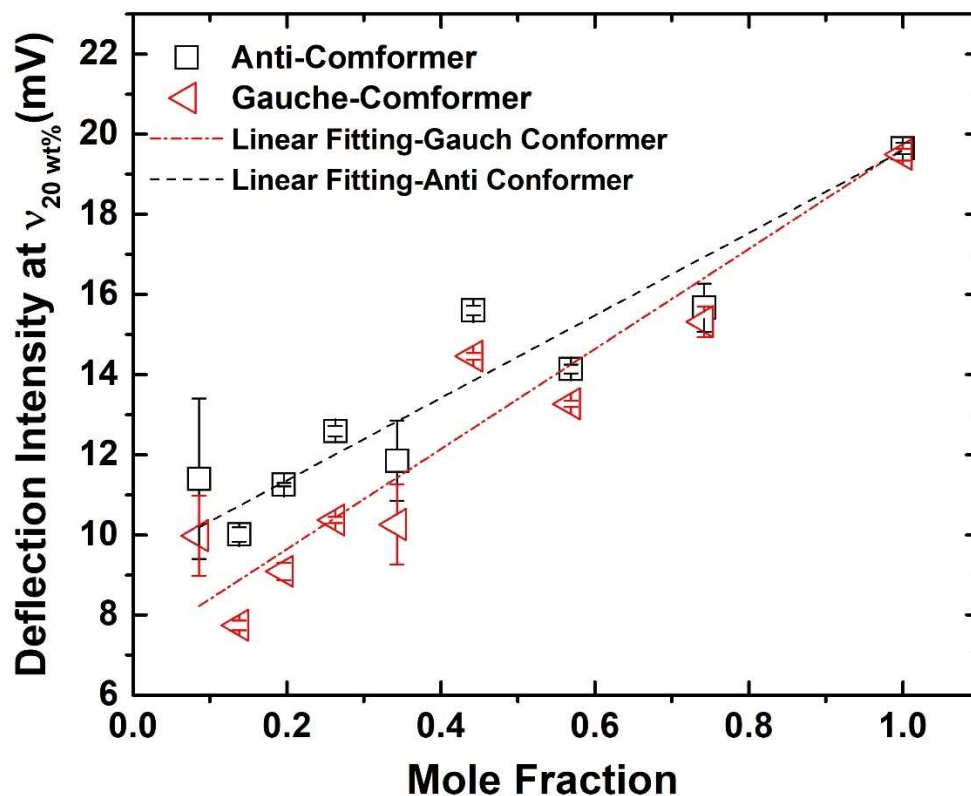
Figure 4.20. IR absorbance intensity relation with concentration, changes in the cantilever deflection for both anti and gauche conformers at different concentrations while wavenumber is fixed at the peak position of 20 wt% ($\nu_{20wt\%}$). Linear fits of the anti and the gauche conformer show a R^2 of 0.93 and 0.86, respectively.

During the interaction with the IR wave, $\partial\mu/\partial x$ (where ∂x is change in bond distance) of the molecule can change due to the complex interactions between ethanol and water at different concentrations. Because absorptivity, ε, depends on $(\partial\mu/\partial x)^2$,(1) any changes in concentration may cause a deviation in wave-matter interactions and, consequently, the overall absorbance magnitude. Throughout the course of the experiments, the polarization of the laser light's electric field remained the same. Thus,

the only influencing factor on vibrational transition moment angles (VTMAs) comes from orientations of the ethanol resulting from ethanol-water interactions.

To investigate the contribution of the dipole moment of ethanol upon the cantilever's deflection, the published data from reference 50 was used, where contributions of ethanol component to dielectric constant of the mixture was computed from fluctuations of the dipole moment of the simulation box (see Equation 4.4).

$$\varepsilon = \varepsilon_\infty + \frac{4\pi}{3\langle V \rangle k_B T}\left(\langle M^2 \rangle - \langle M \rangle^2\right) \tag{4.4}$$

where M is the total dipole moment of the box and ε_∞ (high frequency contribution) is 1.69.(50) The results show that ethanol contribution to the cantilever deflection intensity changes as a function of concentration, which agrees with the contribution dependence of fluctuations of μ within the simulation box resulting from clustering of the solvent and solute molecules at different concentrations. Fluctuation of μ is presented in terms of, ε , being the dielectric constant, in Figure 4.21.(50)
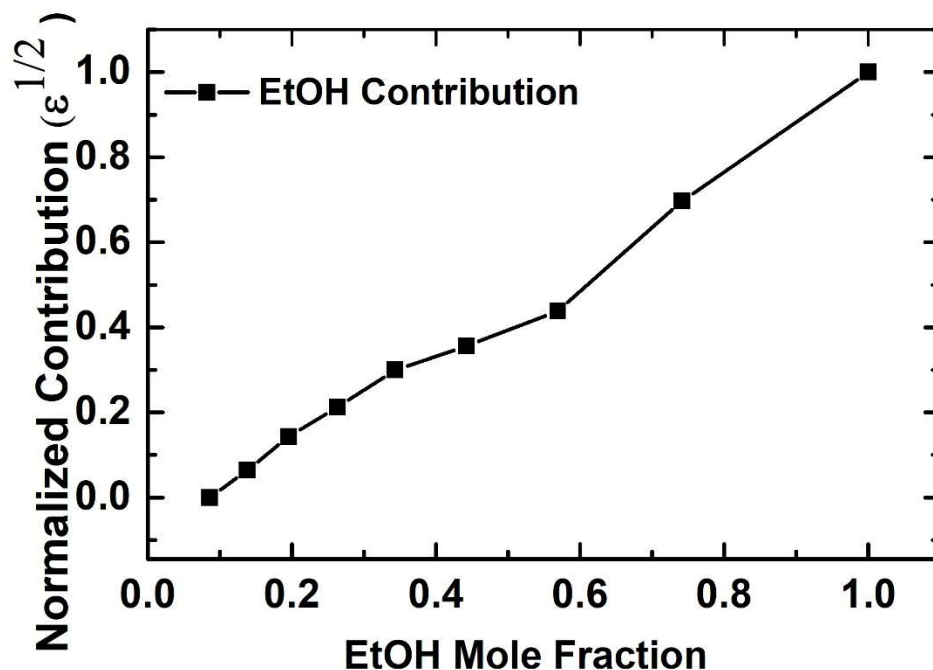
Figure 4.21. Normalized variation in $\sqrt{\varepsilon}$ of ethanol in the binary mixture as concentration changes (unprocessed data are from reference 50).

Even though overall changes in the deflection of the cantilever (shown in Figure 4.20) as a function of concentration shows a linear trend, consistent with Beer-Lambert's Law, there are anomalous points at 20 wt% and 70 wt% (i.e., at $X_{EtOH} = 0.09$ and $X_{EtOH} = 0.44$, respectively where X_{EtOH} stands for ethanol mole fraction). Since absorbance intensity does not increase linearly with concentration for all the concentrations, one may conclude that changes in the transition dipole moment are not linearly increasing with the concentration. This effect may be indication of clustering of ethanol and water, as reported by neutron diffraction measurements and molecular dynamics (MD) models performed with approximately 10^8 molecules, whereas our experiments are done with approximately 10^{15} molecules.(50,51) At $X_{EtOH} = 0.7$ most of the water forms small clusters and only a small fraction of the water compound is monomeric.(50) In contrast,

at X_{EtOH} slightly less than 0.5 clusters of all sized can be observed.(50,52) This could explain why the IR absorption intensity at $X_{EtOH} = 0.44$ is higher than $X_{EtOH} = 0.57$, which cannot be explained by Beer-Lambert's Law.

At very low concentrations, water molecules are reported to be densely packed around the hydrophobic tail of the alcohol resulting in a compressive effect from water which causes the minimum in partial molar volume at $X_{EtOH} = 0.07$.(53) At this concentration, water molecules are in the hydration shells of ethanol molecules.(53) A higher amplitude of deflection at 20 wt% for the anti conformer could be as a result of the presence of water in the hydration shell of ethanol, which possibly makes the presence of the anti conformer even more favorable than the gauche conformer in the mixture.

Although other experimental techniques could not directly measure the distribution of molecular dipole moments in the condensed phase, such changes could possibly be reflected in the response of a bi-material microfluidic cantilever. Local (electro) chemical environment can not only change the average value of electrostatic properties, such as dipole moments of molecules, but also the distributions of molecular dipole moments. Our results, as shown in Figure 4.22 to Figure 4.24, reveal that the spectrum of the binary mixture at 20 wt%, where the solution is dominated by water molecules, has a lower quality factor than those with higher concentrations of ethanol. The lower quality factor corresponds to a higher dissipation or relaxation losses and is in agreement with reported broader dipole moment distribution at $X_{EtOH} = 0.1$, comparing to $X_{EtOH} = 0.5$ and $X_{EtOH} = 0.9$ due to a stronger polarization of the ethanol by the bulk water-like environment.(54) However, further investigations are required before one can make a certain conclusion on

measuring distribution of molecular dipole moments using a bi-material microfluidic cantilever device.

4.5. Material and methods

4.5.1. Deposition of a gold layer

Fabricated cantilevers were constructed of low-stress LPCVD silicon nitride. To make the microfluidic cantilever sensors usable for photothermal deflection spectroscopy, a second metallic layer is required to be deposited on the device. To make the cantilever chips ready for the deposition process, they were cleaned with acetone and alcohol. The cleaned chips were placed face-down on a glass slide, using a piece of double-sided tape. After the glass slide was placed in a Cressington 308R multi coater, a Cr adhesion layer was sputtered on the back of the chip (Cr enhances the adhesion of Au to silicon nitride cantilevers). In the same multi coater, a 250 nm of Au layer was then deposited on the back of the cantilever devices.

4.5.2. PDMS fabrication

To make the PDMS sealing layer, Sylgard 184 base and curing agent were mixed in a 10 to 1 ratio by weight. To remove bubbles formed during the mixing process, the mixture was degassed. Then, a thin layer of the mixture was spin coated on a glass slide with spin speed of 200 RPM for 2 minutes and then cured for 2 hours in a vacuum oven at 80 °C. Curing under vacuum ensures the removal of gasses entrapped in the PDMS

layers. Eventually, individual squares with proper holes in them were laser cut in the PDMS layers.

4.5.3. Chemicals

All experiments were conducted with milli-Q water (purified using Milli-Q Advantage A10) and with absolute ethanol purchased from Sigma Aldrich (with concentration higher than or equal to 99.8 (GC)).

4.5.4. Spectrum decomposition

After the IR spectra of each binary mixture of ethanol-water were collected, the spectra were decomposed using the following function:

$$y = y_0 + A\left[\gamma\frac{2}{\pi}\frac{w}{4(x-x_c)^2+w^2} + (1-\gamma)\frac{\sqrt{4\ln2}}{w\sqrt{\pi}}\exp\left(\frac{-4\ln2}{w^2}(x-x_c)^2\right)\right]. \qquad (4.5)$$

In this function, y is the profile intensity, y_0 is the offset, x_c is the center wavenumber, A is the area, w is the full width half maximum (FWHM), and γ is the profile shape factor. Decomposition of spectra for different concentrations are presented in Figure 4.22 to Figure 4.24.
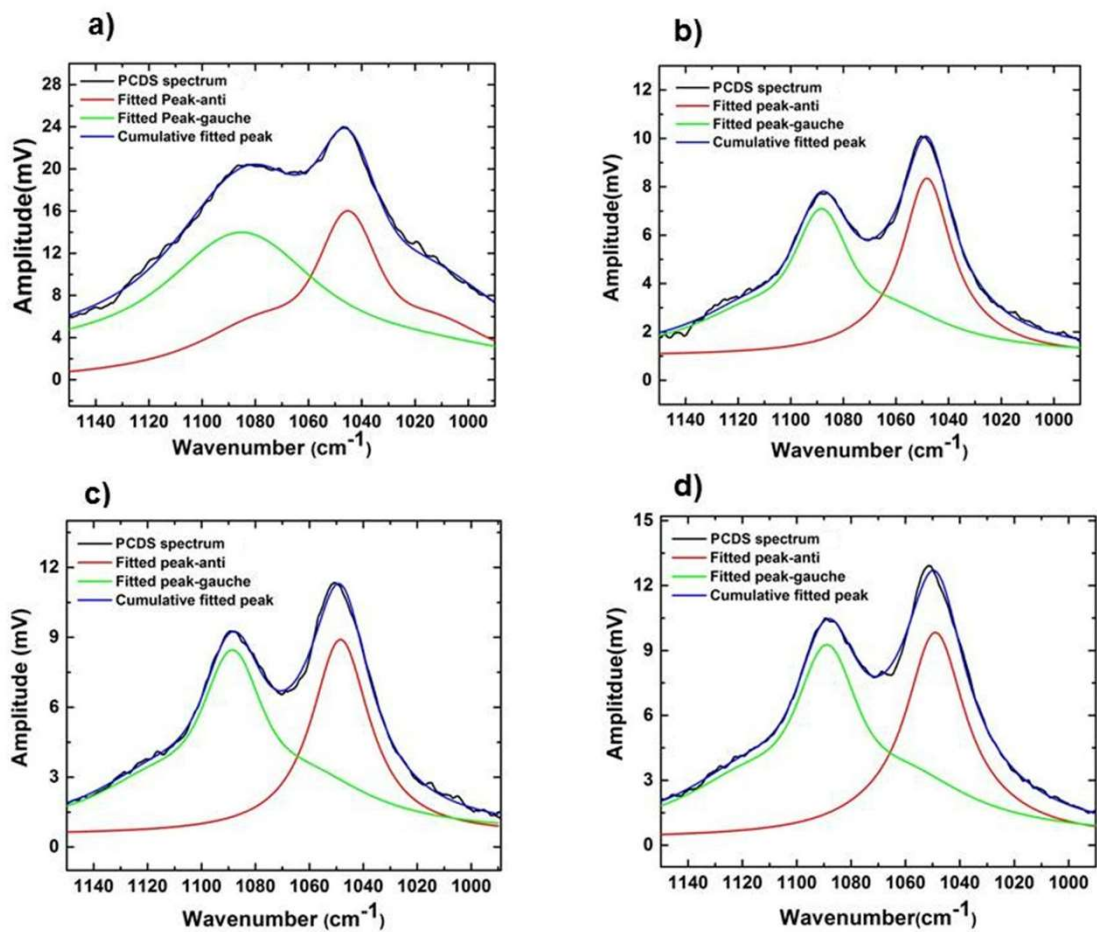
Figure 4.22. IR spectra obtained by the PCDS technique and decomposition of the spectra for the following concentrations of EtOH: a) 20 wt%, b) 30 wt%, c) 40 wt%, and d) 50 wt%.
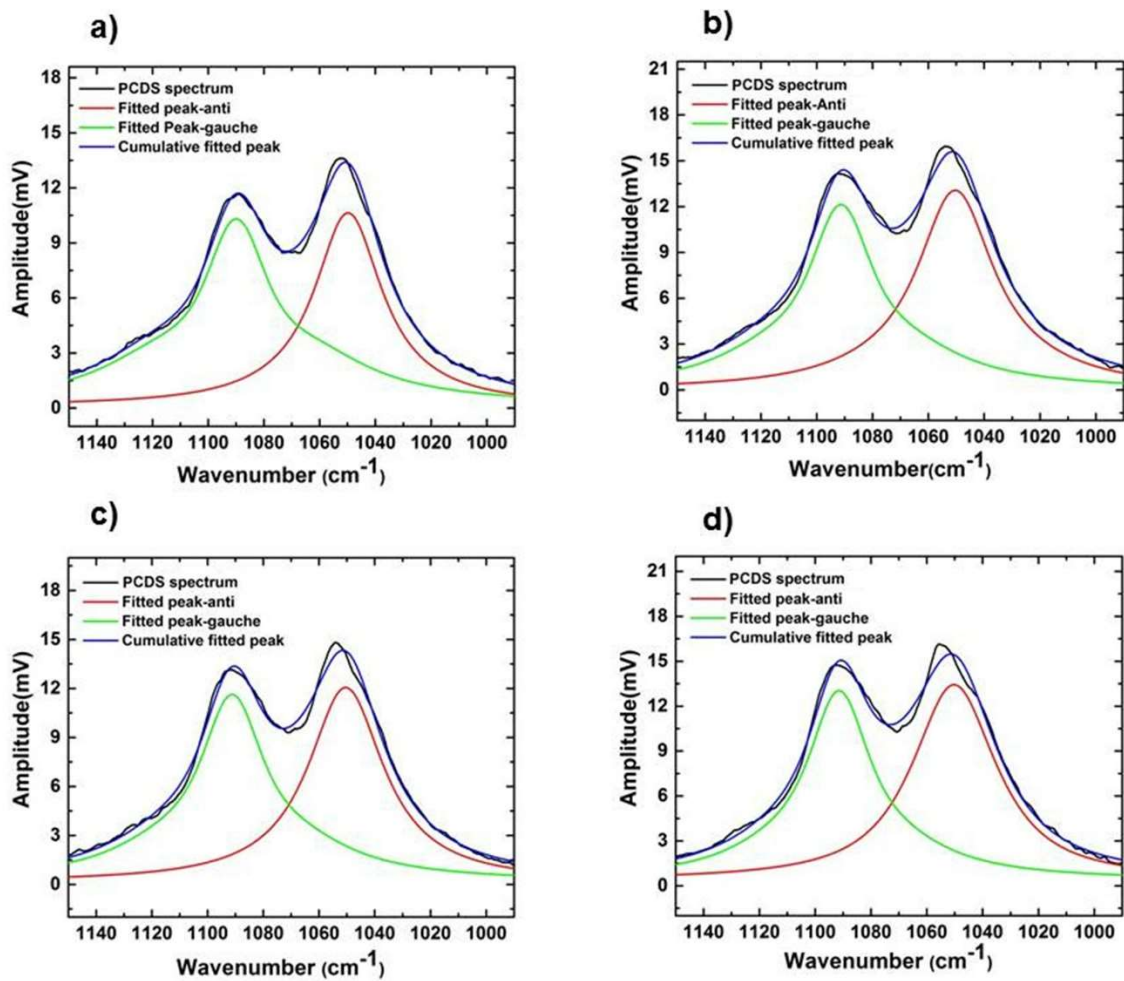
Figure 4.23. IR spectra obtained by the PCDS technique and decomposition of the spectra for the following concentrations of EtOH: a) 60 wt%, b) 70 wt%, c) 80 wt%, and d) 90 wt%.
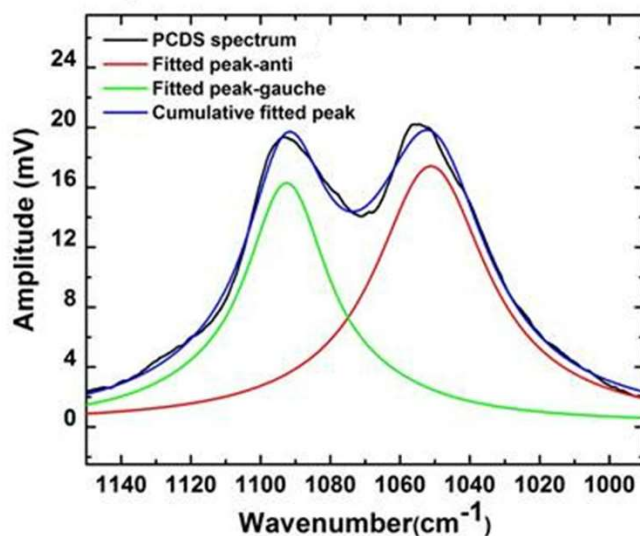
Figure 4.24. IR spectrum obtained employing PCDS technique for 100 wt% EtOH and decomposition of the spectra.

4.5.5. ATR-FTIR spectroscopy

Ethanol-water binary mixtures were characterized using a standard ATR-FTIR technique. A Thermo Scientific Nicolet, Nexus 670 system with a Smart Performer ZnSe window was used to collect ATR-FTIR spectra of the binary mixtures. To collect the IR spectra of the samples, 40 µL of the liquid was enough to fully cover the ZnSe window. However, 100 µL of the mixture was placed on the ZnSe window to reduce the effect of ethanol evaporation, which would change the concentration during the measurements. The minimum number of collected scans was 100 with the resolution of 4 cm^{-1}. The ZnSe window was washed with ethanol and milli-Q water and then air dried after each measurement.

4.6.   Conclusion

The effects of solvent-solute interactions on the absorption peaks related to $C\text{-}C\text{-}O$ of ethanol have been investigated using micromechanical calorimetric spectroscopy to collect IR spectrum of ethanol-water mixtures. This technique offers a means to study and understand dipole dependence on molecular vibrations in confined picoliter volumes of mixtures, previously unexplored due to limitations of volume levels in other analytical techniques. The results presented in this chapter reveal a power law dependence of the IR absorption peak positions on the induced dipole moments of ethanol in the mixtures. In addition, non-linear contributions of ethanol in the IR absorption intensity at a fixed wavenumber can be related to the effects of clustering in the $\partial\mu/\partial x$ which cannot be explained by Beer-Lambert's Law. This technique allows correlations between MD simulations and experimental results where the total number of molecules in question are comparable, as well as liquid matter sensing.

4.7. References

1.	Smith BC. Infrared spectral interpretation: a systematic approach. Boca Raton: Boca Raton: CRC Press; 1999.

2.	Cozzolino D. Infrared spectroscopy theory, development and application. Hauppauge, New York: Nova Science Publishers, Inc; 2013.

3.	Booth RS, Annesley CJ, Young JW, Vogelhuber KM, Boatz JA, Stearns JA. Identification of multiple conformers of the ionic liquid [emim][tf2n] in the gas phase using IR/UV action spectroscopy. Phys Chem Chem Phys. 2016;18(25):17037.

4.	Mohammadi N, Ganesan A, Chantler CT, Wang F. Differentiation of ferrocene D-5d and D-5h conformers using IR spectroscopy. J Organomet Chem. 2012;713:51–9.

5.	Reva ID, Stepanian SG, Adamowicz L, Fausto R. Combined FTIR matrix isolation and Ab initio studies of pyruvic acid: proof for existence of the second conformer. J Phys Chem A. 2001;105(19):4773–80.

6.	Hoffmann W, Marianski M, Warnke S, Seo J, Baldauf C, von Helden G, et al. Assessing the stability of alanine-based helices by conformer-selective IR spectroscopy. Phys Chem Chem Phys. 2016;18:19950–4.

7.	Smith B. Fundamentals of Fourier transform infrared spectroscopy, 2nd ed. Boca Raton, Fla: CRC Press. 2011.

8.	Gimzewski JK, Gerber C, Meyer E, Schlittler RR. Observation of a chemical reaction using a micromechanical sensor. Chem Phys Lett. 1994 Jan;217(5–6):589–94.

9. Barnes JR, Stephenson RJ, Welland ME, Gerber C, Gimzewski JK. Photothermal spectroscopy with femtojoule sensitivity using a micromechanical device. Nature. 1994;372:79–81.

10. Hallsworth JE. Ethanol-induced water stress in yeast. J Ferment Bioeng. 1998;85(2):125–37.

11. Brandts JF, Hunt L. The thermodynamics of protein denaturation. III. The denaturation of ribonuclease in water and in aqueous urea and aqueous ethanol mixtures. J Am Chem Soc. 1967;89(19):4826–38.

12. Nozaki Y, Tanford C. The solubility of amino in aqueous ethanol acids and two glycine dioxane solutions peptides. J Biol Chem. 1971;246(7):2211–7.

13. Chuang W, Young T-H, Wang D-M, Luo R-L, Sun Y-M. Swelling behavior of hydrophobic polymers in water/ethanol mixtures. Polymer (Guildf). 2000;41(23):8339–47.

14. Yaacobi M. Hydrophobic interaction mixtures in water-ethanol mixtures. J Solution Chem. 1973;2(5).

15. Hoogenboom R, Thijs HML, Wouters D, Hoeppener S, Schubert US. Tuning solution polymer properties by binary water–ethanol solvent mixtures. Soft Matter. 2008;4(1):103–7.

16. Kiritoshi Y, Ishihara K. Preparation of cross-linked biocompatible poly(2-methacryloyloxyethyl phosphorylcholine) gel and its strange swelling behavior in water/ethanol mixture. J Biomater Sci Polym Ed. 2002;13(2):213–24.

17. Li F, Men Z, Li S, Wang S, Li Z, Sun C. Study of hydrogen bonding in ethanol-water binary solutions by Raman spectroscopy. Spectrochim Acta Part A Mol

Biomol Spectrosc. 2018;189:621–4.

18. Furukawa K, Judai K. Brownian motion probe for water-ethanol inhomogeneous mixtures. J Chem Phys. 2017;147(244502).

19. Ben-Naim A. Inversion of the Kirkwood-Buff theory of solutions: application to the water-ethanol system. J Chem Phys. 1977;67(11):4884–90.

20. Burikov S, Dolenko T, Patsaeva S, Starokurov Y, Yuzhakov V. Raman and IR spectroscopy research on hydrogen bonding in water-ethanol systems. Mol Phys. 2010;108(18):2427–36.

21. Hu N, Wu D, Cross K, Burikov S, Dolenko T, Patsaeva S, et al. Structurability: a collective measure of the structural differences in vodkas. J Agric Food Chem. 2010;58(12):7394–401.

22. Ahmed MK, Ali S, Wojcik E. The C-O stretching infrared band as a probe of hydrogen bonding in ethanol–water and methanol–water mixtures. Spectrosc Lett. 2012;45(2015):420–3.

23. Dolenko TA, Burikov SA, Dolenko SA, Efitorov AO, Plastinin I V., Yuzhakov VI, et al. Raman spectroscopy of water-ethanol solutions: the estimation of hydrogen bonding energy and the appearance of clathrate-like structures in solutions. J Phys Chem A. 2015;119(44):10806–15.

24. Dolenko T a, Burikov S a, Patsaeva S V, Yuzhakov VI. Manifestation of hydrogen bonds of aqueous ethanol solutions in the Raman scattering spectra. Quantum Electron. 2011;41(3):267–72.

25. Burikov S, Dolenko S, Dolenko T, Patsaeva S, Yuzhakov V. Decomposition of water Raman stretching band with a combination of optimization methods. Mol

Phys. 2010;108(6):739–47.

26.   Nishi N, Takahashi S, Matsumoto M, Tanaka A, Muraya K, Takamuku T, et al. Hydrogen bonding cluster formation and hydrophobic solute association in aqueous solution of ethanol. J Phys Chem. 1995;99:462–8.

27.   Petong P, Pottel R, Kaatze U. Water-ethanol mixtures at different compositions and temperatures. A dieletric relaxation study. J Phys Chem. 2000;104:7420–8.

28.   Brai M, Kaatze U. Ultrasonic and hypersonic relaxations of monohydric alcohol/water mixtures. J Phys Chem. 1992;96(22):8946–55.

29.   Behrends R, Kaatze U. Hydrogen bonding and chain conformational isomerization of alcohols probed by ultrasonic absorption and shear impedance spectrometry. J Phys Chem A. 2001;105(24):5829–35.

30.   Kaatze U. Hydrogen network fluctuations of alcohols. Evidence from ultrasonic, dielectric, and shear impedance spectrometry. Int J Thermophys. 2012;33(4):653–63.

31.   Iwasaki K, Fujiyama T. Light-scattering study of clathrate hydrate formation in binary mixtures of tert-butyl alcohol and water. J Phys Chem. 1977;81(20):1908–12.

32.   Harris KR, Newitt PJ. Diffusion and structure in dilute aqueous alcohol solutions: evidence for the effects of large apolar solutes on water. J Phys Chem B. 1998;102(1):8874–9.

33.   Harris KR, Newitt PJ, Derlacki ZJ. Alcohol tracer diffusion, density, NMR and FTIR studies of aqueous ethanol and 2,2,2-trifluoroethanol solutions at 25°C. J Chem Soc Faraday Trans. 1998;94(14):1963–70.

34. Matsumoto M, Nishi T, Saita M, Takamuku T, Yamagami M, Yamaguchi T. Structure of clusters in ethanol-water binary solutions studied by mass spectrometry and X-Ray diffraction. Bull Chem Soc Jpn. 1995;68(7):1775–83.

35. Pradhan T, Ghoshal P, Biswas R. Structural transition in alcohol – water binary mixtures: a spectroscopic study. J Chem Sci. 2008;120(2):275–87.

36. Gao Q, Zhu Y, Ruan Y, Zhang Y, Zhu W, Lu X, et al. Effect of adsorbed alcohol layers on the behavior of water molecules confined in a graphene nanoslit: a molecular dynamics study. Langmuir. 2017;33(42):11467–74.

37. Allen MP, Tildesley DJ. Computer simulation of liquids. Oxford [England]: Clarendon Press; 1987.

38. Wensink EJW, Hoffmann AC, Van Maaren PJ, Van Der Spoel D. Dynamic properties of water/alcohol mixtures studied by computer simulation. J Chem Phys. 2003;119(14):7308–17.

39. Palinkas G, Bako I. Excess properties of water-methanol mixtures as studied MD simulations. Zeitschrift fur Naturforsch Sect A-A J Phys Sci. 1991;46(1–2):95–9.

40. Zhang C, Yang X. Molecular dynamics simulation of ethanol/water mixtures for structure and diffusion properties. Fluid Phase Equilib. 2005;231(1):1–10.

41. Ludwig R, Gill D., Zeidler D. Molecular reorientation in liquid methanol. Zeitschrift fur Naturforsch Sect A-A J Phys Sci. 1991;94:89–94.

42. Simon JD. Solvation dynamics: new insights into chemical reaction and relaxation processes. Pure Appl Chem. 1990;62(12):2243–50.

43. Laage D, Stirnemann G, Hynes JT. Why water reorientation slows without iceberg formation around hydrophobic solutes. J Phys Chem B. 2009;113(8):2428–35.

44. Ramos D, Tamayo J, Mertens J, Calleja M. Photothermal excitation of microcantilevers in liquids. J Appl Phys. 2006;99(12).

45. Burg TP, Manalis SR. Suspended microchannel resonators for biomolecular detection. Appl Phys Lett. 2003;83(13):2698.

46. Burg TP, Mirza AR, Milovic N, Tsau CH, Popescu G a., Foster JS, et al. Vacuum-packaged suspended microchannel resonant mass sensor for biomolecular detection. J Microelectromechanical Syst. 2006 Dec;15(6):1466–76.

47. Shaw RA, Wieser H, Dutler R, Rauk A. Vibrational optical activity of (S)-l-d-ethanol. J Am Chem Soc. 1990;112(14):5401–10.

48. Scheiner S, Seybold PG. Quantum chemical analysis of the energetics of the anti and gauche conformers of ethanol. Struct Chem. 2009;20(1):43–8.

49. Mizuno K, Miyashita Y, Shindo Y, Ogawa H. NMR and FT-IR studies of hydrogen bonds in ethanol-water mixtures. J Phys Chem. 1995;99(10):3225–8.

50. Noskov SY, Lamoureux G, Roux B. Molecular dynamics study of hydration in ethanol - water mixtures using a polarizable force field. J Phys Chem B. 2005;109(14):6705–13.

51. Dixit S, Crain J, Poon WCK, Finney JL, Soper AK. Molecular segregation observed in a concentrated alcohol-water solution. Nature. 2002;416(6883):829–32.

52. Dougan L, Bates SP, Hargreaves R, Fox JP, Crain J, Finney JL, et al. Methanol-water solutions: a bi-percolating liquid mixture. J Chem Phys. 2004;121(13):6456–62.

53. Tan ML, Miller BT, Te J, Cendagorta JR, Brooks BR, Ichiye T. Hydrophobic

hydration and the anomalous partial molar volumes in ethanol-water mixtures. J Chem Phys. 2015;142(6):064501–6.

54.   Zhong Y, Patel S. Electrostatic polarization effects and hydrophobic hydration in ethanol - water solutions from molecular dynamics simulations. J Phys Chem B. 2009;113(3):767–78.

Chapter 5:

Thermal sensitivity analysis of microfluidic cantilever sensors

5.1. Introduction

In 1993, Gimzewski JK et al.(1) introduced a new form of calorimeter with an approximate sensitivity of 1pJ. This calorimeter was built upon the bending of an aluminum coated silicon-based microcantilever. Later, they applied this approach to obtain the photothermal absorption spectra of fluorescein dye.(2) After the molecule absorbs light and is excited to a higher energy level, some of the absorbed energy releases in the form of heat, during the relaxation process. In 2013, Canetta C and Narayanaswamy A improved the heat sensitivity even further, up to 1 pW.(3) Due to the high sensitivity of bi-metallic microcantilevers to heat, they have been employed for numerous applications, including: detection of subnanograms of RDX and TNT;(4) sensing generated heat by a single mammalian cell;(5) and spectroscopic measurements in a wide range of wavelengths.(6)

Even though the cantilever-based spectrometer is a very promising platform, it is not suitable for spectroscopic measurements in liquid phase, especially water media. This is mainly because operation of the device in liquid media decreases the sensitivity significantly. This challenge can be overcome by confining the liquid in a microfluidic cantilever.(7) Simultaneously, the low resolution as well as low signal to noise ratio of MIR spectroscopy in aqueous media can be addressed by employing a quantum cascade

laser as the light source. This idea was used to extract detailed information on intermolecular interactions between ethanol and water as the IR spectra of the mixture were collected.(8) As this platform has demonstrated its capability in shedding light on intermolecular interactions where ATR-FTIR, Raman, and FTIR spectroscopy reach their limits,(8) further improving the device sensitivity can be valuable in applied liquid spectroscopy. Further improvement in sensitivity of this platform for liquid spectroscopy can be achieved by enhancing understanding of the device's thermal behaviour.

Bending of a bi-material structure due to a mismatch of the thermal expansion coefficients of the constructing layers was first explored by Stoney.(9) Stoney's equation relates the radius of the curvature (r) of such a structure to Young's modulus of the substrate, as well as thicknesses of constructing layers by $r = Et_1^2/6t_2\sigma$, where, E, t_1, t_2 and σ are Young's modulus, substrate's thickness, thickness of the deposited layer, and generated surface stress, respectively.(9)

Nonetheless, Stoney's equation is not applicable to a recently developed microfluidic cantilever sensor because it does not include microfluidic parts.(10) Although bi-material microfluidic cantilever (BMC) sensors have been employed for several novel applications, a theoretical understanding of the response of such a platform to heat is still lacking.(8,11) In fact, Naresh M et al. asserted that thermal deflection of the BMC is governed by $(d^2z/dx^2) = 6(\gamma_1 - \gamma_2)(t_1 + t_2/t_2^2 K)[T(x) - T_0]$. However, this relation does not include existence of a microfluidic channel on the cantilever and results in considerable error in the thermal sensitivity of the device.(12) The large difference between theoretical and experimental results highlights the need for a new model to explain the thermal sensitivity of BMCs. Here, adapting the approach developed by Timoshenko S,(13)

bending of a BMC resulted from thermally induced surface stresses is modeled in an unprecedented way. To evaluate this new model, bending of two different microfluidic cantilevers were monitored as a function of IR radiation from 8.3 µm to 10.4 µm. The experimental results match the theoretical prediction calculated using the new model with high accuracy.

5.2.   Objective

The thermal sensitivity of a bi-material microcantilever plays a critical role when application of the device is based on heat sensing. Even though there have been extensive studies on the response of standard bi-material microcantilevers to heat, thermal sensitivity of microfluidic cantilevers has not been addressed by analytical models. BMC have introduced a novel platform to investigate intermolecular interactions through obtaining IR spectra of liquids in picoliter volume levels. However, further improvements in their applications depends on an enhanced understanding of the response of this platform to heat. In this chapter of this work, a new model applicable to the bi-material microfluidic cantilever device is presented when the device undergoes uniform heating. This model is validated by the results of photothermal bending experiments carried out on different designs of BMCs with different microfluidic channel heights of 1.6 and 3.1 µm. In addition, capability of the model to accurately predict thermal sensitivity and thermal bending of BMCs with different dimensions are presented.

5.3.   Modeling thermal sensitivity of the BMC

Here, the bending of a BMC beam subjected to uniform heating is investigated. In this work, it is assumed that the cross section of the beam is plane and perpendicular to

the beam axis and remains plane and perpendicular to the curved axis during the bending. Because of changes in the temperature, both layers of the microcantilever beam will be subjected to an axial force (F) and a bending moment (M). The axial force is either tensile or compressive. Figure 5.1 presents a schematic of BMC deflection resulting from uniform heating.
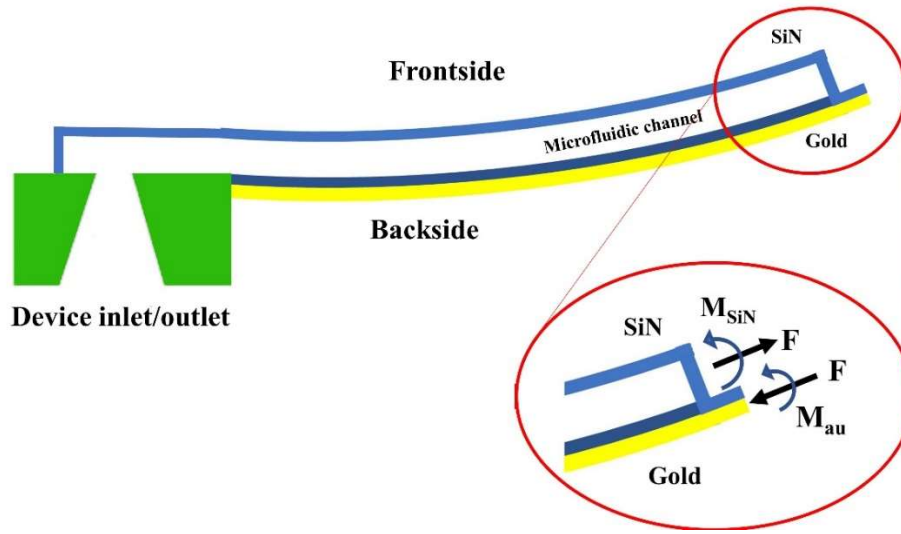
Figure 5.1. The schematic of deflection of BMC due to uniform heating. M represents the bending moment and F represents a tensile force or a compressive force. Yellow represents a secondary gold layer deposited on the backside of the microfluidic cantilever platform. Blue represents SiN layers constructing the microfluidic cantilever sensor.

On the bearing surface of gold and SiN the unit elongation in the longitudinal direction of both layers must be equal, therefore we have:

$$\gamma_{Au}(T - T_0) + \frac{F_{Au}}{E_{Au}A_{Au}} + \frac{t_{Au}}{2}\kappa = \gamma_{SiN}(T - T_0) - \frac{F_{SiN}}{E_{SiN}A_{SiN}} - \frac{t_{SiN}}{2}\kappa \qquad (5.1)$$

where, γ, T, T_0, F, E, A, t, and κ represent the thermal expansion coefficient, increased temperature, room temperature, compressive or tensile force, Young's modulus, area, thickness, and principal curvature of either the gold or the SiN layer. Vertical changes in the temperature in SiN and gold layers are neglected for simplicity. Therefore, the microfluidic channel and gold layer are only subjected to longitudinal stresses. In the absence of an external force acting on the device, the equilibrium between all the forces acting over any cross-section of the device is shown in Equation 5.2;

$$F_{Au} = F_{SiN} = F .$$ (5. 2)

In addition, the sum of the bending moment about the centroid (h_c) of the BMC is defined by Equation 5.3;

$$M_{Au} + M_{SiN} = Fh_c .$$ (5. 3)

Knowing that bending moment (M) is related to flexural rigidity (EI) and principal curvature of the beam by $M = \kappa EI$,(13) the following equation describes the force acting over the cross-section of the beam:

$$F = \frac{\kappa(E_{Au}I_{Au} + E_{SiN}I_{SiN})}{h_c} .$$ (5.4)

Using Equations 5.2 and 5.4, and solving for the principal curvature of the beam in Equation 5.1 results in:

$$\kappa = \frac{\Delta\gamma(T - T_0)}{\left(\dfrac{E_{Au}I_{Au} + E_{SiN}I_{SiN}}{h_c}\right)\left(\dfrac{1}{E_{Au}A_{Au}} + \dfrac{1}{E_{SiN}A_{SiN}}\right) + (h_c)} .$$ (5.5)

Modifying Equation 5.5 to include any initial bending of the cantilever we have:

$$\kappa + \kappa_0 = \frac{\Delta\gamma\left(T - T_0\right)}{\left(\dfrac{E_{Au}I_{Au} + E_{SiN}I_{SiN}}{h_c}\right)\left(\dfrac{1}{E_{Au}A_{Au}} + \dfrac{1}{E_{SiN}A_{SiN}}\right) + \left(h_c\right)},$$ (5.6)

where, κ_0 is the initial principal curvature of the cantilever device created during the fabrication process. Tip deflection (δ) of a microcantilever relates to the principal curvature of the device by $\delta = \left[1 - \cos(\kappa L)\right]/\kappa$.(14) Using the relation between tip deflection and principal curvature of a cantilever, Taylor series expansion of δ, and Equation 5.6, thermal sensitivity of the microfluidic cantilever device resulting from uniform heating when the temperature (T) changes from T_1 to T_2 is expressed as:

$$\frac{\Delta\delta}{\Delta T} = \frac{L^2}{2}\left[\frac{\Delta\gamma\left(1 - \dfrac{\kappa^2 L^2}{12}\right)}{\dfrac{\left(E_{Au}I_{Au} + E_{SiN}I_{SiN}\right)}{h_c}\left(\dfrac{1}{E_{Au}A_{Au}} + \dfrac{1}{E_{SiN}A_{SiN}}\right) + \left(h_c\right)}\right]$$ (5.7)

where

$$\Delta T = T_2 - T_1$$

Centroid (h_c) and area moment of inertia for the BMC should be uniquely calculated for this structure. h_c for the BMC is calculated using $h_c = \sum h_i A_i / \sum A_i$ where h_i and A_i represent the centroid and the area of the constructing layers. The following relation represents h_c for the BMC.

$$h_c = \frac{2t_c\left(h_{c-SiN} + t_{Au}\right)\left(W_c + 2h_{ch}\right) + 0.5t_{Au}^2 W_c}{2t_c\left(W_c + 2h_{ch}\right) + W_c t_{Au}}$$ (5.8)

where

$$h_{c-SiN} = t_c + \frac{W_{ch}h_{ch} + h_{ch}^2}{W_c + 2h_{ch}}.$$ (5.9)

W_c, W_{ch}, h_{ch} , and t_c represents the cantilever's width, the width of the microfluidic channel, the height of the microfluidic channel, and the cantilever's thickness. In addition, area moment of inertia of the gold layer and the microfluidic cantilever device about their centroids are defined as $I_{Au} = W_c t_{Au}^3/12$ and $I_{SiN} = 0.167\left(W_{ch}\left[(h_{ch} + 2t_c)^3 - h_{ch}^3\right] + 2t_c h_{ch}^3\right)$, respectively.

5.4. Results and discussions

5.4.1. More accurate prediction of thermal behaviours by the new model

Inadequately modeling the thermal behaviour of the BMC, with equations established for a rectangular bi-material beam, creates a considerable discrepancy between theoretical and experimental results. Accuracy of the theoretical prediction can be improved by using the new model developed in section 5.3. Here we show that the new model can more closely predict thermal sensitivity and thermal bending of the BMCs. However, use of the standard model developed for a rectangular bi-material beam(15,16) results in significant error in the estimation of the thermal behavour of the device. Hereafter the standard bi-material model will be refered to as the standard model.

Thermal sensitivity of two different BMCs, referred to as cantilevers Chip A and Chip B, was studied by Naresh M et al. The cantilever Chip A is 600 μm long and 76 μm

wide; the cantilever Chip B is 500 μm long and 44 μm wide. Their experimentally obtained values for thermal sensitivity of the cantilevers Chip A and B were reported as 250 nm/K and 195 nm/K, respectively.(12)

They assert that the thermal sensitivity of the devices is governed by,

$$(d^2z/dx^2) = 6(\gamma_1 - \gamma_2)(t_1 + t_2/t_2^2 K)[T(x) - T_0],$$

where

$$K = 4 + 6(t_1/t_2) + 4(t_1/t_2)^2 + (E_1/E_2)(t_1/t_2)^3 + (E_2/E_1)(t_2/t_1).(12)$$ In this equation, z is the vertical deflection of the cantilever at a position (x) along the length of the device, γ is the thermal expansion coefficient of the constructing layers, t is thickness of the layers, E is Young's modulus of the layers where subscripts 1 and 2 refer to the two layers. $[T(x) - T_0]$ is the temperature difference relative to ambient temperature along the length of the cantilever. If one uses $(d^2z/dx^2) = 6(\gamma_1 - \gamma_2)(t_1 + t_2/t_2^2 K)[T(x) - T_0]$, the thermal sensitivities of the microfluidic cantilevers Chip A and B are calculated as 3.5 μm/K and 2.2 μm/K, respectively.

By using this equation, Naresh M et al.(12) did not include the existence of the microfluidic channel located on top of the cantilever base. Closer inspection of their device reveals that due to neglecting the microfludic channels, they overstimated the thickness of the cantilever base from 500 nm to 1000 nm.

For comparison, we used the new model developed here to calculate the thermal sensitivity of the cantilevers Chip A and B. Since $\delta/L < 0.1$ for both devices, principal curvatures of the microcantilevers are approximated by $\kappa \approx 2\delta/L^2$ when using the new model (Equation 5.7).(17) The new model predicts the thermal sensitivity of the

cantilevers Chip A and B as 240 nm/K and 193 nm/K, respectively. These calculations match the experimentally reported value with 96% accuracy.

To calculate the cantilevers' bending, due to thermal stress, we first need to know the initial bending of the device resulting from the fabrication process. We used the information reported by Naresh et al. for bending of the cantilevers from 303 K to 324 K to extrapolate the initial bendings of -1.465 μm and -1.302 μm, respectively. The negative sign indicates downward bending of the cantilevers due to the stress created during the fabrication. Direction of the bending of a bi-material cantilever depends on stacking orientation of the layers. Because the gold layer was deposited on the backside of the device, an increase in the temperature results in an upward bending of the cantilever Chip A and B. When the temperature first increases, such an upward bending of the device will cancel out the initial downward bending. Further increases in the temperature of the device result in a net upward bending.

Here we employed both models to estimate thermal bending of the cantilever Chip A and B. Room temperature is assumed to be 296.2 K for all the calculations. Predicted results are presented in Figure 5.2. By using the new model, we predict that the cantilever Chip A and B become flat at approximately 303 K. However, using the standard model predicts that the cantilever becomes flat at a temperature of 297 K. This implies that a 0.8 K change in the temperature will cancel out the initial bending of the device. However, a 0.8 K increase in the temperature will not create a large enough stress to result in more than 1 μm bending of the device. Figure 5.2 shows that at 323 K the net bending of the Chip A and B increase linearly to 5 μm and 3.9 μm, respectively. This result closely matches the experimentally reported bending of the cantilevers Chip A and B by Naresh

M et al. (12) with 89% and 97% accuracy, respectively. Employing the standard model as utilized by Naresh M et al. to predict thermal bending of the BMCs results in the unrealistic net deflections of 92 μm and 58 μm for the cantilever Chip A and B, respectively.
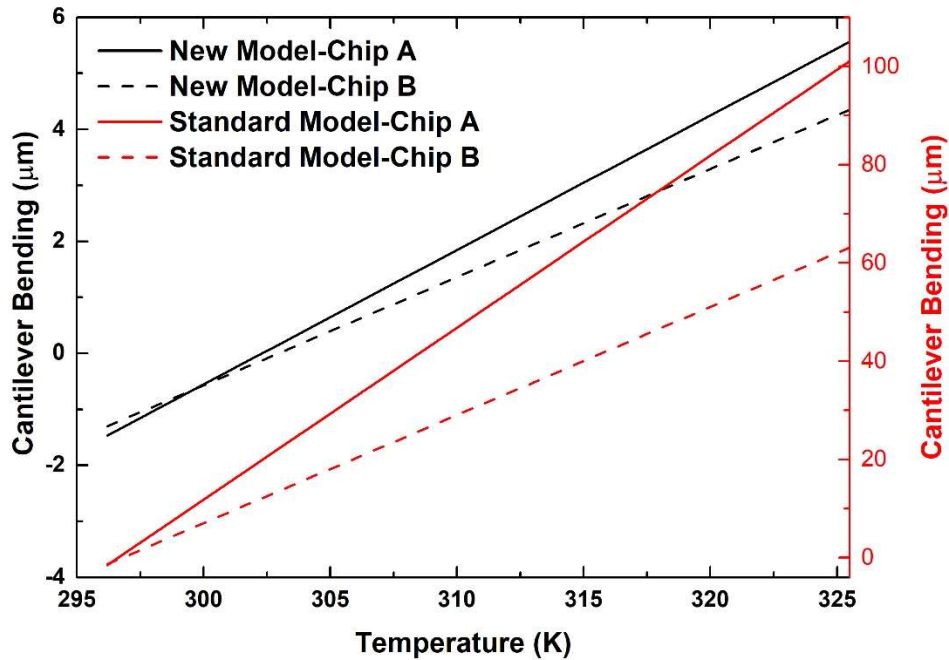
Figure 5.2. Comparison between cantilever bending predicted using the standard model and the new model developed in this chapter of the work.

5.4.2. Effect of gold thickness and the channel height

The thickness of the gold layer, as well as height of the microfluidic channel, plays a significant role on thermal sensitivity of the device and needs to be addressed. In Figure 5.3, thermal sensitivity of two BMCs as a function of gold thickness is compared using

Equation 5.7. The only difference between cantilevers 3.1 and 1.6 is the height of the microfluidic channel located on top of the cantilever. The cantilevers' dimensions required to calculate the thermal sensitivity of the devices are shown in Table 5.1. Young's modulus of SiN and gold are 180 GPa and 78 GPa, respectively. Thermal expansion coefficient of SiN and gold are $0.8 \times 10^{-6} K^{-1}$ and $14.2 \times 10^{-6} K^{-1}$, respectively.(18,19)

Table 5.1. Cantilevers' dimensions

	Cantilever length (μm) L	Cantilever width (μm) W_c	Channel width (μm) W_{ch}	Channel height (μm) h_{ch}	Channel thickness (nm) t_c
Cantilever 3.1	600	74	31.4	3.1	420
Cantilever 1.6	600	74	31.4	1.6	420
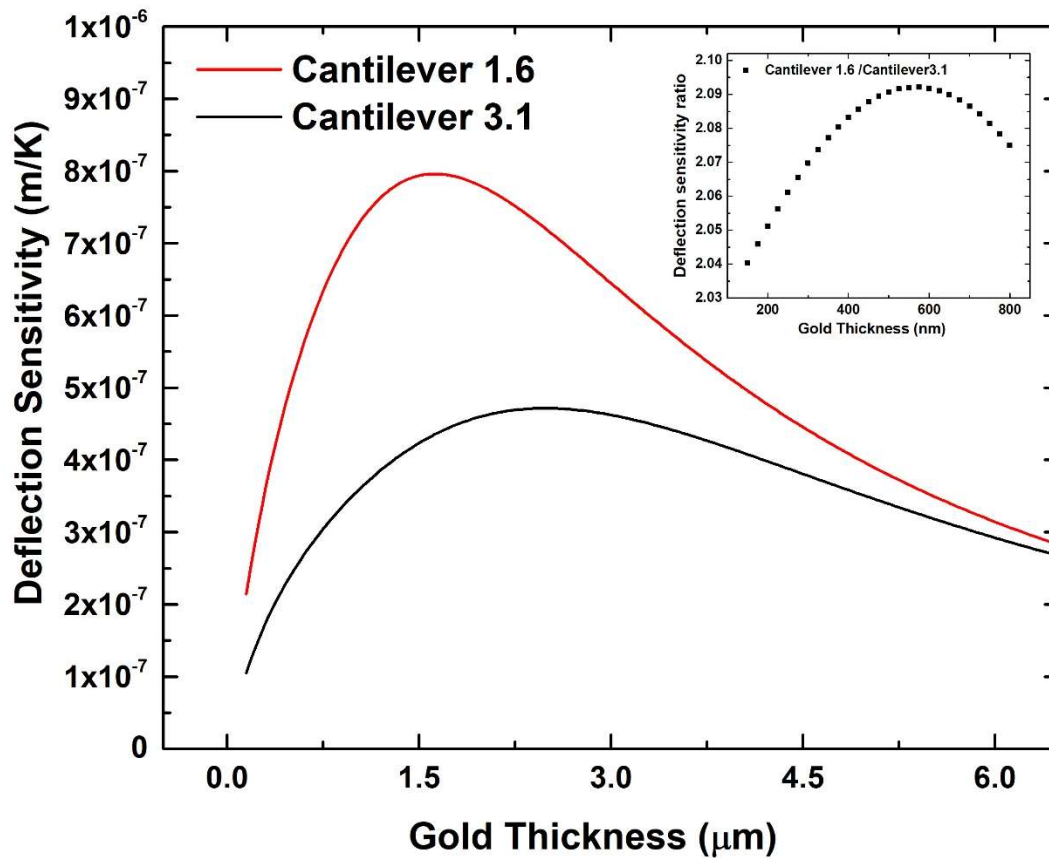
Figure 5.3. Thermal sensitivity of cantilevers 1.6 and 3.1 as a function of gold thickness. Inset graph shows the ratio of deflection sensitivity of the cantilever 1.6 to cantilever 3.1 where gold thickness varies from 150 nm to 800 nm.

The overall changes in the thermal sensitivity of the BMCs as a function of gold thickness are similar to changes in the thermal sensitivity of standard bi-material cantilevers.(20) However, as shown in Figure 5.3 the height of the microfluidic channel has a significant effect on the thermal sensitivity of the device.

To examine the effect of the channel height, two different microfluidic cantilevers with channel heights of 3.1 μm and 1.6 μm were employed. A 300 nm gold layer was deposited on the backside of both fabricated microfluidic cantilever devices. Figure 5.4

shows scanning helium ion microscope images of microfluidic cantilever 3.1 where the height of the channel is 3.1 µm.

Thermally induced bending of both BMCs was monitored by illuminating the devices with monochromatic infrared radiation using a quantum cascade laser (QCL) (Daylight Solutions). QCL is modulated at 40 Hz, using an SRS DS345 function generator, and it is in synchronization with the lock-in amplifier. The IR beam, with wavelengths varying from 8.3 µm to 10.4 µm, was focused onto the cantilevers. Employing a PSD the bending of the device was recorded by tracking the position of a laser beam reflected off of the cantilever onto the PSD. Output voltage of the PSD is proportional to the cantilever's bending. The output signal from the PSD was fed to a lock-in amplifier (SRS 850 Stanford Systems) and a spectrum analyser (SRS 760 Stanford Systems) to monitor the amplitude of bending and frequency of vibration of the device. The QCL is operating at a repetition rate of 100 kHz at a duty cycle of 5%. Figure 5.5 shows the experimental set up.
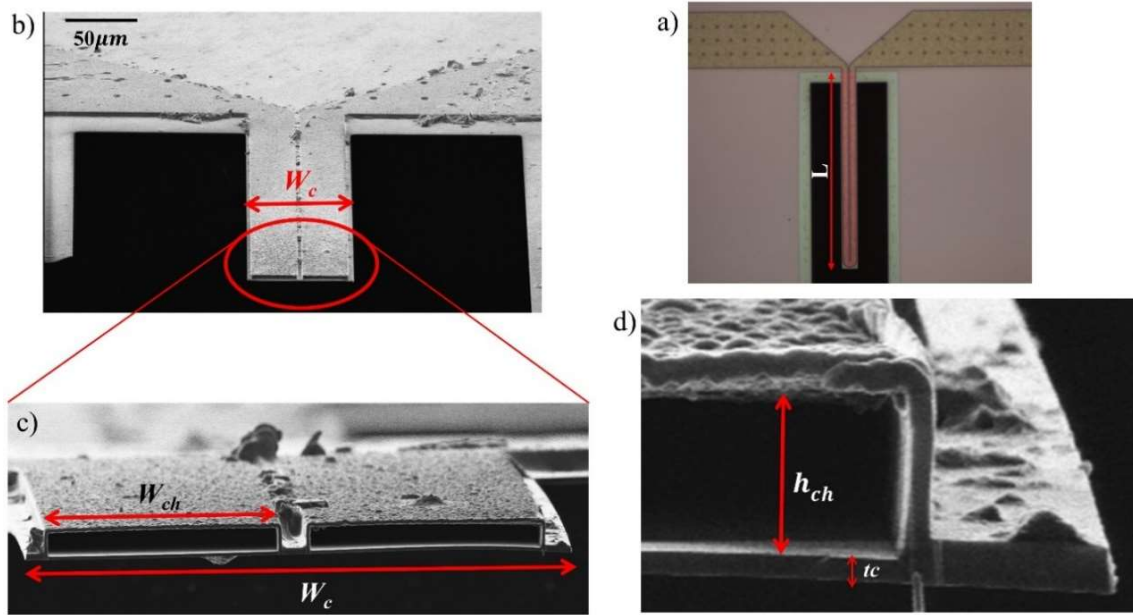
Figure 5.4. a) Microscopic image of the microfluidic cantilever 3.1, b) HIM image of the cut microfluidic cantilever 3.1, c) HIM image zoomed at the cut end of the cantilever, and d) HIM image zoomed at the right corner of the microfluidic channel. Cantilever length (L), Cantilever width (W_c), Width of the microfluidic channel (W_{ch}), height of the channel (h_{ch}), and thickness of the cantilever (t_c) are presented in Table 5.1.
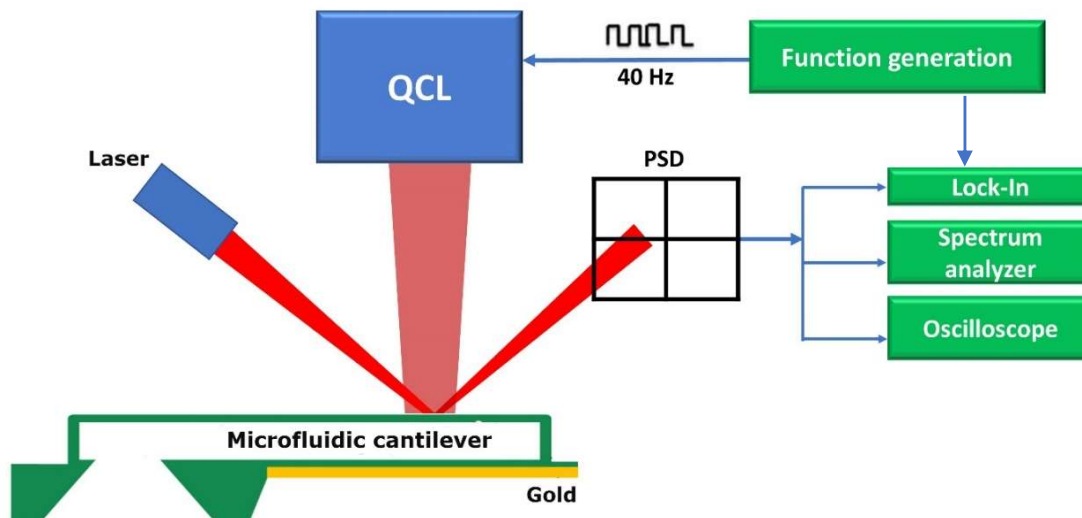
Figure 5.5. The schematic of the experimental setup. Infrared radiation was focused onto a BMC as thermal sensitivity of the device was monitored as a function of light's wavelength. This figure is not to scale.

Recorded bending of both cantilevers as a function of IR wavelength is shown in Figure 5.6. As presented in this figure, cantilever 1.6 has a higher bending amplitude than cantilever 3.1 for all wavelengths. Whereas both devices undergo the same heating conditions during the experiment, any improvement in the thermal sensitivity is attributed to the change in the channel height. Furthermore, as the goal of this chapter of the work was to demonstrate improved sensitivity, the absolute temperature of the device need not to be measured. This result is consistent with predicted results shown in Figure 5.3. At a gold thickness of 300 nm, thermal sensitivity of cantilever 1.6 is predicted to be 2.07 times higher than thermal sensitivity of cantilever 3.1. This is partially because the microfluidic channel located on top of the cantilever 1.6 base is shorter, which results in a decrease in the spring constant of the device. The lower spring constant of the cantilever results in a larger deflection due to the thermally induced stress. The maximum IR

absorptions for the constructing materials of the device is around 9.3 µm.(21,22) This is clearly reflected by the maximum photothermal bending of the devices around this wavelength.
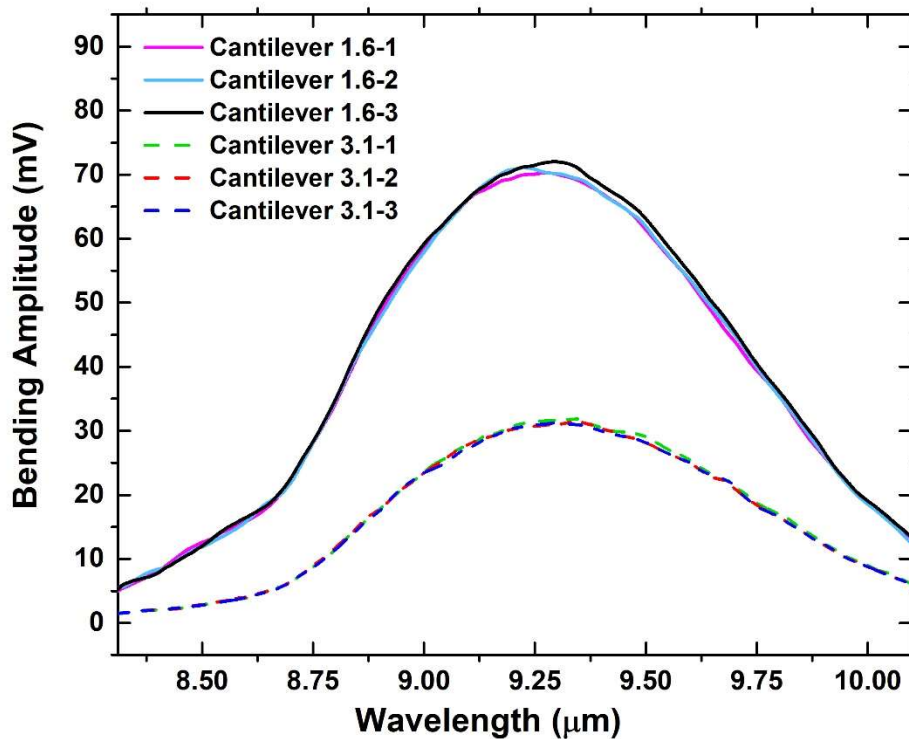

Figure 5.6. Photothermal bending of the BMC 1.6 and 3.1 as a function of IR light wavelength. Number 1,2, and 3 indicate three different measurements.
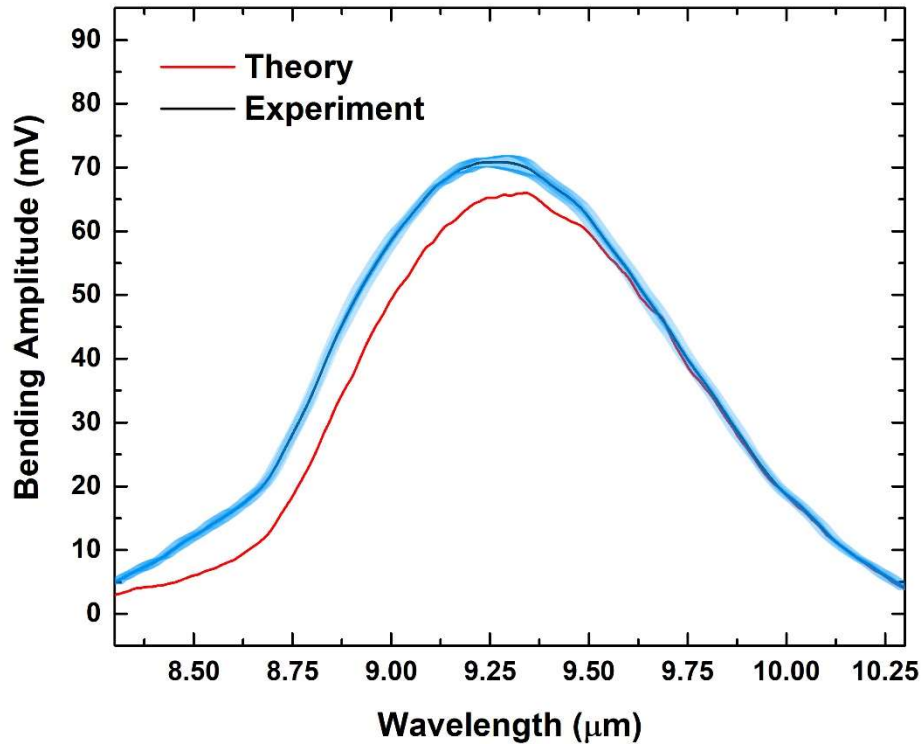
Figure 5.7. Comparison of theoretical prediction and experimental results for bending amplitude of cantilever 1.6 as a function of wavelength. Error bars are presented in blue for the experimental result.

To compare experimental and predicted results, using Equation 5.7, it is important to satisfy a uniform heating for both cantilevers. Since the QCL spot size (2.5 mm²) is much larger than the area of the microfluidic cantilever 3.1 and cantilever 1.6, it is expected that there is uniform heating. Figure 5.7 shows the comparison between experimental and predicted results for cantilever 1.6 as IR light wavelength varies from 8.3 μm to 10.4 μm. Even though the predicted result employing the developed model matches the experimental result with high accuracy, this theory can be improved further by considering temperature gradient along the length of the device.

5.5.   Material and methods

5.5.3.   Deposition of a gold layer

A 300 nm gold layer was deposited on the backside of the cantilever devices using sputtering system # 1 (Bob) in University of Alberta nanoFAB. To make the cantilever chips ready for the deposition process, they were cleaned with acetone as well as alcohol. Then, cleaned chips were located on a glass slide, using a piece of double-sided tape, in an upside-down position. Finally, glass slides were taped on a 4-inch wafer. Deposition was accomplished following the standard procedure available in the nanoFAB. A Cr adhesion layer was sputtered on the backside of the chip to enhance the adhesion of Au to SiN cantilevers.

5.6. Conclusions

It is important to improve the understanding of the response of the recently developed BMC device to heat. In this work, deflection of a BMC to the changes in temperature is studied using a new model that we developed based on the Timoshenko beam model. Prediction of the thermal bending and thermal sensitivity of the microfluidic cantilever device has been improved by at least 1000% when using this new model. The analysis presented indicates that general changes in thermal sensitivity of the device as a function of gold thickness is similar to a standard bi-material cantilever. However, cantilever 3.1, with a taller channel located on top of the device, requires a higher gold thickness to reach its maximum thermal sensitivity. In addition, decreasing the height of the microfluidic channel from 3.1 μm to 1.6 μm considerably increases the thermal sensitivity of the BMC. Such an increase in thermal sensitivity will be very useful where this platform is employed for photothermal deflection spectroscopic measurements.

5.7. References

1.   Gimzewski JK, Gerber C, Meyer E, Schlittler RR. Observation of a chemical-reaction using a micromechanical sensor. Chem Phys Lett. 1994;217(5–6):589–94.

2.   Barnes JR, Stephenson RJ, Welland ME, Gerber C, Gimzewski JK. Photothermal spectroscopy with femtojoule sensitivity using a micromechanical device. Nature. 1994;372:79–81.

3.   Canetta C, Narayanaswamy A. Sub-picowatt resolution calorimetry with a bi-material microcantilever sensor. Appl Phys Lett. 2013;102(10):103112–4.

4.   Krause AR, Van Neste C, Senesac L, Thundat T, Finot E. Trace explosive detection using photothermal deflection spectroscopy. J Appl Phys. 2008;103(9):94906.

5.   Voiculescu I, Liu F, Ono T, Toda M. Investigation of bimaterial cantilever beam for heat sensing in liquid. Sensors Actuators, A Phys. 2016;242:58–66.

6.   Li G, Burggraf LW, Baker WP. Photothermal spectroscopy using multilayer cantilever for chemical detection. Appl Phys Lett. 2000;76(9):1122–4.

7.   Burg TP, Manalis SR. Suspended microchannel resonators for biomolecular detection. Appl Phys Lett. 2003;83:2698–700.

8.   Ghoraishi MS, Hawk JE, Phani A, Khan MF, Thundat T. Clustering mechanism of ethanol- water mixtures investigated with photothermal microfluidic cantilever deflection spectroscopy. Sci Rep. 2016;(23966).

9.   Stoney GG. The tension of metallic films deposited by electrolysis. Proc R Soc London. 1909;82(553):172–5.

10. Burg TP, Godin M, Knudsen SM, Shen W, Carlson G, Foster JS, et al. Weighing of biomolecules, single cells and single nanoparticles in fluid. Nature. 2007;446(7139):1066–9.

11. Etayash H, Khan MF, Kaur K, Thundat T. Microfluidic cantilever detects bacteria and measures their susceptibility to antibiotics in small confined volumes. Nat Commun. 2016;7(12947):1–9.

12. Miriyala N, Khan MF, Thundat T. Thermomechanical behavior of a bimaterial microchannel cantilever subjected to periodic IR radiation. Sensors Actuators, B Chem. 2016;235:273–9.

13. Timoshenko S. Analysis of bi-metal thermostats. J Opt Soc Am. 1925;11(3):233–55.

14. Scott S, Kim J Il, Sadeghi F, Peroulis D. An analytical capacitance model of temperature-sensitive, large-displacement multimorph cantilevers: Numerical and experimental validation. J Microelectromechanical Syst. 2012;21(1):161–70.

15. Roark RJ, Young WC, Plunkett R. Formulas for stress and strain 5th ed. New York :McGraw-Hill; 1975.

16. Barnes JR, Stephenson RJ, Woodburn CN, O'Shea SJ, Welland ME, Rayment T, et al. A femtojoule calorimeter using micromechanical sensors. Rev Sci Instrum. 1994;65(12):3793–8.

17. Sohi AN, Nieva PM. Thermal sensitivity analysis of curved bi-material microcantilevers. J. Micromech. Microeng.2014;(115004):1-9.

18. Kwon B, Rosenberger M, Bhargava R, Cahill DG, King WP. Dynamic thermomechanical response of bimaterial microcantilevers to periodic heating by

infrared radiation. Rev Sci Instrum. 2012;83(1).

19. Toda M, Ono T, Liu F, Voiculescu I. Evaluation of bimaterial cantilever beam for heat sensing at atmospheric pressure. Rev Sci Instrum. 2010;81(55104):1–6.

20. Lai J, Perazzo T, Shi Z, Majumdar A. Optimization and performance of high-resolution micro-optomechanical thermal sensors. Sensors Actuators, A Phys. 1997;58(2):113–9.

21. Busca G, Lorenzelli V, Porcile G, Baraton MI, Quintard P, Marchand R. FT-IR study of the surface properties of silicon nitride. Mater Chem Phys. 1986;14(2):123–40.

22. Shankar SS, Rai A, Ahmad A, Sastry M. Rapid synthesis of Au, Ag, and bimetallic Au core-Ag shell nanoparticles using Neem (Azadirachta indica) leaf broth. J Colloid Interface Sci. 2004;275(2):496–502.

Chapter 6:

Actuation of microfluidic cantilever using confined electrolyte solution and alternating electric fields

6.1. Introduction

There are different methods to drive microsystems including microcantilevers such as:

1) Piezoelectric elements, which supply periodic excitations in response to the potential deference across the element.(1,2)

2) Thermal interactions, where a periodic variation in thermal characteristics is utilized to generate a time-varying thermal expansion and movement.(3)

3) Lorentz forces, where the interaction between an external magnetic field and a current on the device develops periodic forces.(4,5)

4) Feedback control, where electronic feedback circuits are employed to monitor the response of a cantilever and adjust it to control the signal accordingly.(6–8)

Among the above-mentioned methods, feedback loops in combination with an electrostatic drive electrode and piezoelectric crystals have been employed as driving mechanisms for microfluidic cantilever resonators.(9–12) To our knowledge, there has not yet been any report on actuating a microfluidic cantilever by applying AC voltage on a confined electrolyte solution. This idea can possibly be employed to design a new online actuation method in the future. This chapter seeks to explore the actuation of an

electrolyte filled microfluidic cantilever through exerting an AC potential difference to the system.

6.2.   Objectives

The major goal for this part of this study was to actuate an electrolyte filled microfluidic cantilever device by applying AC potential differences. In addition to the main objective, the effect of the following parameters in the obtained results were studied, to improve our understanding about the system.

1) Concentration of $NaHSO_4$ solution.

2) Strength of the applied AC voltage.

3) Size of the microfluidic cantilever.

4) Intrinsic charge on the device.

5) Frequency of the applied AC voltage.

6.3.   Experimental design

6.3.1.   Microfluidic device

Figure *4.1*Figure 6.1 shows microscopic images of a device employed for the work presented in this chapter. This cantilever is located on Chip 7 and is referred to as cantilever C7 throughout this chapter. The cantilever located underneath of the microfluidic channel has a thickness of 0.5 μm, a width of 44 μm, and a length of 500 μm. The microfluidic channel has a width of 16 μm and a height of 3 μm. All the

experiments were conducted with this design of the device, except for the experiments presented in section 6.4.2, where a secondary design was employed to study the effect of the device's geometry.
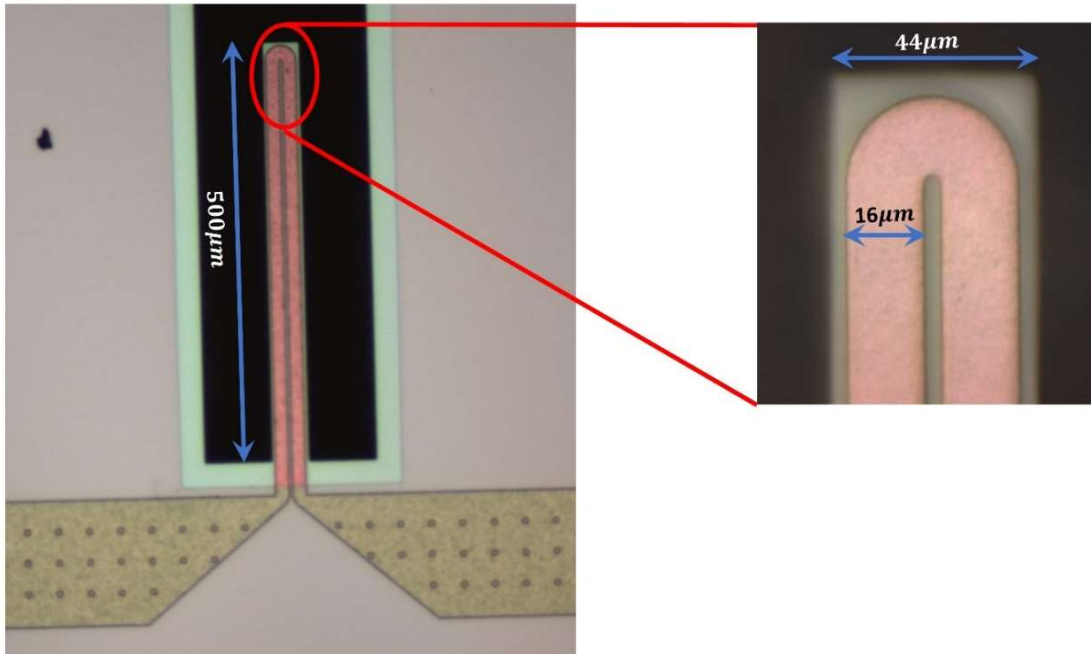

Figure 6.1. Microscopic top view of the cantilever C7, length and width of the cantilever are 500 μm and 44 μm, respectively. Width of the channel sitting on top of the cantilever is 16 μm.

6.3.2. Fluid delivery

Fluid delivery set-up is the same as the one explained in Chapter 4 with affixed Pt wires. Two Pt wires, with diameter of 0.1 mm, were inserted in the stainless-steel tubes that were embedded in the PEEK holder. The assembly is clamped onto an optical table located under a Polytec MSA-500 Laser Doppler Vibrometer (LDV).

6.3.3. Measurement set-up

A series of sinusoidal potential differences was generated using the internal function generator of the LDV and swept throughout the range of frequencies around fundamental frequency of the device. The generated potential difference was amplified using a power amplifier (Electronic Navigation Industries 2100L RF power amplifier) and then applied to the solution, using the Pt wires located beneath the input and the output of the cantilever device. Applied voltages were monitored using an oscilloscope. A non-contact current probe (Tektronix CT-2) was employed to monitor any current in the system. The schematic of the experimental set-up is shown in Figure 6.2.
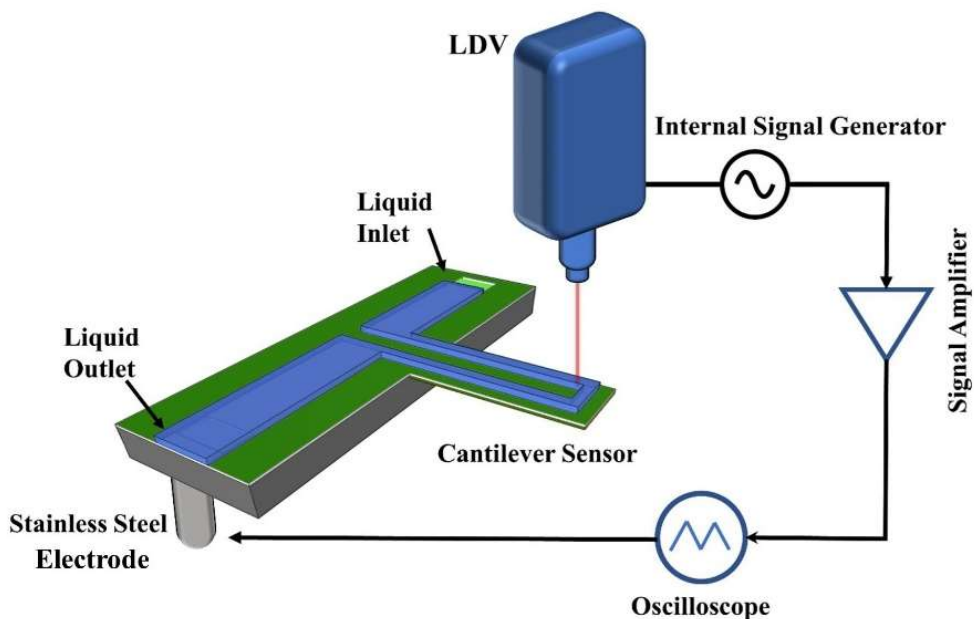

Figure 6.2. The schematic of the experimental set-up to collect the cantilever response upon applying the AC voltages.

6.3.4.　Data collection

After loading the samples, with different concentrations of electrolyte solutions in the cantilever and applying the AC potential differences, the frequency responses of the device were monitored using the LDV. For example, a measured frequency response by the LDV is shown in Figure 6.3. To be able to process the captured frequency response, the data was transferred from a PSV format to text files. Next, to obtain the processable frequency spectrum over the desired limits, the maximum amplitude of each waveform was extracted using MATLAB code. These amplitudes were then plotted with respect to the correlating frequency of the applied voltage. This resulted in the frequency spectrum shown in Figure 6.4. Finally, this spectrum was fitted by a Lorentzian function to obtain the resonance amplitude, the resonance frequency, and the quality factor. The frequency of the cantilever was monitored as an indicator of proper loading and removal of each sample. All the experiments were repeated at least five times for each voltage, and the average values of the resonance amplitudes were reported in the results and discussions section of this chapter.
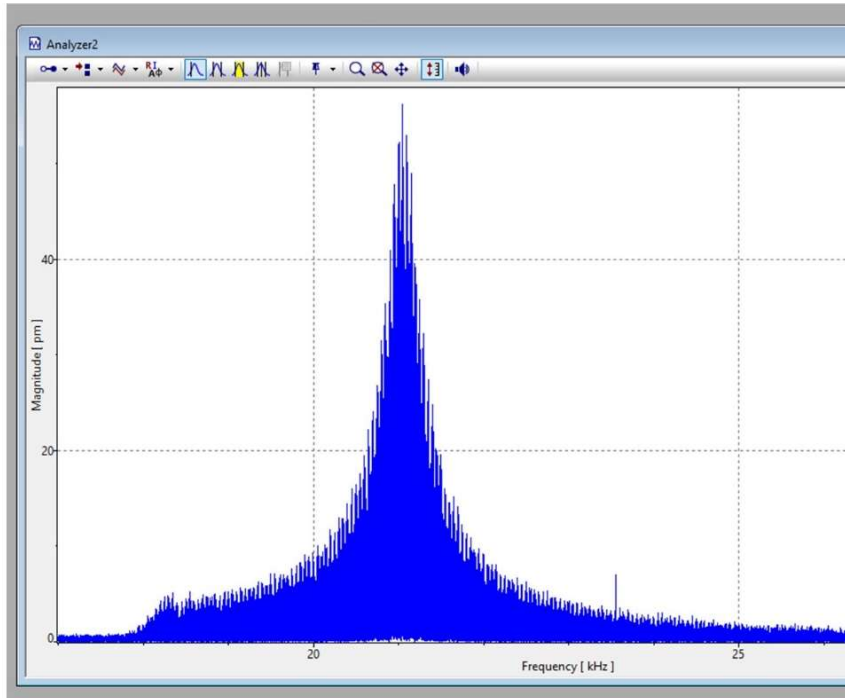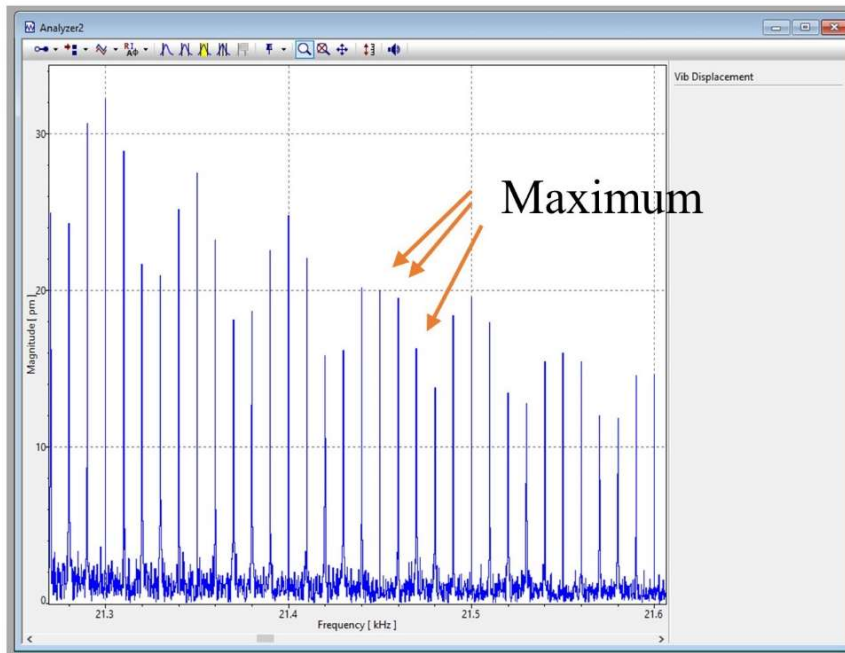
Figure 6.3. a) The frequency response of an electrolyte filled cantilever C7 as measured by the LDV upon applying AC voltages, b) the frequency response zoomed at the range of 21.3 kHz to 21.6 kHz. As an example, the maximum points of three peaks are marked with orange arrows.
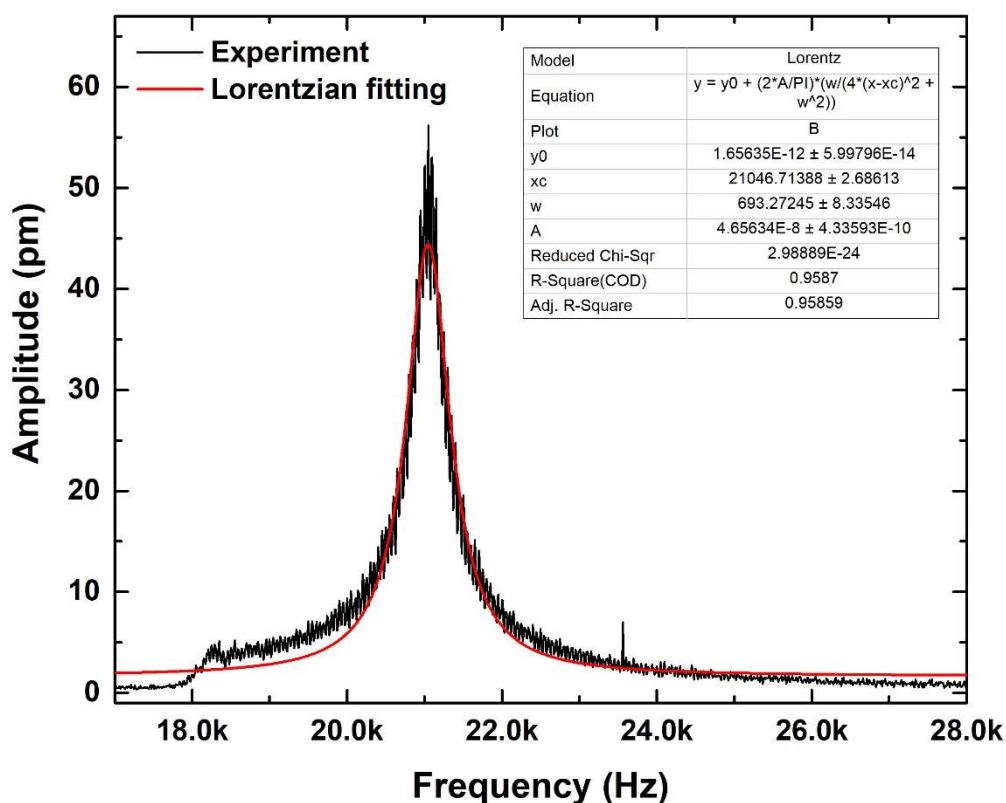
Figure 6.4. The frequency response of the electrolyte filled cantilever C7 obtained after extracting the maximums of all the peaks shown in Figure 6.3.

6.4. Results and discussions

6.4.1. Effect of concentration

In this section of the work, an electrolyte filled cantilever C7 was exposed to AC potential differences and the device response was studied. $NaHSO_4$ solution with concentrations of 1 wt%, 2.5 wt%, 10 wt%, and 20 wt% were used for this study. As an AC voltage was applied to the Pt electrodes, an electric field formed between them which caused a current to pass through the electrolyte solutions. In addition, there would be an

external electric field forming between the stainless steel electrodes. Therefore, the cantilever beam as well as the confined electrolyte both experience an external electric field. Interaction of the field with the electrolyte filled cantilever actuates the device. The resulting resonance amplitude of the device is shown in Figure 6.5.

As Figure 6.5 shows, the resonance amplitude of the cantilever varies as a function of the applied voltage and concentration of the electrolyte. An increased amplitude as a function of voltage can be attributed to a stronger external electric field that is interacting with the electrolyte filled device. However, the effect of concentration on the amplitude is more complicated, because any variations in concentration changes conductivity, dielectric constant, and pH of the solution.(13,14) For all the concentrations except 10 wt% $NaHSO_4$, the increase in the resonance amplitude is a linear function of the voltage. For 1 wt% solution, the amplitude is 2.4 times larger when the voltage is changed from 0 V to 150 V. The rate of amplification becomes four times higher at 2.5 wt% $NaHSO_4$. However, at 10 wt% concentration the amplitude shows a square dependency on the voltage resulting in the highest resonance amplitude. Finally, at 20 wt% $NaHSO_4$ the linear increase in the amplitude is almost the same as 1 wt% solution. Whereas, the conductivity of $NaHSO_4$ solution increases by concentration, the pH and dielectric constant decreases.(13–15) These opposing trends might have a role in the complicated cantilever response to the changes in the concentration. In addition, in a higher concentration of the electrolyte, there might be considerable joule heating resulted from a higher conductivity of the solution.(16,17) This heat can possibly affect the behaviour of the system.
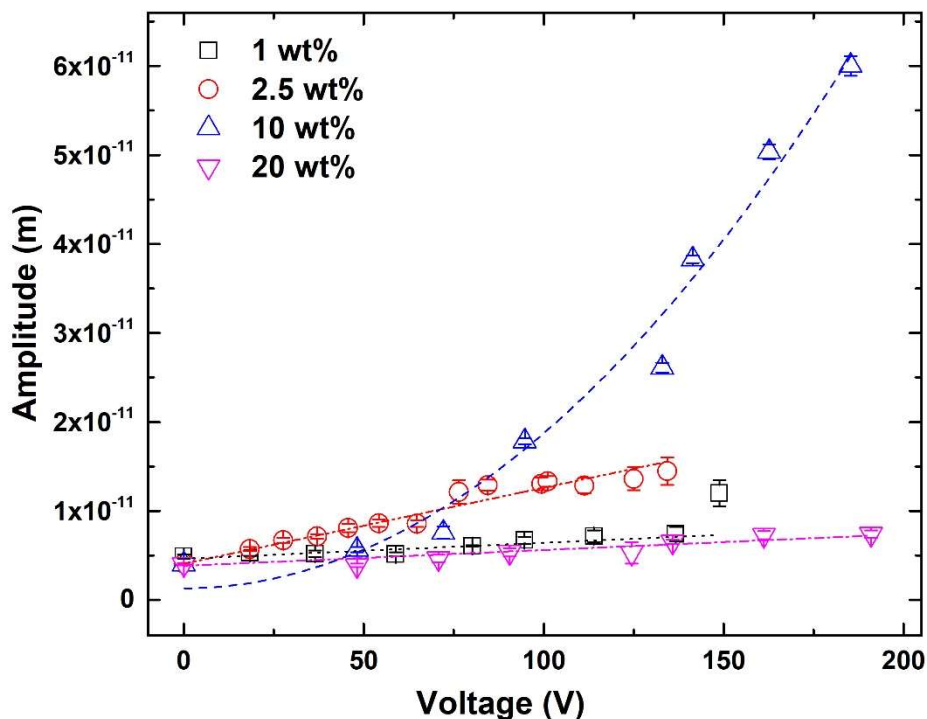
Figure 6.5. Effect of voltage and concentration of NaHSO$_4$ on the resonance amplitude of cantilever C7. For 10 wt% NaHSO$_4$ the amplitude shows a square dependency on the voltage (amplitude=1.3+1.7V^2) with R^2=0.98. For 1 wt%, 2.5 wt%, and 20 wt% NaHSO$_4$ the amplitude is a linear function of the voltage with R^2 of 0.70, 0.98, and 0.87, respectively.

The surface charges of the device's interior surface can vary as a result of changes in the pH of the solution.(18) The possible effects of the pH-dependent surface charge on the resonance amplitude can be studied by employing an electrolyte such as NaCl, because the pH of the solution is independent of the concentration and always remains 7. Figure 6.6 compares the resonance amplitude of cantilever C7 filled with 10 wt% and 15 wt% NaCl. Although the pH of the solution is the same for both concentrations, the

resonance amplitudes varies from 10 wt% to 15 wt% NaCl. In addition, for 10 wt% NaCl the increase in the amplitude is a linear function of voltage; however, for 15 wt% the amplitude shows square dependency on the voltage. This result indicates that the system's response is not pH dominant and it depends more on the solution concentration and conductivity. However, more study needs to be conducted to be able to model the exact behaviour of this system as a function of an electrolyte concentration.
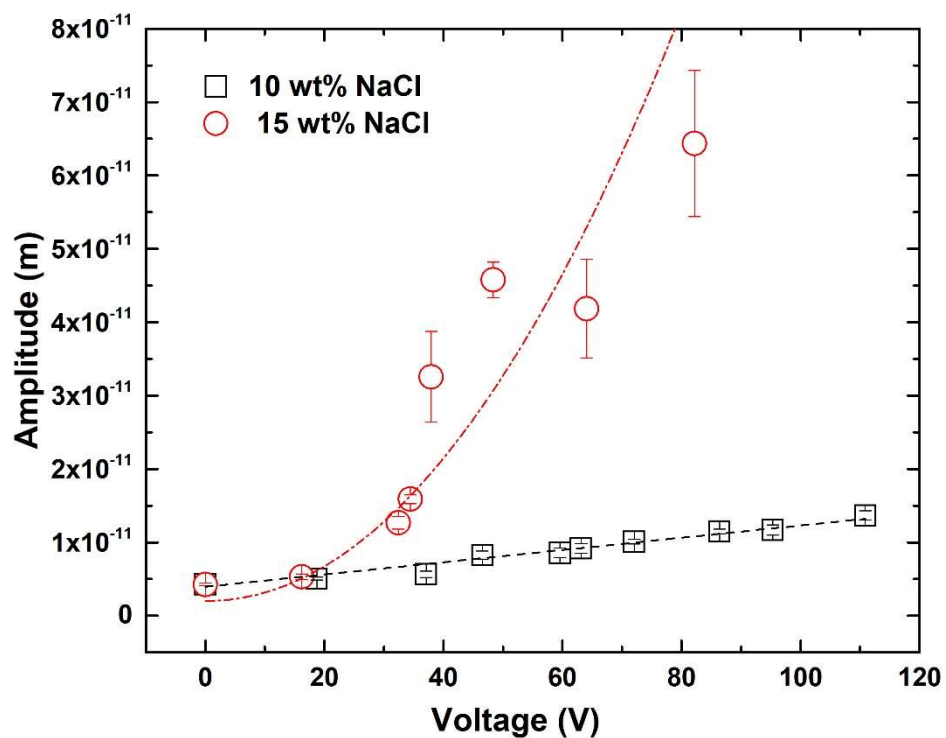

Figure 6.6. Resonance amplitude of 10 wt% and 15 wt% NaCl filled cantilever C7 with respect to the AC voltage.

6.4.2.   Effect of device's geometry

To improve our understanding about the behaviour of the system, here we present the results obtained when a microfluidic cantilever with a smaller channel size is employed to conduct the same experiment. This microfluidic cantilever is located on Chip 12 (see Figure A11 in appendix A for the device layout) and hereafter is referred to as cantilever C12. Cantilever C12 is 100 μm long and the microfluidic channel on this device has a height and width of 3 μm and 4 μm, respectively. The resonance frequency of this device is 406 kHz. The experimental conditions were the same as the ones applied to cantilever C7, for 10 wt% NaHSO$_4$, except for the frequency of AC potential difference which was changed to match the frequency of cantilever C12. Figure 6.7 compares the resonance amplitude of cantilever C12 and C7 at different voltages. This result indicates that the resonance amplitude of cantilever C12 is a linear function of the applied potential difference with a higher sensitivity than cantilever C7. The sensitivity is defined as the ratio of change of resonance amplitude to the change of voltage. The higher sensitivity of cantilever C12 to the applied voltage resulted from the multiple effects of changing the device dimensions as explained in the following.

Cantilever C12 has a higher spring constant and quality factor. Increased quality factor is a result of lower internal and external damping of cantilever C12. However, an increase in the spring constant is created because of changing the geometry. The spring constant of a cantilever (k) is defined by $k = 3EI/l^3$,(19,20) where E, I, and l are Young's modulus, area moment of inertia, and length, respectively. Both the area moment of inertia and the length of cantilever C12 are smaller than cantilever C7. Whereas the decrease in the area moment of inertia and the length have competing effects on the spring

constant; any decrease in length results in a much higher increase in k, since k is proportional to l^{-3}.

In addition to the k and the quality factor, the total mass (i.e., mass of device and confined liquid) vary due to changing the geometry. The microfluidic channel located on top of cantilever C12 has an approximate volume of $2.4 \times 10^{-15} m^3$, whereas the microfluidic channel located on top of cantilever C7 has an approximate volume of $48 \times 10^{-15} m^3$. Thus, cantilever C7 confines 20 times higher volume of a liquid sample than cantilever C12. The device mass is negligible compared to the mass of the confined liquid, thus the total mass of cantilever C7 is approximately 20 times the total mass of cantilever C12. The lower total mass, the higher Q-factor, and the higher spring constant are possible reasons for the higher sensitivity of cantilever C12.
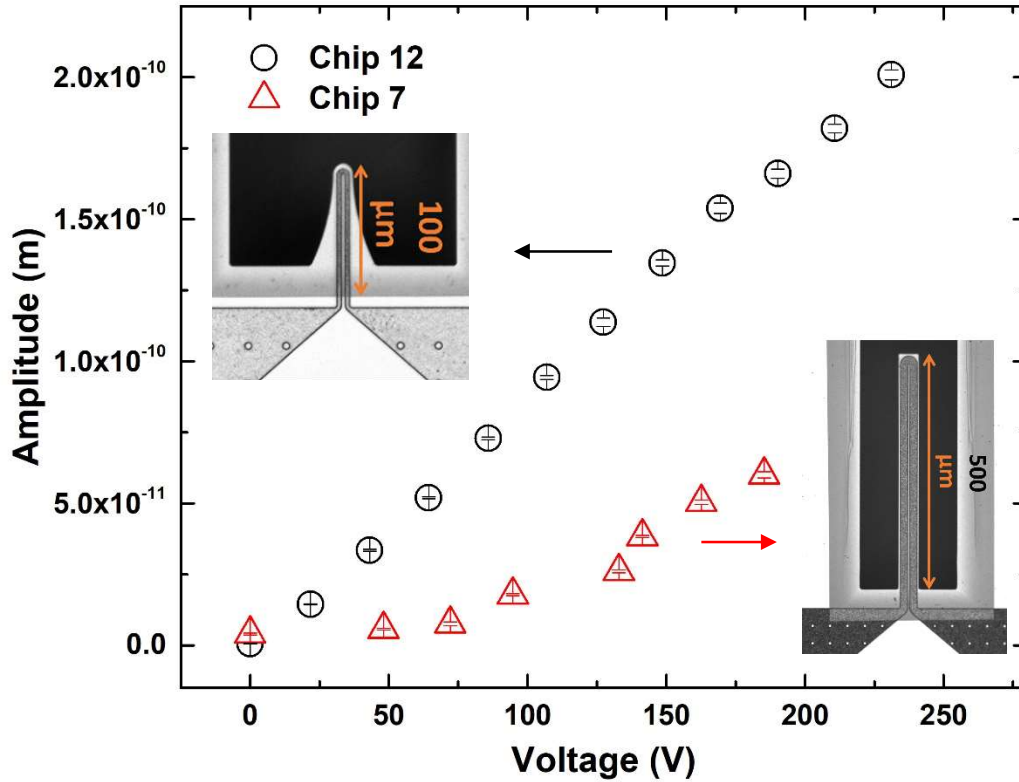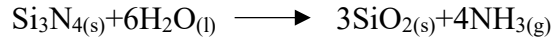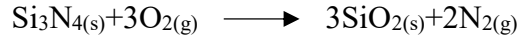
Figure 6.7. The resonance amplitude of cantilever C12 and C7 as a function of the applied voltage. Both cantilevers were filled with 10 wt% $NaHSO_4$. The images of cantilever C12 and C7 are not on the same scale.

6.4.3. Initial surface charge

Here, the effect of the interaction of the electric field with an intrinsic surface charge of the device is discussed. Even though silicon nitride thin films are cited as chemically stable, the near surface $Si-N$ bond in this thin film is chemically reactive. When $Si-N$ is exposed to air or water, it develops a surface passivation layer with a thickness of 3-5

nm. This layer results from silicon nitride oxidation in oxygen or water vapor. Oxidation reactions are thermodynamically feasible at room temperature and these reactions are represented by the following equations:

$$Si_3N_{4(s)} + 3O_{2(g)} \longrightarrow 3SiO_{2(s)} + 2N_{2(g)}$$

$$Si_3N_{4(s)} + 6H_2O_{(l)} \longrightarrow 3SiO_{2(s)} + 4NH_{3(g)}$$

However, these equations do not capture the complete complex surface chemistry of Si_3N_4, which results from the presence of $Si\text{-}N$, $Si\text{-}N\text{-}O$, and $Si\text{-}O$ bonds in the near-surface region. Reactions of $Si\text{-}N$ bonds when exposed to air or moisture result in the formation of charged and neutral functional groups (i.e., $Si-NH_3^+$, $Si\text{-}OH_2^+$, $Si\text{-}O^-$, $Si\text{-}NH_2$, and $Si\text{-}OH$).[18,21,22] To demonstrate the effect of any surface charges, resulting from the aforementioned functional group, an empty and water filled cantilever C7 were examined under the same conditions as an electrolyte filled cantilever. The frequency response of an empty cantilever C7, upon applying different voltages, is shown in Figure 6.8.
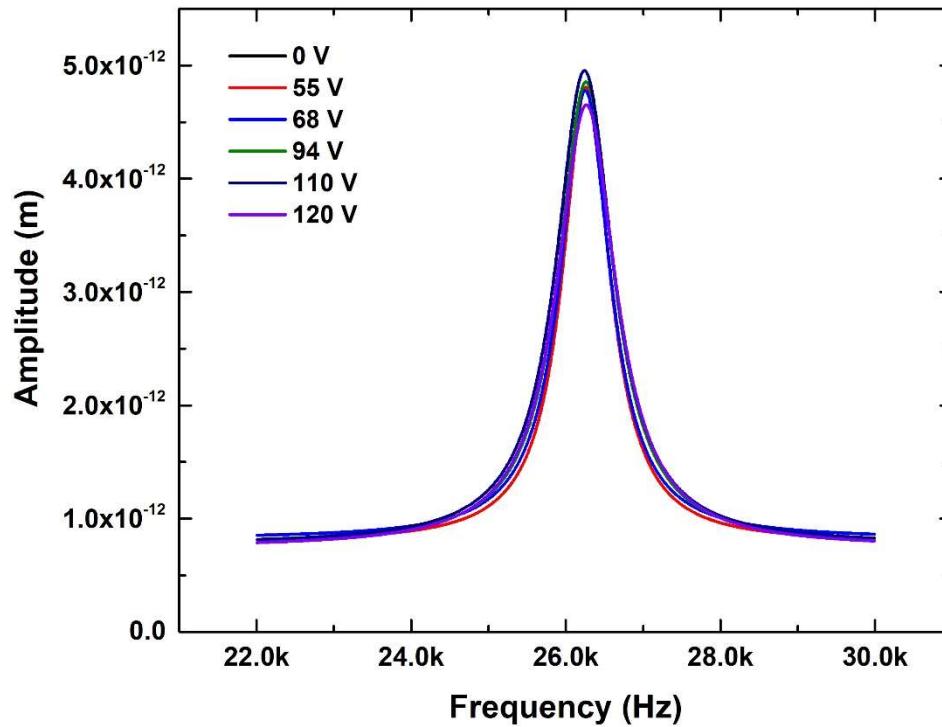
Figure 6.8. The frequency response of an empty cantilever C7 upon applying different voltages. The frequency responses of the device were fitted by a Lorentzian function.

This experiment was repeated five times for each voltage and the resonance amplitude was obtained after fitting the device frequency responses by a Lorentzian function. Figure 6.9 shows changes in the averaged amplitude as a function of applied AC voltage.
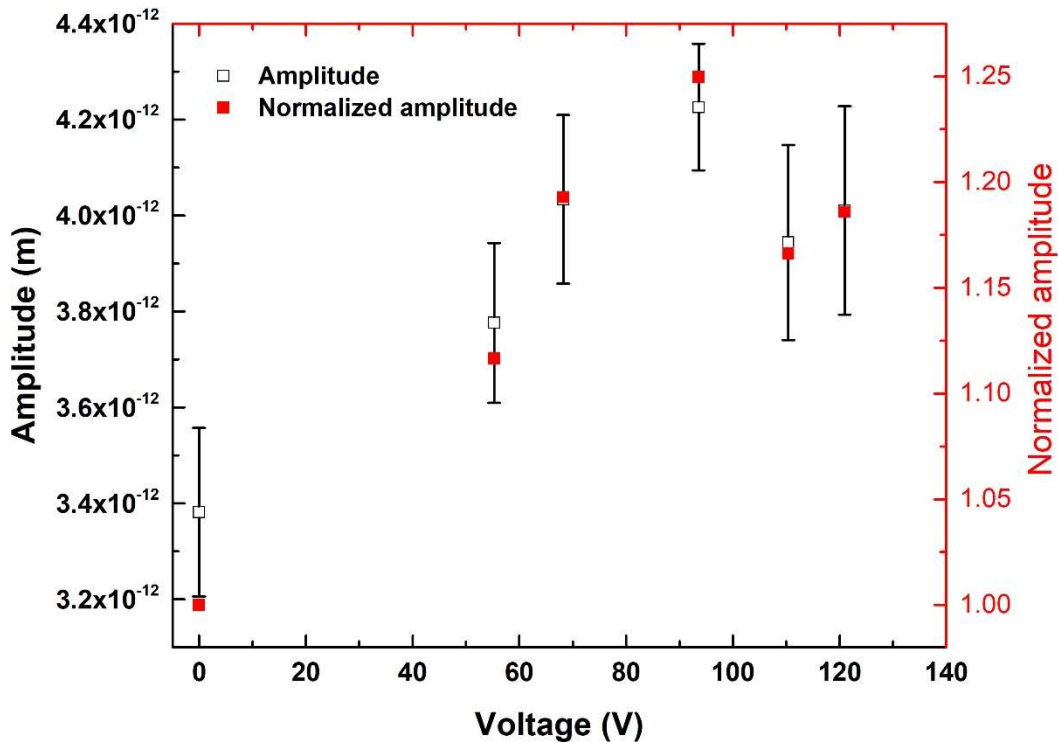
Figure 6.9. Changes in the average resonance amplitude of an empty cantilever C7 as a function of AC voltage.

Figure 6.9 indicates that the cantilever surface charge does not result in a considerable increase in the cantilever's amplitude at the applied voltages. The same experiment was carried out with the water filled cantilever and the frequency responses of the device at different voltages are shown in Figure 6.10. This experiment was also repeated five times for each voltage. Figure 6.11 shows changes in the average amplitude of the water filled cantilever C7 as a function of voltage. This figure indicates that there were no changes, beyond the standard deviations, in the resonance amplitude of the water filled cantilever upon applying the voltage. Results obtained with the empty and water filled cantilevers indicated that the presence of intrinsic surface charges on the device

would not result in noticeable changes in the resonance amplitude as the cantilever interacted with the electric field.
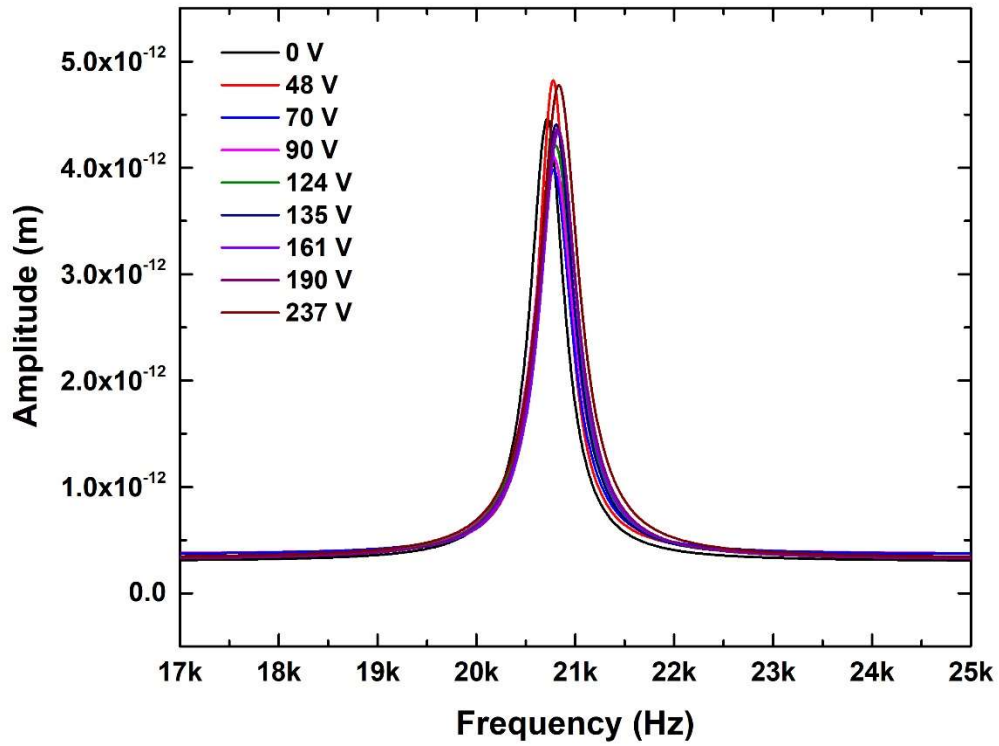

Figure 6.10. Frequency response of the water filled cantilever C7 as a function of applied voltage. The frequency responses of the device were fitted by a Lorentzian function.
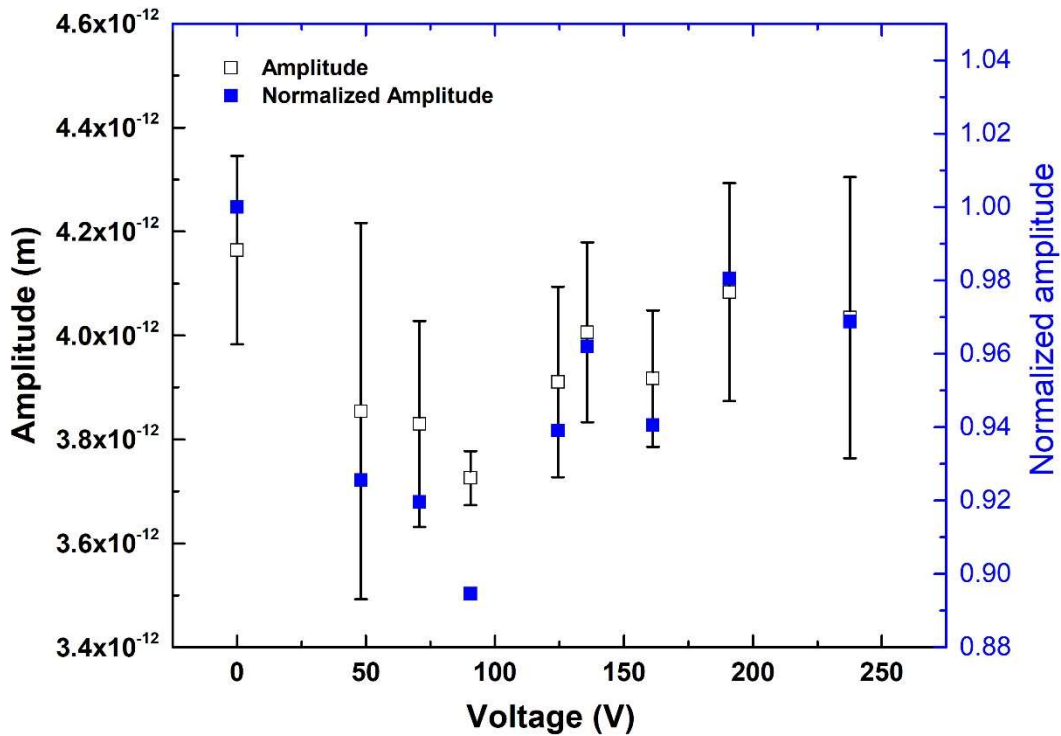
Figure 6.11. Changes in the average resonance amplitude of the water filled cantilever C7 as a function of voltage.

6.4.4.   Applied frequency

This section seeks to explore the effect of the frequency of an AC voltage on the device response. Here a cantilever C7 was filled with 5 wt% of $NaHSO_4$ solution. As the cantilever's amplitude was monitored, the AC voltage of 45 V with different frequencies was applied to the system. This cantilever had a fundamental frequency of 20.9 kHz. Thus, a center frequency of 20.9 kHz, 41.8 kHz, and 62.7 kHz was used as the center sweep frequencies. Figure 6.12 shows that to actuate the cantilever, the frequency of the AC voltage should match the fundamental frequency of the device. In other words, when

160

the frequency of the applied voltage is outside the fundamental frequency of the cantilever, the amplitude returns to that of the unexcited cantilever.
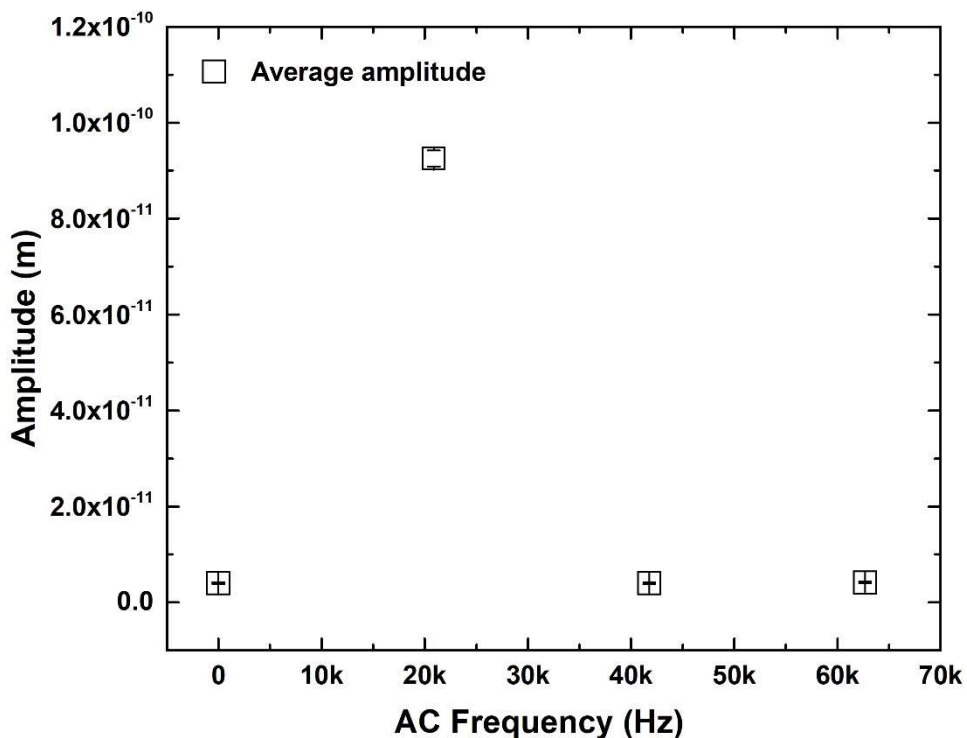

Figure 6.12. The effect of the frequency of the AC voltage on the resonance amplitude of the cantilever C7, filled with 5 wt% of $NaHSO_4$ solution.

6.5. Material and methods

6.5.1. Chemical

Water used in all the experiments was milli-Q water (purified using Milli-Q Advantage A10). Sodium bisulfate and sodium chloride were purchased from Sigma-Aldrich.

6.5.2. Equivalent circuit

Linear characteristics of current and voltage (shown in Figure 6.13) indicates the linear resistance of this system. This linearity can possibly be modeled by resistors and capacitors. One way to model the system is shown in Figure 6.14, where C_{dl}, R_f, C_e, and R_s represent the double-layer capacitance (formed between Pt electrode and electrolyte), the faradaic resistance, the external capacitance (formed between the stainless steel electrodes), and the solution resistance, respectively. However, at this stage of the study we cannot precisely define the exact contribution of each element in the final results.
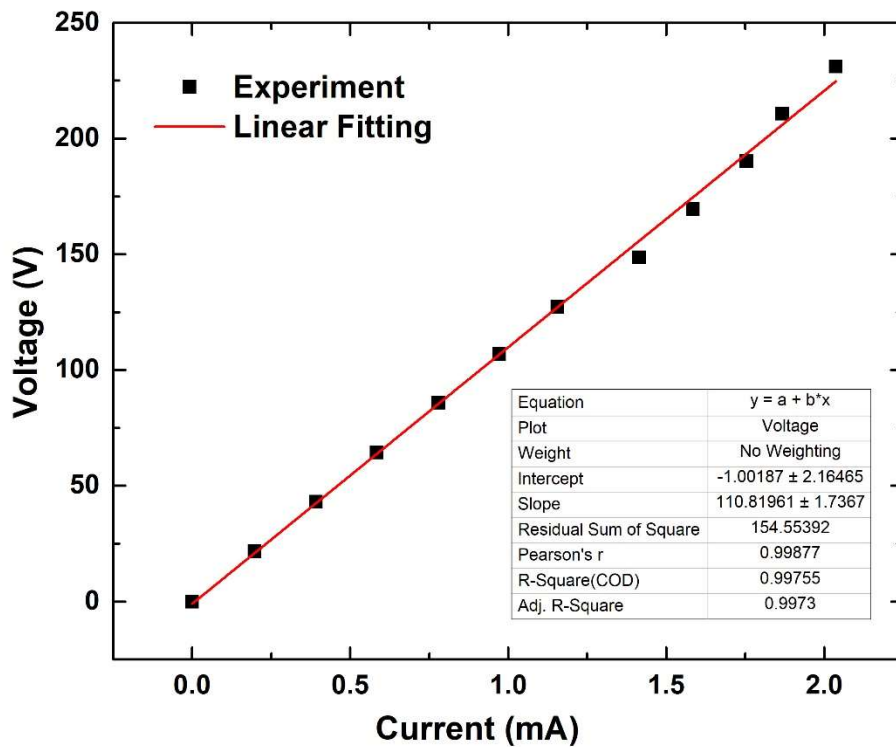

Equation	y = a + b*x
Plot	Voltage
Weight	No Weighting
Intercept	-1.00187 ± 2.16465
Slope	110.81961 ± 1.7367
Residual Sum of Square	154.55392
Pearson's r	0.99877
R-Square(COD)	0.99755
Adj. R-Square	0.9973

Figure 6.13. Voltage-current relation for the experiment conducted with Chip 12, where the device was filled with 10 wt% $NaHSO_4$.
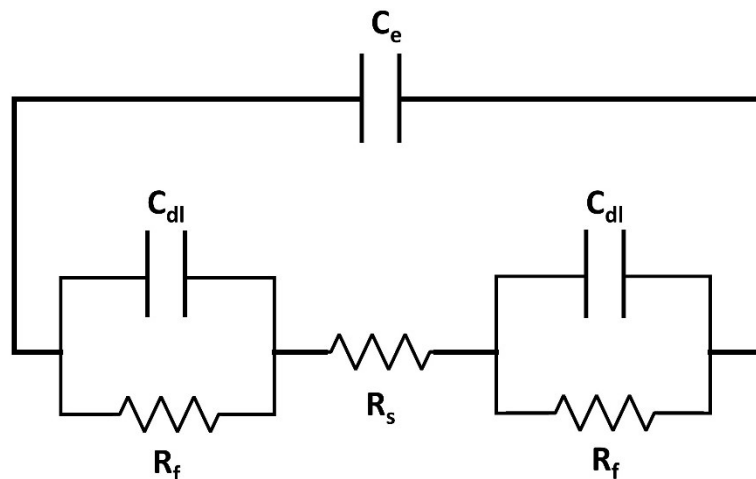
Figure 6.14. Equivalent circuit for the experimental set-up. C_{dl}, R_f, C_e, and R_s represent the double-layer capacitance, the faradaic resistance, the external capacitance formed between the stainless steel electrodes, and the solution resistance, respectively

6.6. Conclusion

In this chapter, nanograms of $NaHSO_4$ and NaCl solutions in combination with an AC potential difference were used to actuate microfluidic cantilevers. Presented results indicate that the resonance amplitude increases by increasing the applied voltage. However, an increase in the concentration of the electrolyte does not necessarily result in an increase in the amplitude. In addition, the intrinsic surface charges or any variation in the surface charge, resulted from changes in the solution pH, does not seem to have a considerable effect on the resonance amplitude. Nonetheless, decreasing the device's size, which in turn increases the spring constant, results in a higher resonance amplitude when 10 wt% $NaHSO_4$ was employed. Though the current system is adequate for proof of concept, further investigation is required to thoroughly understand the effect of voltage and electrolyte concentration on the response of electrolyte filled microfluidic cantilevers.

6.7.   References

1.   Yie Z, Miller NJ, Shaw SW, Turner KL. Parametric amplification in a resonant sensing array. J Micromechanics Microengineering. 2012;22(3).

2.   Thomas O, Mathieu F, Mansfield W, Huang C, Trolier-Mckinstry S, Nicu L. Efficient parametric amplification in micro-resonators with integrated piezoelectric actuation and sensing capabilities. Appl Phys Lett. 2013;102(16).

3.   Evans DR, Tayati P, An H, Lam PK, Craig VSJ, Senden TJ. Laser actuation of cantilevers for picometre amplitude dynamic force microscopy. Sci Rep. 2014;4:5567.

4.   Requa M V., Turner KL. Electromechanically driven and sensed parametric resonance in silicon microcantilevers. Appl Phys Lett. 2006;88(26):1–4.

5.   Karabalin RB, Feng XL, Roukes ML. Parametric nanomehanical amplification at very high frequency. Nano Lett. 2009;9(9):3116–23.

6.   Manzaneque T, Hernando-Garcia J, Ababneh A, Schwarz P, Seidel H, Schmid U, et al. Quality-factor amplification in piezoelectric MEMS resonators applying an all-electrical feedback loop. J Micromechanics Microengineering. 2011;21(2).

7.   Moreno-Moreno M, Raman A, Gomez-Herrero J, Reifenberger R. Parametric resonance based scanning probe microscopy. Appl Phys Lett. 2006;88(19):193108.

8.   Tamayo J, Humphris ADL, Owen RJ, Miles MJ. High-Q dynamic force microscopy in liquid and its application to living cells. Biophys J. 2001;81(1):526–37.

9.   Lee J, Shen W, Payer K, Burg TP, Manalis SR. Toward attogram mass

measurements in solution with suspended nanochannel resonators. Nano Lett. 2010 Jul 14;10(7):2537–42.

10. Burg TP, Manalis SR. Suspended microchannel resonators for biomolecular detection. Appl Phys Lett. 2003;83:2698–700.

11. Khan MF, Schmid S, Larsen PE, Davis ZJ, Yan W, Stenby EH, et al. Online measurement of mass density and viscosity of pL fluid samples with suspended microchannel resonator. Sensors Actuators, B Chem. 2013;185:456–61.

12. Lee J, Chunara R, Shen W, Payer K, Babcock K, Burg TP, et al. Suspended microchannel resonators with piezoresistive sensors. Lab Chip. 2011;11(4):645–51.

13. Gavish N, Promislow K. Dependence of the dielectric constant of electrolyte solutions on ionic concentration: A microfield approach. Phys Rev E. 2016;94(1):1–7.

14. Valisko M, Boda D. The effect of concentration- and temperature-dependent deielectric constant on the activity coefficient of NaCl electrolyte solutions. J Chem Phys. 2014;140(234508).

15. Wang P, Anderko A. Computation of dielectric constants of solvent mixtures and electrolyte solutions. Fluid Phase Equilib. 2001;186(1–2):103–22.

16. Xuan X. Joule heating in electrokinetic flow. Electrophoresis. 2008;29(1):33–43.

17. Jing D, Pan Y, Wang X. Joule heating, viscous dissipation and convective heat transfer of pressure-driven flow in a microchannel with surface charge-dependent slip. Int J Heat Mass Transf. 2017;108:1305–13.

18. Jan D, Raghavan S. Electrokinetic characteristics of nitride wafers in aqueous

solutions and their impact on particulate deposition. J Electrochem Soc. 1994;141(9):2465–9.

19.   Fernando S, Austin M, Chaffey J. Improved cantilever profiles for sensor elements. J Phys D Appl Phys. 2007;40:7652–5.

20.   Liu Y, Wang H, Qin H, Zhao W, Wang P. Geometry and profile modification of microcantilevers for sensitivity enhancement in sensing applications. 2017;29(6):689–98.

21.   Bock RM, McEntire BJ, Bal BS, Rahaman MN, Boffelli M, Pezzotti G. Surface modulation of silicon nitride ceramics for orthopaedic applications. Acta Biomater. 2015;26:318–30.

22.   S. I. Raider, R. Flitsch, J. A. Aboaf WAP. Surface oxidation of silicon nitride films. J Electrochem Soc. 1976;123(4):560–5.

Chapter 7:

Conclusions and future work

7.1. Conclusions

The main conclusions of the work described in this thesis are summarized in the following:

- Successful fabrication of the microfluidic cantilever devices with quite a few different lengths and widths was achieved while employing surface microfabrication on 350 μm thick silicon wafers. Depending on the dimensions of the device, confining one picolitre to hundreds of picolitres (300 pL) of a liquid sample inside the device is achievable.

- The deflection of the modified cantilever as a function of temperature was measured as the device was heated using a hot plate. The deflection of the BMC is linearly proportional to the changes in the temperature. This result is consistent with the linear deflection of a rectangular bi-material cantilever as a function of temperature. In addition, the fabricated microfluid cantilevers were used to demonstrate: a) the device's performance upon filling the cantilever with a liquid sample, and b) the change in the quality factors and the resonance frequencies resulting from changing the cantilever's geometry.

- IR spectra of the confined ethanol-water samples with various ethanol concentrations were collected using the photothermal cantilever deflection technique.

- The effects of ethanol concentration on the absorption peaks related to C-C-O was investigated by using micromechanical calorimetric spectroscopy to collect IR spectra of the ethanol-water mixtures. This technique offers a means to study and understand dipole dependency of molecular vibrations in confined picolitre volumes of mixtures, previously unexplored due to the limitations of volume levels in other analytical techniques. In addition, non-linear changes in the IR absorption intensity, at a fixed wavenumber, can be related to the effects of clustering in the $\partial\mu/\partial x$ which cannot be explained by Beer -Lambert's Law.

- Deflection of a bi-material microfluidic cantilever due to changes in temperature was studied using a new model developed based on the Timoshenko beam model.

- The new model improves predictions of the thermal bending and thermal sensitivity of the microfluidic cantilever device by at least 1000%.

- Decreasing the height of the microfluidic channel from 3.1 to 1.6 μm considerably increases the thermal sensitivity of the BMC. Such an increase in the thermal sensitivity will be very useful if this platform is employed for photothermal deflection spectroscopic measurements.

- Picolitres of $NaHSO_4$ and NaCl aqueous solutions in combination with an AC potential difference were used to actuate microfluidic cantilevers. In addition, the effect of the voltage, the electrolyte concentration, the device's geometry, and the frequency of an applied voltage on the device's resonance amplitude was studied and the following results were obtained.

- An increase in the applied AC voltage results in the increased resonance amplitude.

169

- An increase in the concentration of the electrolyte does not necessarily result in an increase in the amplitude.

- Decreasing the device's size, which in turn increases the spring constant, results in a higher resonance amplitude when 10 wt% $NaHSO_4$ is employed.

- To actuate the device, the frequency of the applied AC voltage must match the resonance frequency of the cantilever.

- In addition, the intrinsic surface charges or any variation in the surface charge, resulting from changes in the solution pH, do not have a considerable effect on the resonance amplitude.

7.2.   Future work

Based on the study conducted in this work the following suggestions are presented for future research in this field:

- Performance of the fabricated microfluidic cantilevers in collecting IR spectra of ethanol was demonstrated where only picolitres of ethanol were required. However, to establish this platform as a highly selective spectroscopy method, a complex mixture analysis which involves multiple analytes can be crucial.

- As presented in Chapter 4, interactions of water and ethanol result in nonlinear shifts in $C\text{-}C\text{-}O$ peak positions in the IR spectra (collected by a PCDS method). This nonlinearity was shown to be related to the induced dipole moments in the mixtures. In addition, the results of the study in Chapter 5 indicates that the thermal sensitivity of the device increases when the

channel height reduces. However, a shorter microfluidic channel confines smaller volume of liquids which in turn reduces the generated heat during non-radiative decay. Therefore, to find out the optimal channel height for spectroscopy purpose, BMCs with various heights need to be employed to study the concentration dependency of the absorption peaks in the IR spectra. This can further improve the resolution of the acquired data which in turn can help to shed more light on the role of ethanol-water interactions on the absorption peaks.

- Following the success of the fabricated microfluidic cantilevers in revealing intermolecular interactions in the collected IR spectra, the device's capability can be further investigated for more complex mixtures.

- The new model developed in Chapter 5 improves the thermal sensitivity prediction of the BMC, by including the microfluidic channel in the analysis. However, a thorough study is yet to be accomplished to further improve heat sensitivity prediction of a liquid-filled BMC. This is particularly essential for developing new designs to increase the sensitivity for liquid-based studies such as measuring heat capacity, collecting IR spectra, and more.

- From the insights of the study presented in Chapter 6 it can be anticipated that electrode positions are important in the actuation of the electrolyte filled cantilevers. This effect can be studied by fabrication of the devices with embedded electrodes in the inlet and outlet and changing the distance between the electrodes by changing the length of fluid carrying microfluidic channel.

This study can possibly shed light on the relation between the external field and the resonance amplitude.

- In addition, actuation efficiency of the electrolyte filled cantilever can be improved by operating the system in vacuum. Exposing the exterior of the device to vacuum results in decreasing the energy loss. Therefore, the same amount of applied force results in a higher resonance amplitude.

Appendix A

Mask layout and designs

The entire mask layout and color code for each layer is presented in Figure A.1. Figure A.2 to Figure A. show the mask layout of the cantilevers located on different chips as they appear from the left side to the right side of the mask. Figure A.12 show the mask layout of a double-clamped microfluidic resonator located on Chip 10. Black squares show the locations of inlet and outlet. Green shows the microfluidic part. The hatched area shows the location of the backside patterns. These patterns define the location of the through-wafer holes.
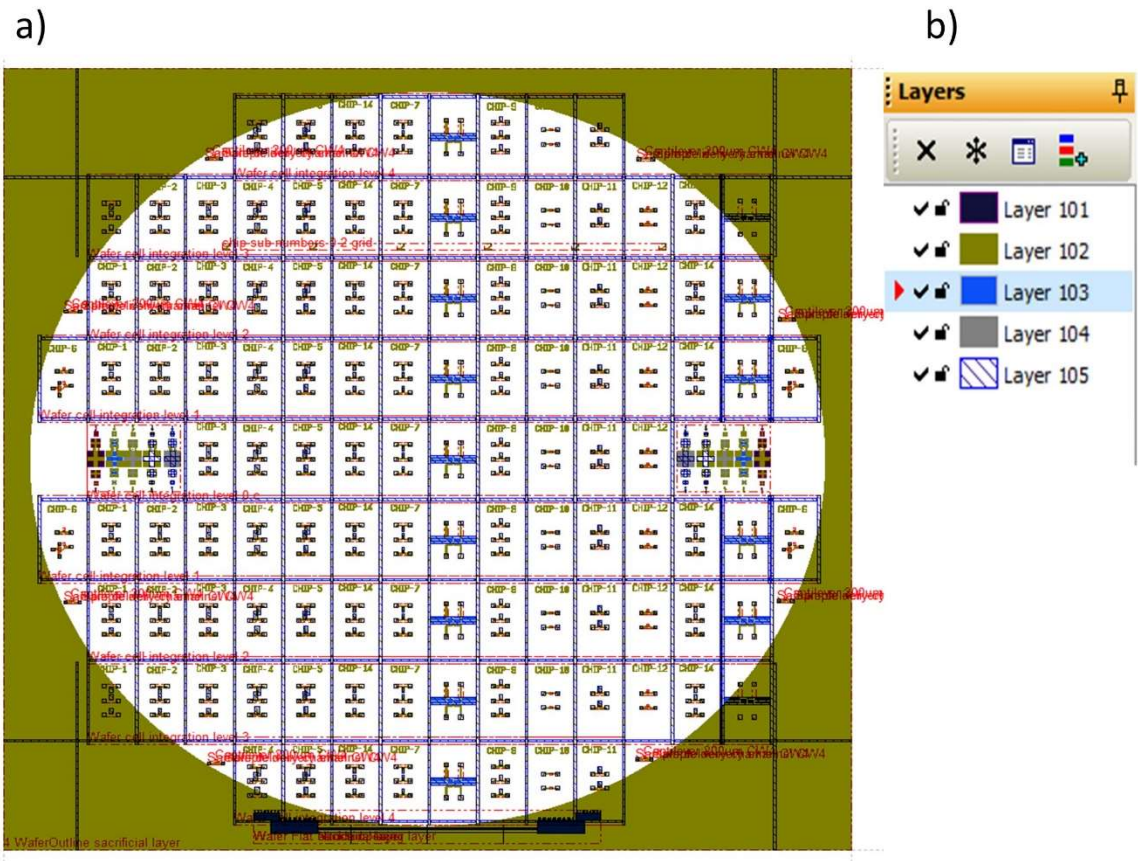
Figure A.1. a) The entire mask layout, b) color code for each mask.
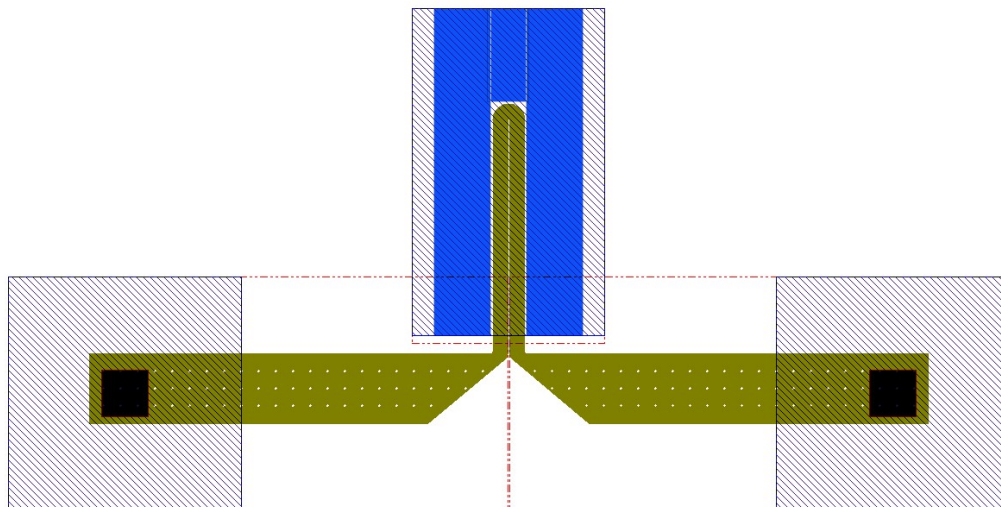
Figure A.2. Mask layout for a cantilever located on Chip 1.
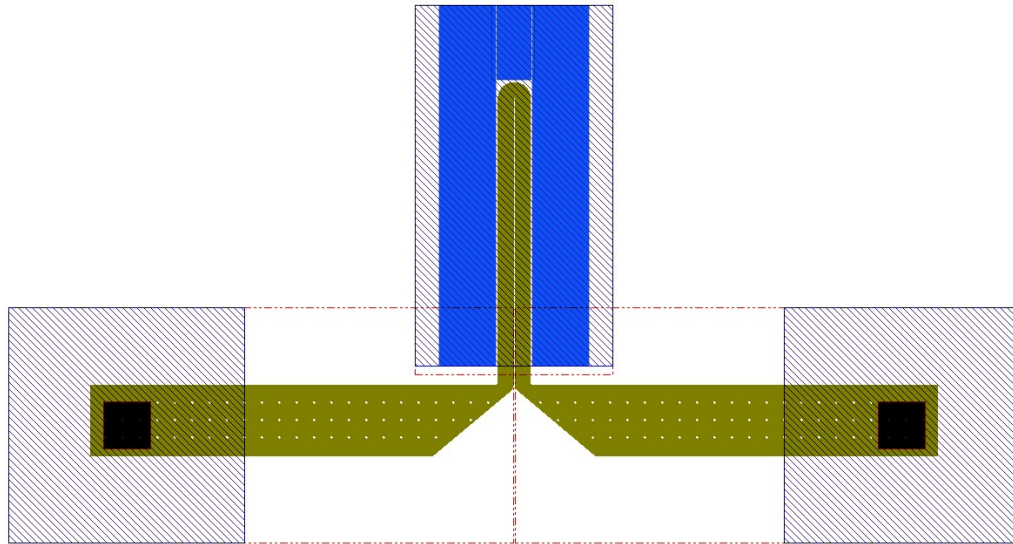
Figure A.3. Mask layout for a cantilever located on Chip 2.
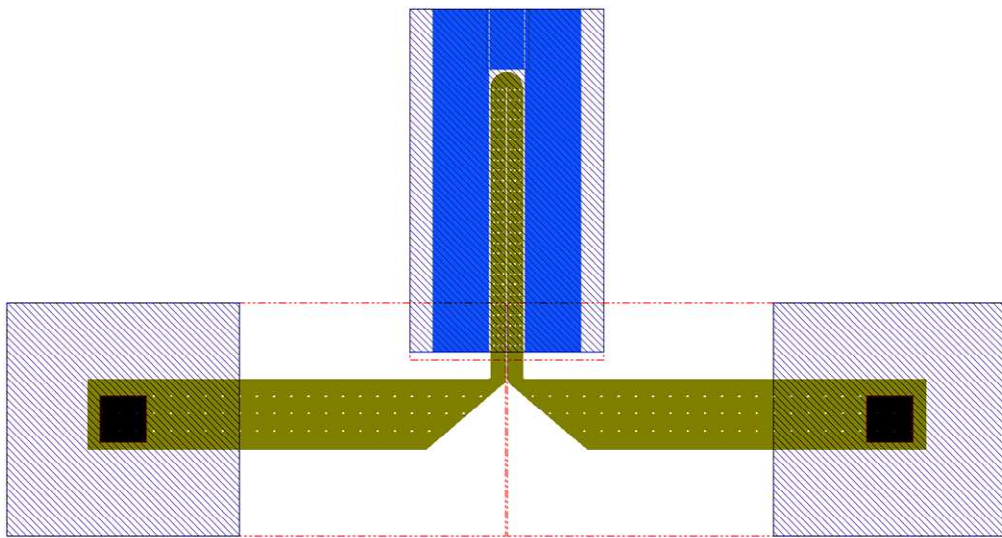
Figure A.4. Mask layout for a cantilever located on Chip 3.
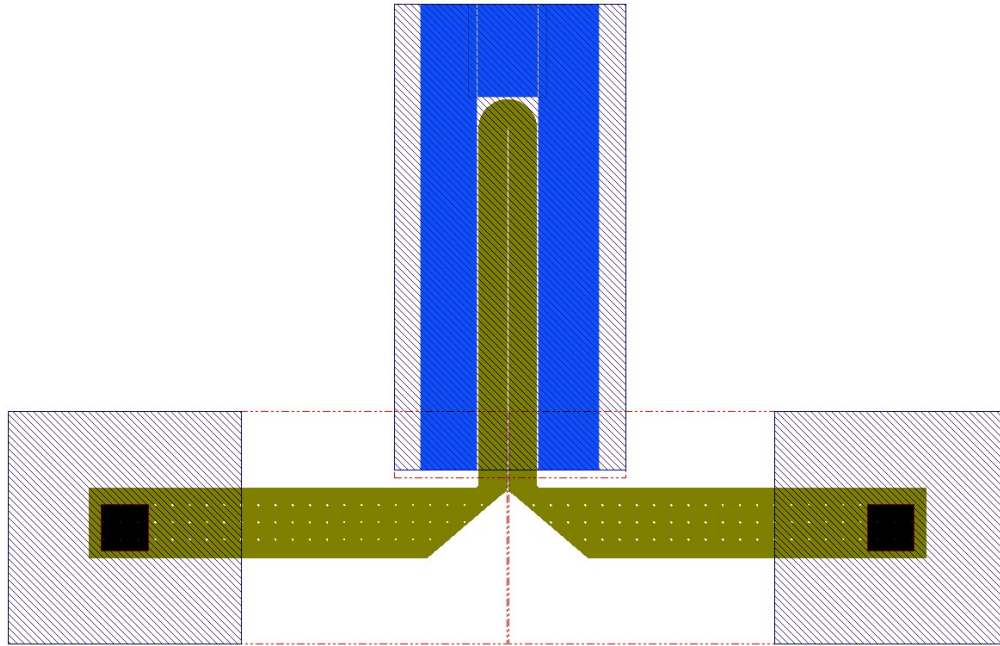
Figure A.5. Mask layout for a cantilever located on Chip 4.
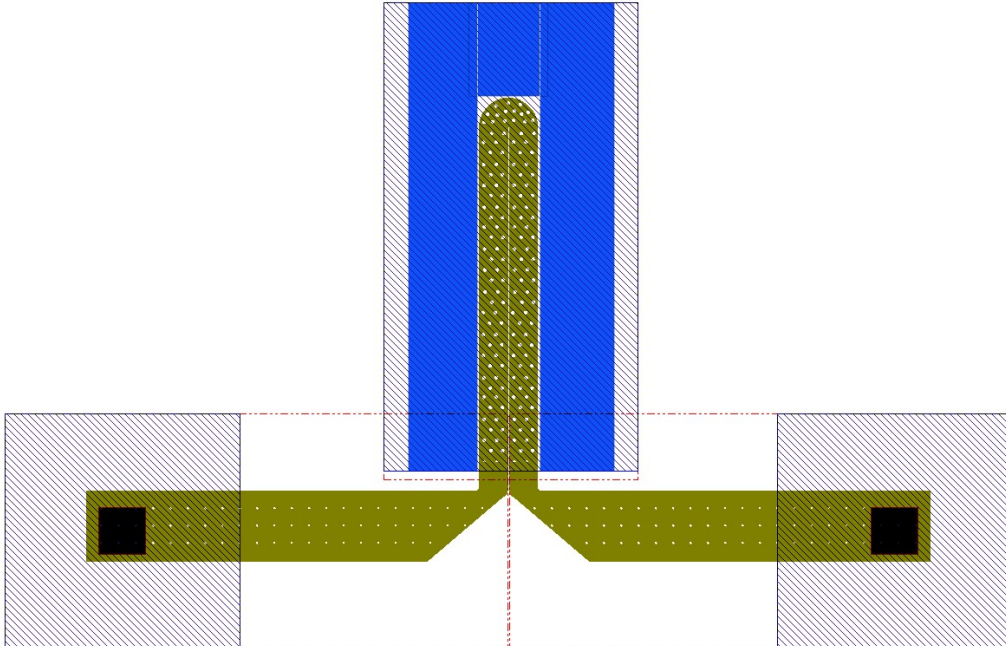
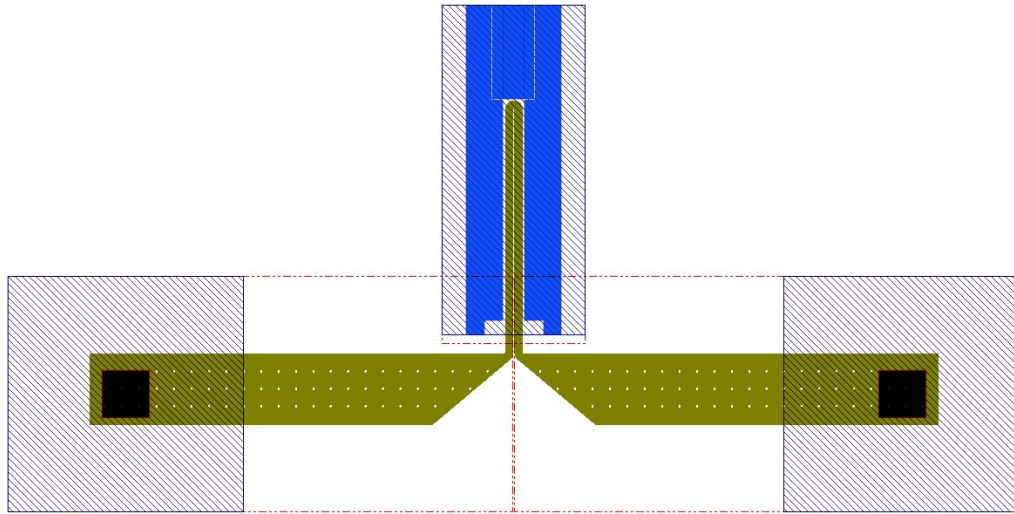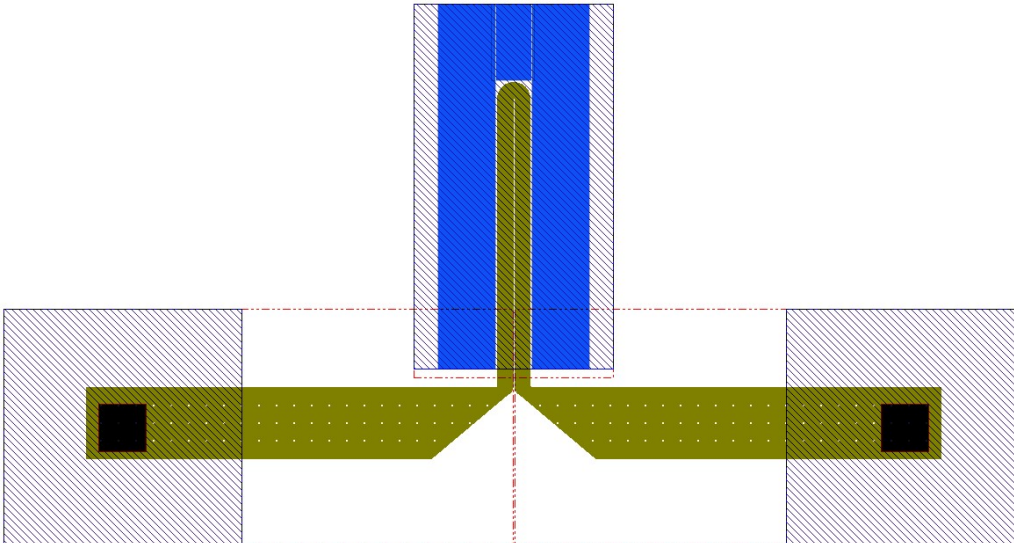Figure A.6. Mask layout for a cantilever located on Chip 5.
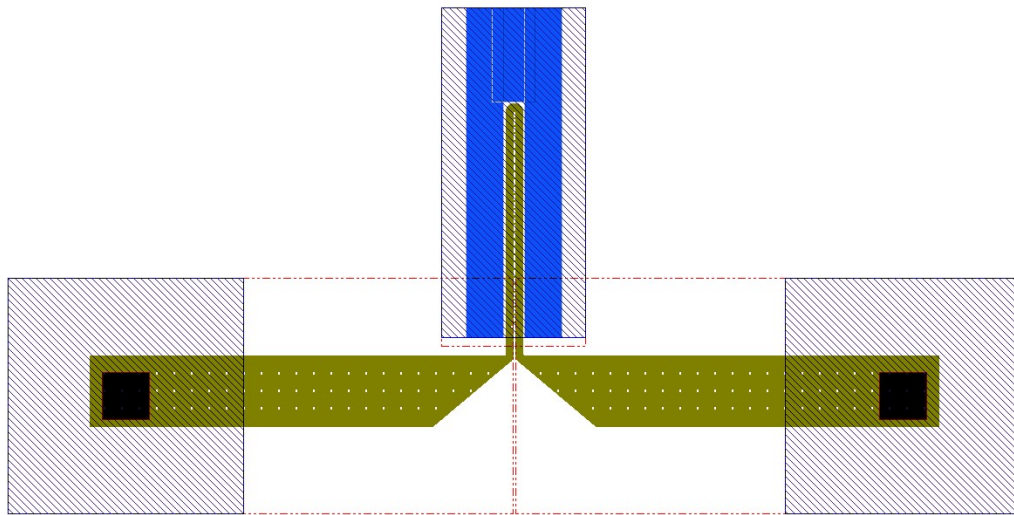
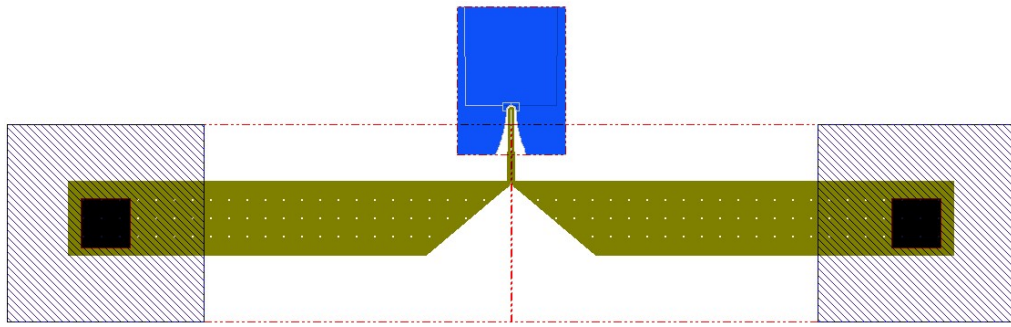Figure A.7. Mask layout for a cantilever located on Chip 14.
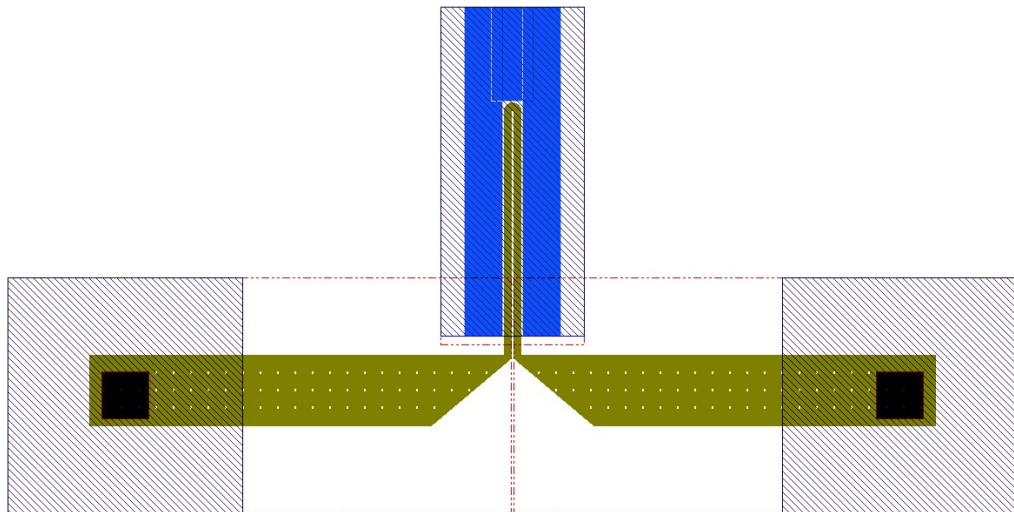
Figure A.8. Mask layout for a cantilever located on Chip 7.

Figure A.9. Mask layout for a cantilever located on Chip 9.

Figure A.10. Mask layout for a cantilever located on Chip 11.

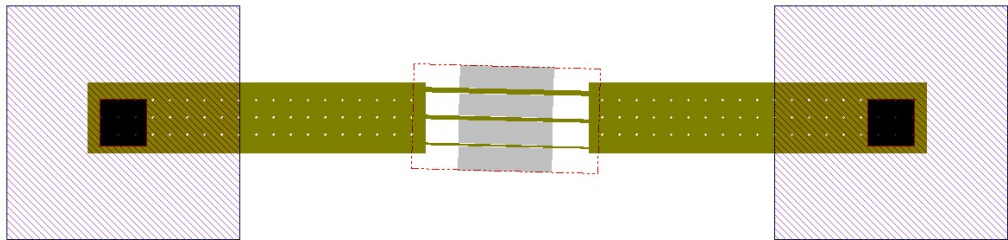Figure A.11. Mask layout for a cantilever located on Chip 12.

Figure A.12. Mask layout for a double-clamped microfluidic resonator located on Chip 10.

For example, microscopic images of a cantilever located on Chip 14 and a cantilever located on Chip 9 are shown in the following.
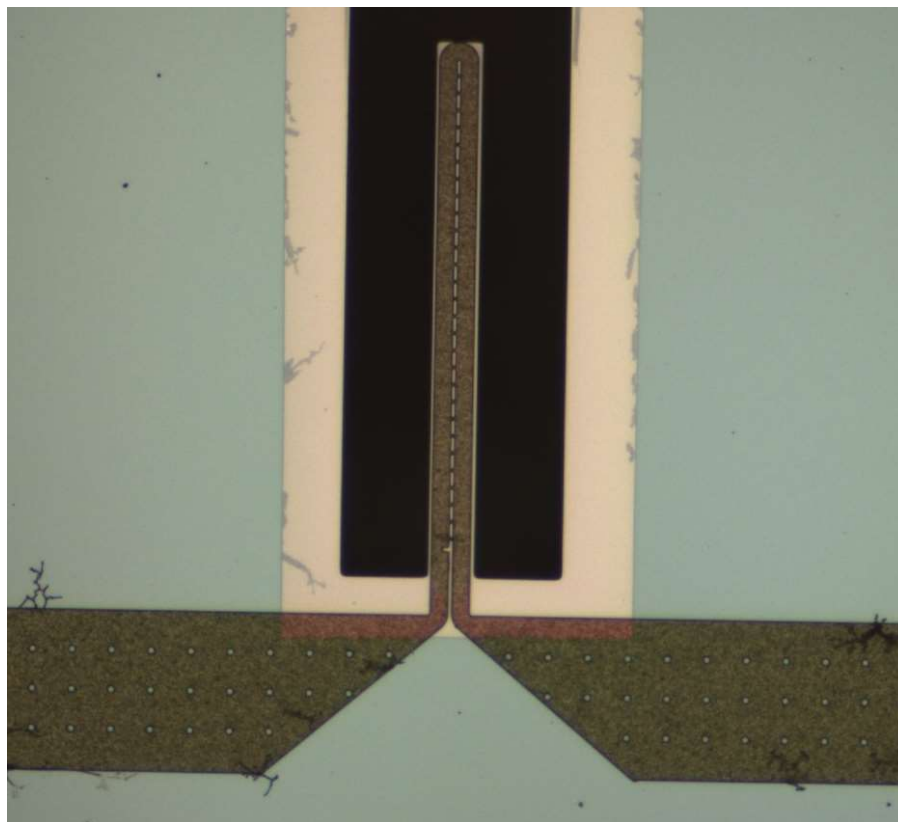

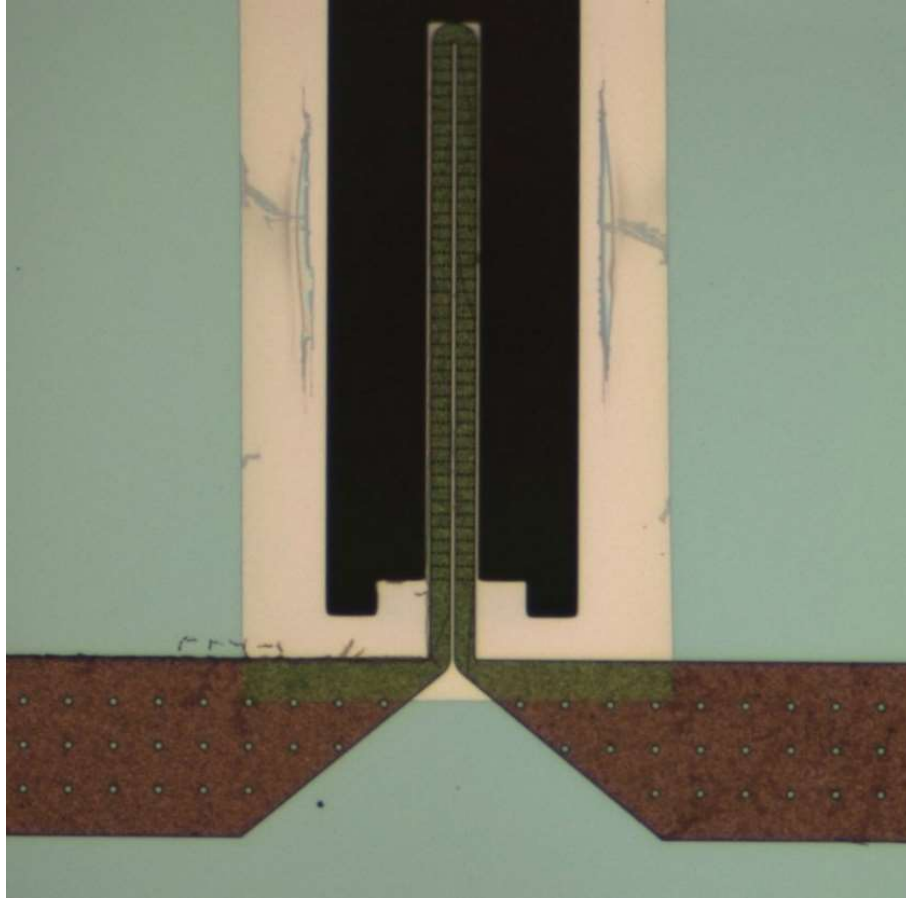Figure A.13. An microscopic image of a cantilever located on Chip 14

Figure A.14. An microscopic image of a cantilever located on Chip 9

Appendix B

Photoresist thickness

Figure B.1 shows the variation in the thickness of photoresist HPR 504 as a function of spin speed.
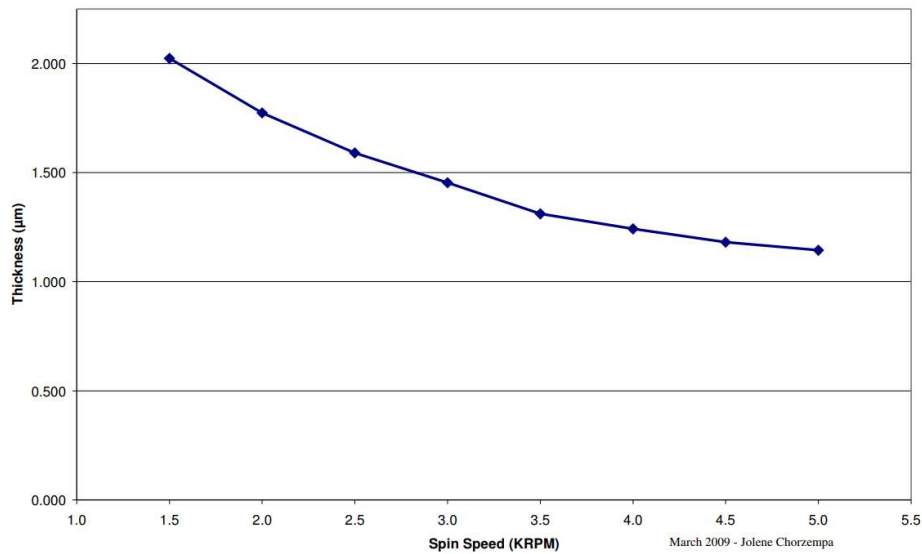

Figure B.1. Thickness of photoresist HPR 504 as a function of spin speed. Reprinted from resource library of nanoFAB with permission from University of Alberta nanoFAB.